System Identification and Active Control of a Turbulent Boundary Layer

by

Ruben Rathnasingham

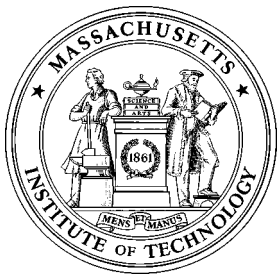

FDRL TR 97-6

Fluid Dynamics Research Laboratory
Department of Aeronautics and Astronautics
Massachusetts Institue of Technology
Cambridge, MA 02139

June, 1997

Abstract

An experimental investigation is made into the active control of the near-wall region of a turbulent boundary layer using a linear control scheme. System identification in the boundary layer provides optimal transfer functions that predict the downstream characteristics of the streamwise velocity and wall pressure fluctuation using an array of upstream flush-mounted sensors that are sensitive to spanwise shear. Enhanced detection techniques isolated the large scale turbulent motion and improved the downstream correlations resulting in greater controllability. The techniques were based on the conditioned spectral analysis between adjacent sensors to extract the most correlated flow structures that span the distance between them. The control is applied using a spanwise array of resonant actuators that introduce a pair of streamwise vortices into the flow. Control experiments were carried out for single and multiple input/output configurations. The single output results show that a maximum reduction of 34% is achieved in the streamwise velocity fluctuation. This reduction is greatest at the point of optimization but spans over a few hundred viscous lengths downstream of the actuator and about 50 viscous lengths in the spanwise and wall-normal directions. The wall pressure fluctuation and the mean wall shear stress (measured approximately using mean velocity profiles near the wall) was reduced by 17% and 7% respectively. The multiple-input/single-output configuration resulted in a wider spatial influence of the control while maintaining the maximum reductions in the fluctuations. The multiple-input/multiple-output configuration showed a marked increase in the spatial extent of the control (primarily in the spanwise direction), at the expense of a lower reduction in the fluctuations (maximum of 30% and 15% for the streamwise velocity and wall pressure respectively). The bursting frequency was computed from a VITA algorithm applied to the streamwise velocity fluctuation. The bursting frequency was reduced at all threshold levels examined but the maximum reduction of 23% occurred at a threshold level of 3. The spanwise spatial correlation was measured at different streamwise locations downstream of the actuator array. This result suggests that the reduction in turbulent fluctuations obtained using the current control scheme was achieved by reducing the strength of the most coherent flow structures and to inhibit their ability to interact with each other by increasing their average spanwise separation by more than 25% (from $\approx 90l^*$ to $120l^*$).

This is the Ph.D. Thesis of Ruben Rathnasingham, submitted to the department of Aeronautics and Astronautics at M.I.T. in June 1997, supervised by Prof Kenneth Breuer. For further information, please contact K. Breuer: `breuer@mit.edu`.

Acknowledgments

This work was supported by the Office of Naval Research, grant N00014-92-J-1918 monitored by Dr. L. Patrick Purtell.

First and foremost, I would like to acknowledge the guidance and patience of my supervisor, Kenny Breuer. It's quite amazing how much I've learned from him.

I am grateful to numerous collegues and friends for their support and encouragement through these years of research. Many thanks also to the graduate and undergraduate researchers with whom I have had the pleasure to work. In particular, the contribution of Thomas Lorkowski during the later stages of this research program was invaluable. I am most grateful to him for allowing me to use some of his results in my own thesis.

Finally, my undying gratitude to my parents and my little sister, Sunita, who were always there when I needed them. Their confidence in my ability to overcome the many hurdles I have faced during my academic life has been a crucial driving force in the pursuit of my goals.

Contents

List of Figures

List of Tables

Chapter 1

Introduction

The focus on boundary layer control has persisted for its potential benefits in transition and separation postponement, lift enhancement, drag reduction and noise suppression. The control of turbulent boundary layers, in particular, has received much interest in recent years mainly due to the growing understanding and appreciation of organized structures within the flow that are responsible for the majority of turbulence production. Their coherent nature and significance in the near-wall region make them primary targets in the control of the flow. Attempts to control turbulence typically either interfere with a component of the turbulence-producing cycle associated with these coherent structures or alter the interaction between them.

A review of some suggested control techniques and the approach taken here will be discussed, following a brief introduction on the current understanding of coherent structures.

1.1 The Structure of Near-Wall Turbulence

1.1.1 Kinematic Description

The idea of the large scale coherent motion in turbulent boundary layer flows stems from visual studies carried out by Kline *et al.* [1] among others, from 'conditional sampling' measurements [2, 3, 4] and numerical experiments [5] conducted over the past twenty years. A review of the conclusions drawn from various studies is given by Robinson [6].

Flow Visualization

The existence of streamwise oriented 'low-speed streaks' in the wall-region of a turbulent boundary layer has been well documented. These large scale coherent structures appear in the near-wall region of the boundary layer as streamwise-elongated streaks of low-speed fluid. These low-speed streaks, as described by Kim *et al.* among others [7, 1], have been shown to persist for up to a thousand viscous time scales (where a viscous time scale, t^*, is defined as the ratio of the kinematic viscosity, ν, and the square of the friction velocity, u_τ: $t^* = \nu/u_\tau^2$). They have been seen to extend for hundreds of viscous length scales in the

streamwise direction (where a viscous length scale, l^*, is defined as ν/u_τ), are typically tens of l^* wide and adjacent streaks by separated by approximately $100l^*$.

Conditional Sampling

The introduction of the Variable Interval Time Averaging (VITA) technique by Blackwelder and Kaplan [8] and subsequent modifications by Alfredsson and Johansson [4] and Johansson, Alfredsson and Eckelmann [3] provided a unique method by which the characteristics of the coherent structures could be isolated from the rest of the flow-field. A VITA event is considered to occur when;

$$var = \frac{1}{T}\int_{t-T/2}^{t+T/2} u^2(s)ds - \left(\frac{1}{T}\int_{t-T/2}^{t+T/2} u(s)ds\right)^2 > ku_{rms}^2, \tag{1.1}$$

where the technique has been applied to u and var is the short-time variance over an averaging time T and k is the threshold level. The VITA technique detects regions of high gradients in u, with time scales of the order of the averaging time. An event occurs when the variance exceeds ku_{rms}^2 so that the threshold level acts as a amplitude discriminator. The number of events detected will depend on k, so that no well-defined event frequency can be obtained and any such value must be accompanied by the corresponding threshold level. The addition of a slope criterion enable accelerating and decelerating events to be distinguished [4].

Experimental investigations by Johansson *et al.* [3], utilizing two hot-wire probes and the VITA conditional sampling technique for mapping the flow field, resulted in a detailed description of the coherent structures. The maximum inclination angle was found to be 20° in the buffer region. The streamwise extent of the coherent structures was confirmed to be about $100l^*$, and they retained their nature over a streamwise extent of at least $500l^*$ with an almost constant propagation speed $u_c = 13u_\tau$ up to $y^+ = 30$. The coherent structures were found to be essentially confined within the near-wall region (up to $y^+ \approx 100$).

Johansson, Alfredsson and Kim [9] applied a VISA conditioning technique (the spatial equivalent to VITA, where streamwise averaging is used rather than time averaging) on a numerically generated turbulent data base. By allowing for spanwise asymmetry, the coherent structures appear as pairs of adjacent streaks - a high-speed streak next to a low-speed streak. The composite structure exhibits a distinct discontinuity halfway along its streamwise extent, coinciding with the location of the maximum shear stress. An intense high-pressure region ($p > 2p_{rms}$) was also observed beneath the center of the structure. The propagation speed associated with the structures was slightly lower ($u_c = 10.6u_\tau$), but confirmed the experimental results.

The Evolution of Coherent Structures

A distinct characteristic of the low-speed streaks is the bursting process. Kim *et al.* [7] determined that the bursting process accounts for almost 70% of the turbulent production making its understanding crucial to the success of turbulence control. The association of turbulent energy production with the bursting process suggests that the time between bursts

or the burst frequency is a useful indication of the performance of any control scheme directed towards the large scale coherent motion.

They further described the process as the lift-up and growth of the streaks followed by a violent break-up and the ejection of fluid from the wall region into the outer flow. This is followed by a more quiescent flow accompanied by a sweeping of fluid towards the wall.

Landahl [10] suggested that the breakdown and the ensuing violent ejection constitutes the dominant non-linear mechanism for the fluctuating velocity field and proposed a regeneration mechanism whereby one breakdown triggers another leading to the self-maintenance of turbulence. The violent ejection of fluid into the outer flow is accompanied by a reduction in the streamwise velocity fluctuation, u, and an increase in the transverse velocity fluctuation, v. These velocity gradients can either be detected using the VITA technique or a quadrant technique which sorts out $u - v$ signals according to the signs of the individual u and v signals. Blackwelder and Haritonidis [2] showed that the time between bursts scales with inner wall variables and is approximately $100t^*$ at a threshold level of 3. However, Alfredsson and Johansson [11] introduced a mixed scaling (a combination of inner and outer scales) that collapsed their data. This implies that there is an influence from the inner region as well as the global flow.

Using the VISA technique, Johansson *et al.* [9] were able to follow the structures over their lifetimes. By doing so, the time history of the peak VISA variance amplitude could be mapped. They found that the variance amplitude increased with time, reaching a maximum before returning to its previous value. The amplitude was approximately symmetric about the time of maximum strength. There were no signs of unstable oscillatory motion or a violent break-up associated with the later stages of development as observed by Kim *et al.*. By considering instantaneous shear layer structures, they showed that individual shear layers develop a strong asymmetry as they propagate downstream and the streaky pattern remains more or less intact after the most active stages of the process.

Spanwise asymmetry is dynamically important since it seems to be directly coupled to the formation of the strong shear layer. Landahl [12] used the characteristics of an asymmetric structure to demonstrate instabilities that lead to the formation of streaks similar to those observed in experiments and numerical simulations. The spanwise asymmetry is required to give the initial disturbance a net vertical (wall-normal) momentum.

The dynamics associated with the coherent structures is further examined in the next section.

1.1.2 Dynamical System Models

For the purpose of better understanding and control of the near-wall flow, it is desirable to have a model from which control algorithms can be formulated. The representation of the wide range of scales in a turbulent flow requires the use of a large number of dimensions, which makes its analysis difficult. However, various low-order models that focus on the dynamics of coherent structures have been suggested.

Reduced-Order Models

Landahl [10] developed a two-scale model to describe the phenomenon of wave breakdown,

which was defined as small, high-energy instabilities that develop on large scale traveling wave disturbances. He compared this to the turbulent bursting process and suggested that it constitutes the dominant non-linear mechanism for the fluctuating velocity field in the turbulent boundary layer. A control scheme based on this model may focus on either or both of these two scales to provide a stabilizing control input.

The Karhunen-Loève (or proper-orthogonal) decomposition is a method by which dynamical systems are approximated by a finite series of basis functions. It is an energy-weighted representation so that when applied to a turbulent flow, it extracts the organized structures that contribute most to the energy. The method then allows one to recover as much of the energy in the system as desired, based on the number of modes used. The technique was introduced in the context of turbulence by Lumley [13] who suggested that it may be used to quantify the idea of coherent structures. Sirovich [14] developed a system of dynamical equations that result in a set of eigenfunctions which he then used to track the turbulent evolution of the flow. Rajaee [15] showed that the low-dimensional eigenfunction space obtained with this procedure described shear flow coherent structures well and that most of the fluctuating energy is captured by the first few modes of the expansion.

Aubry *et al.* [16] and Berkooz *et al.* [17] used the proper orthogonal decomposition to describe the flow in the near-wall region with a low order model. The technique is particularly efficient in providing eigenfunctions that represent second order turbulent statistics with a small number of modes. Aubry *et al.* expressed the velocity field in a turbulent boundary layer with eigenfunctions that were experimentally determined. These eigenfunctions took the form of streamwise rolls and were used to expand the Navier-Stokes equations with a Galerkin projection. The infinite dimensional system was then truncated to obtain a ten-dimensional set of differential equations. The equations represented the dynamic behavior of the streamwise rolls and were shown to exhibit intermittent burst-like phenomena. The results also suggested that the bursts were triggered by turbulent pressure signals from the outer layer.

In extending the work by Aubry *et al.* and Berkooz *et al.*, Keefe *et al.* [18] attempted to determine the number of dimensions required to describe wall-bounded flows by using a numerically simulated turbulent Poiseuille flow with spatially periodic boundary conditions. They argued that the number of dimensions required to fully resolved the large scale attractors in the flow, at a Reynolds number of 2.3×10^3, would not be greater than 780. Although finite, this suggests that the ten-dimensional model described above was inadequate in describing the large scale dynamics, especially when considering an open boundary layer flow. Keefe *et al.* also estimated that the data required to determine the attractor dimension was of the order of 10^D, where D is the dimension - exceeding current computer capabilities. However, this estimate refers to the entire boundary layer flow and would be much reduced when only focusing on the wall region.

Linearity

Various workers have suggested that the coherent structures are primarily governed by linear dynamics. For instance, Johansson, Her and Haritonidis [19] found that conditionally sampled u, v and p signals scaled linearly with threshold amplitude and demonstrated that

high amplitude pressure peaks, which are associated with the large scale motion, are linearly related to the velocity field through a turbulence-mean shear interaction term.

The strong mean-shear region near the wall has been emphasized in the development of simple models to describe the dynamics of the flow in that region. The Rapid Distortion Theory (RDT) of Turbulence (first developed by Batchelor [20]) is based on linear analysis for calculating rapidly changing turbulent flows under the action of different kinds of distortion such as large-scale velocity gradients and bounding surfaces. Hunt and Carruthers [21] discussed the application of this theory to describe slowly changing turbulence phenomena by focusing on the solutions of the RDT that are changing slowly with time and are approximately independent of the anisotropy and energy spectrum of the initial turbulence. The form of these RDT solutions describe turbulent processes that persist over many time scales and the predicted structures agree well with measurements, exhibiting regions of intensified transverse vorticity and streamwise velocity (streaks).

Landahl [12, 22] developed a model that highlighted the interaction between a turbulent eddy and the strong mean shear in the near-wall region and demonstrated a linear growth of the eddy with time. He inferred from this a relationship between the low-speed streaks and the linear streamwise growth of disturbances in a parallel shear flow.

1.2 Active Turbulence Control

The interest in active control of turbulence has stimulated several novel techniques including schemes that are based on qualitative physical arguments, adaptive schemes that use neural networks and schemes that incorporate an order reduction using dynamical decomposition in order to isolate the dominant structures in the flow. These methods have been implemented successfully to a certain extent but are usually limited by the complexity of the problem. The issues regarding the implementation of active control, (as well as the development of a linear dynamical model for turbulence control) is discussed by Breuer [23]. Contributions to the understanding of the turbulence control problem and suggested techniques for the practical implementation of control schemes have been studied by using idealized problems, where particular aspects of the flow characteristics are simulated, and by applying local and distributed control in a turbulent boundary layer.

1.2.1 Idealized Problems

Breuer *et al.* [24] conducted an experiment where they introduced an unstable disturbance into a laminar boundary layer that was temporarily stabilized by wall motion designed to induce spanwise velocity gradients. The actuator in this case consisted of a latex membrane stretched over a streamwise array of cavities embedded in the wall. The cavities were connected to independent solenoid valves that were attached to a pressure source enabling each cavity to be pressurized, deflecting each section of the membrane inwards or outwards (creating a depression or a bump). The actuator array was triggered on the arriving disturbances and was shown to delay the onset of turbulent spot formation by more than 10% in the streamwise direction. The cause of this stabilizing effect was suggested to be the reduction of the spanwise velocity gradient, $\partial w/\partial z$.

Nosenchuck and Lynch [25] performed active control experiments on artificially excited turbulent spots in the wall region of a water channel. Control was achieved by inducing velocity perturbations beneath detected low-speed streaks using flush-mounted heated elements. Results showed that the probability of streak bursting at a downstream location was dramatically reduced on applying the control. This, in turn, resulted in reduced turbulent intensities and reynolds stress. Flow visualization studies indicated that the control perturbations caused the low-speed streaks to diffused laterally, forming a temporary region of inactive flow close to the wall. In terms of a control description, heating had the effect of stabilizing the plant - in this case, the flow in the wall region.

Gad-el-Hak and Bleckwelder [26] used selective suction beneath artificially generated streaks in a laminar boundary layer to prevent bursting. They recommended the use of this technique with streamwise grooves on the wall to restrict spanwise movement of the streaks, increasing the probability of 'hitting' the target, thus improving control performance

Jacobson and Reynolds [27] investigated the use of piezo-ceramic driven actuators for controlling disturbances in a laminar boundary layer. The actuators consisted of piezo-ceramic/metal bimorph cantilevers mounted over cavities and driven at their resonant frequencies to produce counter-rotating longitudinal vortices in the wall region of the flow. When these vortices were aligned with artificially induced vortices in the boundary layer, the onset of transition to turbulence was delayed by up to 40 displacement thicknesses. They subsequently used of an array of such actuators to illustrate a feedforward control scheme based on upstream flow detection. An array of flush-mounted shear stress sensors were used to detect intermittent disturbances in the form of vortex pairs created by upstream suction holes. The detection of these flow structures triggered the actuator array which were designed to attenuate them. The control resulted in a substantial reduction in the integrated mean and root-mean-squared value of the downstream shear stress compared to the uncontrolled case.

Jacobson and Reynolds [28] also applied non-linear adaptive algorithms based on neural networks for the control of wall shear stress. A two-dimensional simulation, representative of a near-wall region of a turbulent boundary layer was used. Using information sensed at the flow boundary, the network parameters are trained to represent a relationship between the applied forcing and local streamwise velocity gradient. This parametric model is then used to develop actuator controls that minimize the wall shear stress and was shown to reduce the skin friction by 8%.

1.2.2 Turbulence Control

Local Control

Wilkinson and Balasubramanian [29] investigated the influence of a traveling surface depression on turbulent pre-burst flow. Both numerical and experimental studies focused on canceling the moving adverse pressure gradient associated with convecting, pre-burst 'typical' eddies [30] using a local wall depressions so as to stabilize the pre-bursting flow. In addition, the wall depression also stretches the velocity profile in the wall-normal direction,

reducing its inflection, which may contribute to the instability that gives rise to the bursting process. In the experiment, a flush mounted hot-film sensor was used to detect the upstream wall shear stress which was used as the trigger signal for the downstream array of actuators. The actuator array consisted of ferromagnetic elements, aligned in the streamwise direction, placed underneath a latex membrane on the surface that were independently forced by electromagnets to create a traveling surface depression. The actuator array was triggered by both negative and positive shear stress events, detected by the upstream sensor, to create a phase-locked wall motion underneath the convecting eddy. The results show a weakening of the inflectional velocity profile near the wall and a reduction in Reynolds stress when the actuation was triggered on negative shear stress events suggesting that the pre-burst motion could be mechanically stabilized using properly phase-locked surface depression.

More recently, Carlson and Lumley [31] investigated the active control in the wall region of a minimal flow unit, defined as the smallest computational box in which a turbulent channel flow may be sustained. The unit contained a single pair of adjacent coherent structures; a high- and low-speed streak. Actuation was achieved using wall motion in the shape of a Gaussian 'bump'. The bump was raised at a constant velocity of u_τ and reached a maximum height of $12l^*$ above the wall. The controller was designed to activate the bump beneath either one of the streaks. When it was raised beneath the high-speed streak, low-speed fluid from the adjacent low-speed streak was allowed to expand into the wall region around the bump, reducing the local mean streamwise strain rate and hence the drag. When the bump was raised beneath the low-speed streak, high speed fluid entered the wall region resulting in a drag increase. Although the behavior of actual streaks in a turbulent boundary layer is more complicated than the dynamics that occur in a minimal flow unit (due to the multiplicity of coherent structures), these results illustrate a practical method for the control of wall shear stress by redistributing momentum in the near-wall region.

Distributed Control

Choi *et al.* [32] used an active cancellation scheme to mitigate the effects of near wall vortices. The control effort was based on the injection of vertical momentum into the wall region and was studied in a direct numerical simulation of a turbulent channel flow. The best results were achieved when the control was applied to cancel the vertical velocity fluctuation at $y^+ = 10$, resulting in a drag reduction of 20%. For this scheme to be applied in practice, it must be based on flow characteristics at the wall so as to avoid any disruption of the flow. Choi *et al.* [32] addressed this issue by computing the correlation of measurable wall quantities with the vertical velocity above the wall. They then based their control output on these correlations. This only resulted in a 6% drag reduction which is comparable to that achieved by passive devices [33].

Lee *et al.* [34] developed a neural network scheme that employed blowing and suction at the wall based on the spanwise wall shear stress. Numerical experiments carried out in a simulation of a turbulent channel flow showed a reduction of skin friction of up to 20%. They also found that the network parameters maintained stable values so that they could be employed, without the time-consuming network training, to derive a simple control scheme that produced the same drag reduction. This idea of identifying a relationship (in this case,

that represented by the parameter values) between inputs and outputs is the basis for the work presented here.

Coller *et al.* [35] used the technique of proper orthogonal decomposition to develop a low-dimensional model of bursting in a turbulent boundary layer so as to implement a feedback control scheme. Their controller is based on a cross-flow, induced over the domain of the model. The effect of this cross-flow on the velocity field is expressed in terms of the basis functions that were obtained through the decomposition. The aim was then to direct the flow towards a stable, equilibrium point. They concluded that in the presence of noise, complete stability of the flow is unlikely. However, the time spent close to the point of equilibrium was extended, delaying the bursting process.

The application of optimal control theory in a numerically simulated turbulent channel flows was investigated by Bewley and Moin [36]. A cost function based on the drag integrated over the walls was minimized by determining the sensitivity of the flow to the control (spatially distributed wall-normal blowing and suction). Their results show a 17% reduction in drag using small levels of control. However, it was based on knowing all turbulent fluctuations above the wall. To make the scheme practical, they used a Taylor expansion to estimate the velocity at the wall and resulted with a 15% drag reduction.

1.2.3 Control Requirements

Practical implementation of any active control scheme is made particularly difficult by several physical constraints, including (i) sensors and actuators must be located at the wall, (ii) available sensors and actuators have finite size and exhibit a variety of performance constraints and (iii) existing computational hardware for real-time control has finite bandwidth.

Furthermore, in designing controls for dynamic systems, it is necessary to have a model that adequately describes the system behavior. There are typically two methods by which a model may be constructed; (i) when the physics that govern the system is well understood, one may develop equations of motion that characterize the behavior of a state vector. This vector consists of the entire set of independent variables that together describe completely the dynamic response of the system at all times; (ii) when the system is governed by complex processes, it may not be possible for a satisfactory model to be defined. In these cases, a model may be constructed with data taken from experiments directly conducted to measure the behavior of the plant. Using optimization techniques, this model provides the best estimate of the unknown plant response. Both modeling techniques have been used in the study and control of turbulent flows.

In this work, the approach described is one where the physics of the flow is initially identified and formulated into control blocks that may be coupled together to form a control scheme. The control objectives are based on the assumption that large scale turbulent structures are dominated by linear dynamics. For the purposes of control, this linearity assumption need only hold for the short time it takes a structure to convect from an upstream sensor to an actuator and does not imply that turbulence production as a whole is governed by a linear mechanism. Thus, a linear control schemes directed towards these large scale structures may be conceived provided that their linear dynamics is isolated from the rest of the turbulent motion.

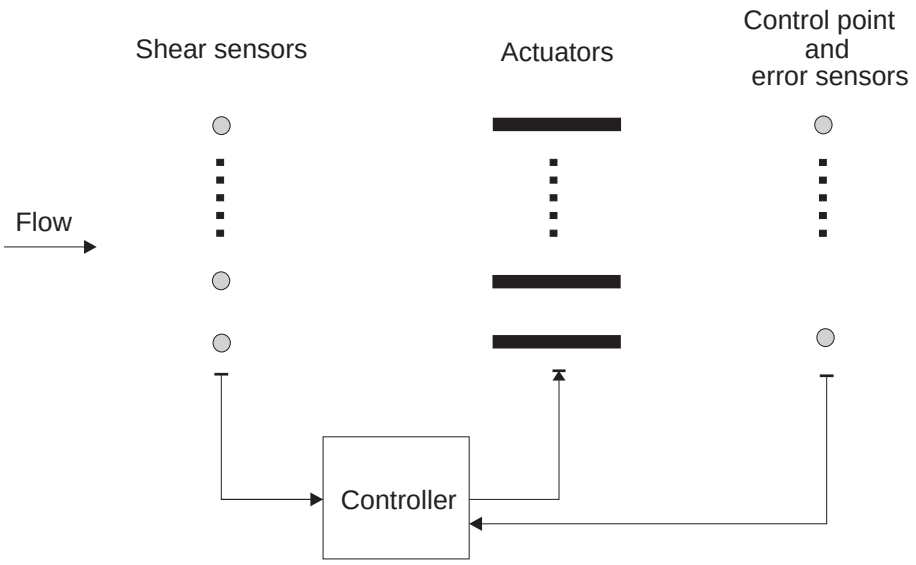

Figure 1.1: Schematic diagram illustrating the primary components in the proposed control scheme.

The primary components of the present experiment is summarized as, (i) the identification of the large scale coherent motion using wall sensors, (ii) the linear prediction of their evolution downstream, (iii) the characterization of the effect of the actuator on the flow and (iv) the feedforward controller that filters the sensor signals and provides the appropriate actuator input. Figure 1.1 is a sketch of the proposed control architecture showing the relative position of each component and how they are integrated into the system. An array of upstream sensors are used to detect the on-coming flow and predict the flow characteristics at a downstream control point. Their signals are read into a digital signal processor (the controller) that computes the appropriate input for an array of downstream actuators. The effect of the actuators on the flow at the control point is predetermined and is incorporated in the control loop. A sensor placed at the control point measures the control performance and returns an error signal that is monitored and used for the adaptation on the controller.

Chapter 2

System Identification

In this chapter, techniques for the optimal characterization of stochastic systems are discussed. The application of these techniques in a turbulent boundary layer and the formulation of the results in a framework of a control system is also presented. The method employed here is based on numerous system identification experiments to determine the most important characteristics of the plant - in this case, the flow in the wall region. As mentioned in the introduction, the primary contribution to the dynamics near the wall is assumed to come from the behavior of the coherent structures and the identification techniques are geared towards their characterization. The characterization of the boundary layer was based on measurable variables in the near-wall region, namely the wall shear stress, streamwise velocity fluctuation and wall pressure fluctuation. The results were then used to optimally predict the evolution of coherent scales in the flow so as to determine appropriate actuator inputs.

The controller was designed to compute the actuator inputs based on the prediction of the flow at a downstream control point and the effect of the actuator on the flow at that point. The effect of the actuator is expressed as a transfer function between the input voltage and the controlled quantity at the downstream control point.

Model design techniques may be classified into two categories, namely parametric and non-parametric. Parametric identification involves the estimation of plant parameters that may be polynomial coefficients or pole and zero values that describe the characteristic transfer functions. This technique is particularly useful in adaptive control, where the design must be implemented on-line and either the plant or controller parameters have to be estimated periodically. In contrast, non-parametric identification relies directly on the variation of the transfer function with frequency, without any knowledge of the plant parameters. The advantage in this case is that the design of a compensator for a required frequency response objective can be carried out simply by using the various standard methods in control analysis (i.e. Nyquist, Bode or Nichols method [37]). This form of analysis also allows weak non-linearities to be estimated by linear functions, while larger deviations from the linear response lead to the concept of 'describing functions' [37] - a concept based on the frequency-response. The two modeling techniques are interchangeable, in that, the transfer function and frequency response can be computed knowing the plant parameters, while the plant parameters may be estimated using the known frequency response. The latter is an

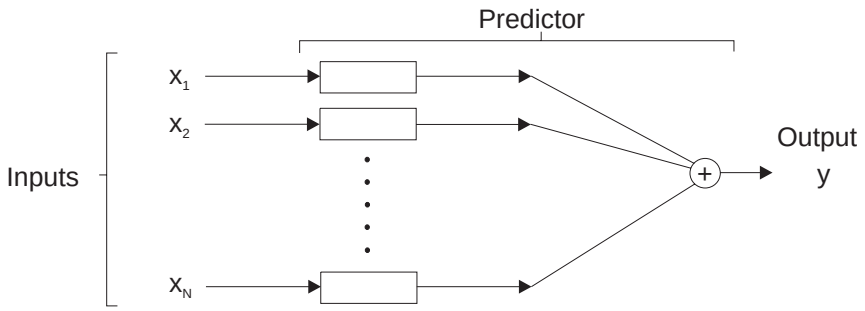

Figure 2.1: Schematic diagram illustrating a predictor that uses N inputs and N filters to estimate the single output y.

estimate since theoretically, there is no finite number of parameters that exactly describe the functional curve of the response.

The approach taken here is a combination of the two techniques. The identification experiments provide transfer functions that describe the evolution of coherent structures in the turbulent boundary layer. These transfer functions represent a non-parametric description in the frequency domain. For the implementation of the real-time adaptive control, however, these transfer functions need to be represented in a parametric form. The chosen form is a digital Finite Impulse Response (FIR) filter, the reasons for which will be discussed later. These filters are approximations of the transfer functions and are defined by filter coefficients that act as the parameters in the control scheme.

In the following control experiments, the aim of identification is to predict the evolution of large-scale turbulence structures as they propagate downstream. Multiple upstream sensors are used as inputs into a linear predictor, the output of which is a given downstream variable (Figure 2.1). Experiments are carried out in order to compute the optimum transfer function between the inputs and the output. This result is then approximated by digital filters whose coefficients represent the plant parameters. The control scheme is then designed to modify these parameters in real time. Hence, the experiment produces a non-parametric frequency response that characterizes the flow dynamics, but it is then necessary for a parametric form to be computed in order for an efficient adaptive control scheme to be implemented.

In this chapter, a brief description of the modeling of stochastic processes is given, together with the theory behind optimal filter design which will be used to construct the predictor - the first part of the control system. The design concepts discussed will be based on stationary analysis, where the input is assumed to be time-stationary and the system is assumed to have fixed parameters with a stable transfer function. This leads to a stationary output, provided the input has been present for a long period of time relative to the system time scales. In the turbulent boundary layer, the controlled parameters, namely the streamwise velocity, wall pressure and shear stress are assumed to be stationary in time.

2.1 Description of Stochastic Processes

The indeterministic nature of turbulence restricts its analysis to the use of statistical

methods. This results in either a time or frequency-based description computed from an ensemble average of independent samples. The time and frequency domains are related through the Fourier transform, but both descriptions independently provide vital information regarding the dynamics of turbulent processes.

The autocorrelation function is a time-based description and is given by;

$$R_{uu}(t,t') \;=\; < u(t)\, u(t') >, \tag{2.1}$$

where $u(t)$ is a sample at time t and '<>' represents an ensemble average. For stationary processes, as will be discussed here, the autocorrelation function depends only on the time difference $\tau = t' - t$ and may be written as;

$$R_{uu}(\tau) \;=\; < u(t)\, u(t+\tau) > . \tag{2.2}$$

The cross-correlation function between two variables $u(t)$ and $v(t)$ is given by,

$$R_{uv}(\tau) \;=\; < u(t)\, v(t+\tau) > . \tag{2.3}$$

The correlation functions provide the average time-dependence of the measured processes. That is, if the correlation decreases rapidly with τ, the process changes rapidly with time and slow variations with τ indicate slowly varying processes. Assuming Taylors' hypothesis, the correlation functions can also give a measure of the typical length scales in the flow [38].

The Fourier transforms of the autocorrelation and cross-correlation provide the autospectra and cross-spectra, respectively. They represent the frequency content of the processes and are given by,

$$\Phi_{uu}(\omega) \;=\; \frac{1}{2\pi} \int_{-\infty}^{\infty} e^{i\omega t}\, R_{uu}(\tau)\, d\tau \;\text{ and} \tag{2.4}$$

$$\Phi_{uv}(\omega) \;=\; \frac{1}{2\pi} \int_{-\infty}^{\infty} e^{i\omega t}\, R_{uv}(\tau)\, d\tau. \tag{2.5}$$

The spectrum is generally a complex function which may be conveniently thought of in terms of a magnitude and an associated phase angle. The correlation coefficient can in turn be expressed in terms of the inverse transform of the spectral function. Thus they form Fourier transform pairs and contain the same information about the process, but in different forms.

A useful application of correlation and spectral functions is in the computation of the transfer functions that relate inputs and outputs of a linear system. A transfer function is defined in terms of a Laplace transform,

$$H(s) \;=\; \int_{0}^{\infty} e^{-s\tau}\, h(\tau)\, d\tau, \tag{2.6}$$

where s is the complex frequency and $h(\tau)$ is the weighting function which is defined as the output of a system, at any time, to a unit impulse input applied at a time τ before. Note that the lower limit of the integral in Equation 2.6 is zero since $h(\tau) = 0$ for $\tau < 0$. Hence the spectral function is a special case of the transfer function with the real part of s equal to zero. For physically realizable and stable systems, the spectral function may replace the transfer function with no loss of useful information.

The transfer function is typically written in a parametric form, with a numerator and denominator polynomial whose roots represent zeros and poles of the system, or in a non-parametric form, as a function of frequency. The detailed characteristics of a transfer function together with its computation will be discussed in Section 2.3. In the subsequent experiments, transfer functions will be computed via the measurement of cross-spectra between inputs and outputs. This non-parametric form is useful for design purposes but must be converted to a parametric form if it is to be applied to real-time control. The most efficient method by which this is done is by approximating the transfer function as a filter. The filter is designed to have the approximate frequency characteristics of the transfer function so that a filtered input signal will provide an estimate of the output. There are several filter design methods available [37], but the optimal Wiener filter is most commonly used in designing for stochastic processes [39] and will be briefly described here.

2.2 The Wiener Filter

The Wiener filter may be defined as the optimal linear filter that separates a random noisy signal into its signal and noise components. The criterion for optimization is minimum mean-squared error, which is a good physical criterion in many applications. A primary assumption in the optimization procedure is that both signal and noise are random processes with *known* spectral (or equivalent) characteristics. The filter is expressed in terms of a weighting function which transforms the noisy signal into the estimated signal without noise.

The problem may be formulated as follows: assume a random signal, $x(t)$, is corrupted by random noise, $n(t)$, so that the resultant signal is $x(t) + n(t)$. An optimal filter with this noisy signal as an input, produces an output, $y(t)$, that will approximate $x(t + t_0)$ to within the performance criterion of minimum mean-squared error, where the error is defined as $e(t) = x(t + t_0) - y(t)$. Note that the filter type is generalized by setting the ideal filter output to $x(t + t_0)$, the choice of t_0 determining the nature of the filter:

1. $t_0 > 0$: Prediction. The filter will try to predict the signal value t_0 ahead of the present time.

2. $t_0 = 0$. Filter. The filter is estimating the current signal value.

3. $t_0 < 0$. Smoothing. The filter will try to estimate the signal value t_0 before the present time.

The choice of t_0 thus depends on the application and is fixed for the optimization process. The details of the optimization process is documented in various texts [40, 41, 39, 42, 43, 44], and will be briefly summarized here for completeness.

The squared error may be written as,

$$e^2(t) \quad = \quad x^2(t + t_0) - 2x(t + t_0)y(t) + y^2(t). \tag{2.7}$$

If the optimal weighting function is denoted by $g(\xi)$, then the output may be written as a convolution integral,

$$y(t) = \int_{-\infty}^{\infty} g(\xi)\,(x(t - \xi) + n(t - \xi))\,d\xi, \tag{2.8}$$

and substituted into Equation 2.7 and averaged to produce an expression for the mean-squared error;

$$\begin{aligned}\overline{e^2} &= \int_{-\infty}^{\infty}\int_{-\infty}^{\infty} g(\xi)g(\eta)R_{(x+n)(x+n)}(\xi-\eta)\,d\xi d\eta \\ &\quad -2\int_{-\infty}^{\infty} g(\xi)R_{(x+n)x}(t_0+\xi)\,d\xi + R_{xx}(0),\end{aligned} \tag{2.9}$$

where the overbar represents an expected value. That is, the expected average value that would occur for an infinite number of trials [39]. The problem then reduces to finding the function $g(\xi)$ that minimizes $\overline{e^2}$. This is achieved using methods in calculus of variation and results in the characteristic equation;

$$\int_{-\infty}^{\infty} g(\xi)R_{(x+n)(x+n)}(\xi-\tau)\,d\xi = R_{(x+n)x}(t_0+\tau), \quad -\infty<\tau<\infty \tag{2.10}$$

which may be solved using Fourier transforms to give;

$$G(s) = \frac{\Phi_{(x+n)x}(s)\,e^{t_0 s}}{\Phi_{(x+n)(x+n)}(s)}, \tag{2.11}$$

where $G(s)$ is the transform of $g(\xi)$. That is, the weighting function, $g(\xi)$, is the inverse transform of $G(s)$ and the mean-squared error is given by;

$$\overline{e^2} = R_{xx}(0) - \int_{-\infty}^{\infty} g(\xi)R_{(x+n)x}(t_0+\xi)\,d\xi. \tag{2.12}$$

This solution may be easily extended to multiple input systems [42] and results in coupled integral equations that must be solved simultaneously.

In summary, Wiener filtering provides an optimal technique to extract the noise from a signal. An important and essential assumption in the theory is that the individual spectra or correlation functions of the noise and signal are known ($\Phi_{(x+n)x}(s)$ and $\Phi_{(x+n)(x+n)}$ in Equation 2.11). In the next section, a problem that uses the mean-squared error criterion for optimization is applied to a problem where the characteristics of the of the noise and the signal is not separately known.

2.3 Modified Optimal Filter Design

The constraint placed on the Weiner filter design regarding the explicit knowledge of the individual noise and signal characteristics is restrictive in many practical situations. For example, the problem addressed in the following experiments required that the evolution of particular large scale structures in the wall-region of the boundary layer flow be characterized so that their behavior at chosen control points can be estimated, given certain measurements taken at some upstream location. In this case, a filter was required to estimate the characteristics of a chosen variable (describing the characteristics of the flow at the control point) from the measurements of a different signal that is only partly correlated with the variable (that from the upstream sensors). In this case, the 'noise' may be thought of as that part

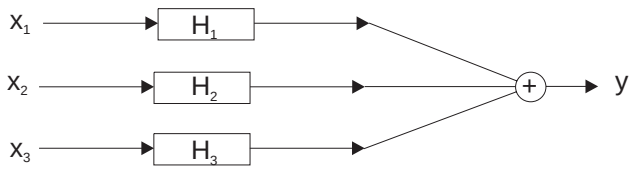

Figure 2.2: Block diagram illustrating a three input filter scheme that estimates a single output variable, y, using three filters, H_1, H_2 and H_3

.

of the measured signal that is not correlated with the variable and what is required is an optimal weighting function that may be applied to the measured signal so as to estimate that chosen variable. This is a very similar problem to that of the Wiener optimal filter except that the separate characteristics of the 'signal' and the 'noise' are unknown. What is given in this case, are the characteristics of the input and the ideal output, both of which have some noise embedded in them. The problem is then to estimate the ideal output from the input at all times.

2.3.1 Single Output Systems

The design problem may be categorized in terms of the number of outputs being estimated with a given number of inputs. For a single input/output linear system, the problem is somewhat trivial, in that the filter that estimates the output from the input is equivalent to the transfer function between them. Thus if the spectral characteristics of the input and output signals are known, then the filter is simply given by,

$$G_{xy}(\omega) = \frac{\Phi_{xy}(\omega)}{\Phi_{xx}(\omega)}, \tag{2.13}$$

where x and y are the input and output respectively. Complications arise when multiple inputs or outputs are required. An optimization process similar to that for Wiener filtering must be carried out, minimizing the mean-squared error, $\overline{e^2}$, where $e(t) = x(t + t_0) - y(t)$. The noise is explicitly left out of this analysis since the estimation is based on the whole signals. Since the optimized filter is an averaged result, its performance will depend on the correlation between the input and the output. That is, if the output is independent of the input, the filter will perform poorly, while if the output is linearly dependent on the input, the filter will reproduce the output exactly. Assumptions of linear filtering and stationary processes will be maintained.

A three input, single output model will be used here to demonstrate the optimization process. Figure 2.2 shows a system using the sum of three inputs, $x_1(t), x_2(t), x_3(t)$, and three filters, $H_1(\omega), H_2(\omega), H_3(\omega)$, to predict a chosen variable, $y(t)$. Given the spectra of the inputs and the output, the transform relationship may be written as;

$$Y(\omega) = H_1(\omega)X_1(\omega) + H_2(\omega)X_2(\omega) + H_3(\omega)X_3(\omega). \tag{2.14}$$

The spectral density of y is given by;

$$\Phi_{yy} = \frac{2}{T}\overline{Y^*Y}, \tag{2.15}$$

$$
\begin{aligned}
&= \frac{2}{T}\overline{(H_1^*X_1^* + H_2^*X_2^* + H_3^*X_3^*)(H_1X_1 + H_2X_2 + H_3X_3)}, \\
&= H_1^*H_1\Phi_{11} + H_1^*H_2\Phi_{12} + H_1^*H_3\Phi_{13} \\
&\quad + H_2^*H_1\Phi_{21} + H_2^*H_2\Phi_{22} + H_2^*H_3\Phi_{23} \\
&\quad + H_3^*H_1\Phi_{31} + H_3^*H_2\Phi_{32} + H_3^*H_3\Phi_{33}, \qquad (2.16)
\end{aligned}
$$

where T is the record length of the inputs and output. Similarly,

$$
\begin{aligned}
\Phi_{1y} &= \frac{2}{T}\overline{X_1^*Y}, \\
&= H_1\Phi_{11} + H_2\Phi_{12} + H_3\Phi_{13}, \qquad (2.17) \\
\Phi_{2y} &= \frac{2}{T}\overline{X_2^*Y}, \\
&= H_1\Phi_{21} + H_2\Phi_{22} + H_3\Phi_{23}, \qquad (2.18) \\
\Phi_{3y} &= \frac{2}{T}\overline{X_3^*Y}, \\
&= H_1\Phi_{31} + H_2\Phi_{32} + H_3\Phi_{33}, \qquad (2.19)
\end{aligned}
$$

which may be written as a series of linear equations;

$$
\begin{bmatrix} \Phi_{11} & \Phi_{12} & \Phi_{13} \\ \Phi_{21} & \Phi_{22} & \Phi_{23} \\ \Phi_{31} & \Phi_{32} & \Phi_{33} \end{bmatrix} \begin{bmatrix} H_1 \\ H_2 \\ H_3 \end{bmatrix} = \begin{bmatrix} \Phi_{1y} \\ \Phi_{2y} \\ \Phi_{3y} \end{bmatrix}, \qquad (2.20)
$$

which in turn may be solved for $H_1(\omega), H_2(\omega), H_3(\omega)$ at each frequency. These functions now represent filters that estimate the output from the three measured inputs.

2.3.2 Multiple Output Systems

A similar approach is adopted for the multiple-input/multiple-output case except that it results in a matrix of transfer functions, H_{xy}, that relate each input to each output. A brief analysis of the optimization process is given below [45]. Given N inputs and M outputs,

$$
\begin{aligned}
x(f) &= \{x_1, x_2, \ldots, x_N\} \text{ and} \qquad (2.21) \\
y(f) &= \{y_1, y_2, \ldots, y_M\}, \qquad (2.22)
\end{aligned}
$$

a transfer function matrix , H_{xy}, may be written;

$$
\begin{aligned}
y &= H'_{xy}x \qquad (2.23) \\
x^*y' &= x^*x'H_{xy}. \qquad (2.24)
\end{aligned}
$$

where the superscripts (*) and (′) represents the complex conjugate and transpose matrix respectively. H_{xy} contains the cross-spectra between each input and output (which in turn represent the transfer functions between the inputs and outputs),

$$
H_{xy} = \begin{bmatrix} H_{1y_1} & H_{1y_2} & H_{1y_3} \\ H_{2y_1} & H_{2y_2} & H_{2y_3} \\ H_{3y_1} & H_{3y_2} & H_{3y_3} \end{bmatrix}. \qquad (2.25)
$$

The expectation of Equation 2.24 may then be written as

$$G_{xy} = G_{xx}H_{xy}, \tag{2.26}$$

where $G_{xy} = E\{x^*x'\}$ and $G_{xx} = E\{x^*y'\}$. The transfer function matrix is then given by,

$$H_{xy} = G_{xx}^{-1}G_{xy}. \tag{2.27}$$

The optimization procedure then involves computing G_{xx} and G_{xy} from measured data and subsequently solving Equation 2.27 for H_{xy} which is an $N \times M$ matrix (where N and M are the number of inputs and outputs, respectively).

2.4 Discrete Time Formulation

2.4.1 FIR and IIR Filters

Discrete filters are broadly divided into two classes, namely FIR (finite impulse response) filters and IIR (infinite impulse response) filters. Both filters may be written in terms of its impulse response, $h(k)$;

$$y(n) = \sum_{k=0}^{\infty} h(k)x(n-k) \quad \text{for the IIR filter and} \tag{2.28}$$

$$y(n) = \sum_{k=0}^{N-1} h(k)x(n-k) \quad \text{for the FIR filter,} \tag{2.29}$$

where n is the current time step and k is the floating time step. From Equation 2.29, it is clear that the IIR filter is of infinite duration and cannot be implemented in practice. Instead, the IIR equation is expressed in a recursive form;

$$y(n) = \sum_{k=0}^{\infty} h(k)x(n-k) \tag{2.30}$$

$$= \sum_{k=0}^{N} a_k x(n-k) - \sum_{k=0}^{M} b_k y(n-k), \tag{2.31}$$

where a_k and b_k are coefficients of the filter. Note that for the FIR filter (Equation 2.29), the output sample is only a function of the past and present values of the input, whereas for the IIR filter (Equation 2.31, the output is a function of the past outputs as well as the present and past inputs. However, when b_k is set to zero, the two equations are identical.

The choice of using FIR filters in these experiments, as opposed to IIR filters was made based on the relative advantages of the two. Firstly, FIR filters have linear phase response so that no phase distortion is introduced by the filter. The phase response of IIR filters are non-linear, especially at the band edges. In this application, the filters were used to estimate the character of coherent flow structures as they convected downstream at a constant speed.

Phase distortion would introduce errors in estimating convection speeds and had to be kept at a minimum. Secondly, FIR filters are computed without any recursion and are always stable. This eliminates the problem of additional design to stabilize a filter before physical implementation. The stability of IIR filters cannot be guaranteed.

Hence, the FIR filter was chosen for its convenience of implementation and stability advantages. It is possible that, for a given order, IIR filters may be better in describing the evolution of the large scale structures in the flow. The dependence of the current output on the past outputs as well as the past and present inputs gives the IIR filter a 'feedback' characteristic. One advantage of this characteristic is that IIR filters normally require fewer coefficients than FIR filters.

2.4.2 Discrete Filter Design

Since the control system is implemented digitally, sampled data are processed using discrete operations. That is, each sample point is operated on individually based on a pre-computed set of functions. In a digital filter, for example, the function takes the form of a series of weights that are multiplied with the sampled data.

As mentioned earlier, in the FIR filter, the weights that result from the optimization process are multiplied by the past history of discrete inputs to yield the best estimate of the variable of interest. It is thus instructive to explore how the optimization process extends to the discrete-measurement situation. Consider the filter input to be a discrete series of additive combination of signal and noise, $a_1, a_2, \cdots, a_n$, where $a_i = x_i + n_i$. If the filter output at time t_n is written as a linear combination of past measurements;

$$y_n = k_1 a_1 + k_2 a_2 + \cdots + k_n a_n, \tag{2.32}$$

then the filter error is given by;

$$\begin{aligned} e_n &= x_n - y_n, \\ &= x_n - (k_1 a_1 + k_2 a_2 + \cdots + k_n a_n). \end{aligned} \tag{2.33}$$

The mean-squared error can then be expressed as a set of linear equations;

$$\begin{bmatrix} \overline{a_1^2} & \overline{a_1 a_2} & \cdots & \overline{a_1 a_n} \\ \overline{a_2 a_1} & \ddots & & \\ \vdots & & \ddots & \\ \overline{a_n a_1} & & & \overline{a_n^2} \end{bmatrix} \begin{bmatrix} k_1 \\ k_2 \\ \vdots \\ k_n \end{bmatrix} = \begin{bmatrix} \overline{a_1 x_n} \\ \overline{a_2 x_n} \\ \vdots \\ \overline{a_n x_n} \end{bmatrix}. \tag{2.34}$$

The elements of the matrix on the left-hand-side of Equation 2.34 correspond to the elements in the auto-correlation function of a and the column vector on the right-hand-side of Equation 2.34 corresponds to the cross-correlation function between the filter input and the current signal value:

$$\begin{bmatrix} R_{aa}(0) & R_{aa}(1) & \cdots & R_{aa}(n-1) \\ R_{aa}(1) & \ddots & & \\ \vdots & & \ddots & \\ R_{aa}(n-1) & & & R_{aa}(0) \end{bmatrix} \begin{bmatrix} k_1 \\ k_2 \\ \vdots \\ k_n \end{bmatrix} = \begin{bmatrix} R_{ax}(0) \\ R_{ax}(1) \\ \vdots \\ R_{ax}(n-1) \end{bmatrix}, \tag{2.35}$$

where $R_{aa}(-\tau) = R_{aa}(\tau)$.

Assuming the auto and cross-correlations are known, Equation 2.35 can then be solved for the weighting factors, $k_1, k_2, \cdots, k_n$. Although the solution is relatively straight-forward, it is clear that it becomes computationally intensive when a large number of data points are used, calling for the solution of a large number of coupled equations. Although this solution is relatively straight-forward, the time restrictions of the subsequent real-time implementation of the filter may be a problem if the number of weights are large.

Filter Order Reduction

In order for the filters to be implemented in a digital control scheme, they must be first expressed in discrete, low-order, parameterized form. This is most efficiently done using a least squares 'curve-fitting' approach by which a discrete filter is constructed by approximating the frequency characteristics of the measured filter. Consider a discrete filter, $H'(z)$, represented by a polynomial of a given order, $B(z)$, used to model a continuous function, $H(\omega)$. The minimization is applied to the squared error, written as;

$$e^2 \quad = \quad |B(z) - H(\omega)|^2. \tag{2.36}$$

Equation 2.36 is then differentiated with respect to the coefficients in $B(z)$ to obtain the minimum e^2. The result is the best estimation of the desired frequency response by a discrete filter with the given order. This procedure must be applied to all measured frequency responses and transfer functions before any digital control scheme is implemented.

Figure 2.3 illustrates the error in using a low-order FIR estimation of the measured frequency response. It shows that higher order filters are required to obtain adequate accuracy at the low frequency, high energy range of the spectra. A tolerance of $\pm 5\%$ in the root-mean-squared value was set and the minimum number of poles needed to achieve this was 32. This value was chosen for all transfer function approximations after verifying that the tolerance limits were met.

2.5 Conditioned Spectral Analysis

The capability of identifying a phenomena or structure of interest depends on the ability for all its properties to be taken into account in the identification scheme. As mentioned earlier, the large scale structures are known to contribute to the majority of the turbulence production making them the most attractive targets for control with the aim of reducing turbulent energy and Reynolds stress. These coherent structures have long lifetimes, making them suitable for feedforward or feedback control strategies (where the plant dynamics between sensor and actuator need to be well understood). Furthermore, as described in the introduction, the characteristic effect of the large scale structures on flow quantities such as velocity, pressure and shear stress fluctuations, make them more easily distinguishable from the rest of the flow. However, these characteristics are averaged effects associated with flow structures that occur randomly in space and time, making the identification of individual structures very difficult.

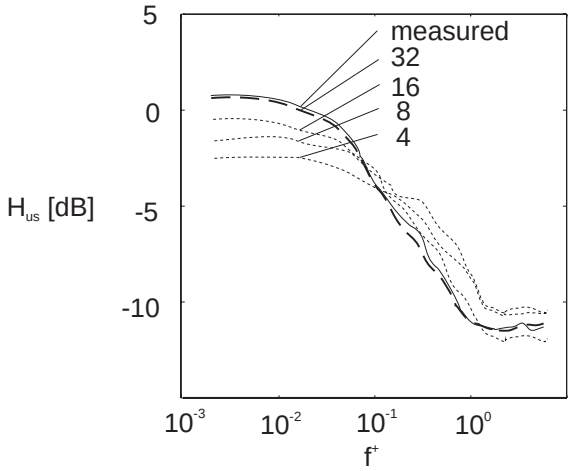

Figure 2.3: FIR filter approximations of a transfer function showing the effect of filter order on the accuracy.

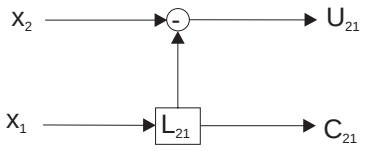

Figure 2.4: Block diagram illustrating the application of conditioned spectral analysis on two signals. The transfer function, L_{21} is used to separate x_1 into portions that are correlated and uncorrelated with x_2 (C_{21} and U_{21} respectively.).

In an effort to improve the robustness of the identification of the large scale structures, additional information regarding their physical dimensions and orientation were taken into account. The aim was to develop a method by which large and small scales in the flow can be continuously differentiated. This was achieved by employing a technique that used multiple real-time measurements of a single structure taken with a spanwise array of shear sensors. The signals from adjacent sensors were compared with each other to extract only the coherent parts between them. This was effectively a filtering process whereby the part of the measured signals corresponding to the large scale structures (low frequency) were emphasized and the rest of the flow (small scale, high frequency) were rejected.

The procedure by which the signals can be separated into correlated and uncorrelated portions is based on a conditioned spectral analysis [45]. Consider two sensors producing signals $x_1(t)$ and $x_2(t)$ that are placed next to each other in the flow to detect a passing coherent structure (Figure 2.4). The relationship of one to the other may be described in terms of the auto and cross-spectra between the two. For example, the portion of $x_1(t)$ that is correlated with $x_2(t)$ is given, in the frequency domain, by;

$$\begin{aligned} C_{12}(\omega) &= \frac{\Phi_{12}(\omega)}{\Phi_{22}(\omega)} X_2(\omega) \\ &= L_{12}(\omega)\, X_2(\omega). \end{aligned} \tag{2.37}$$

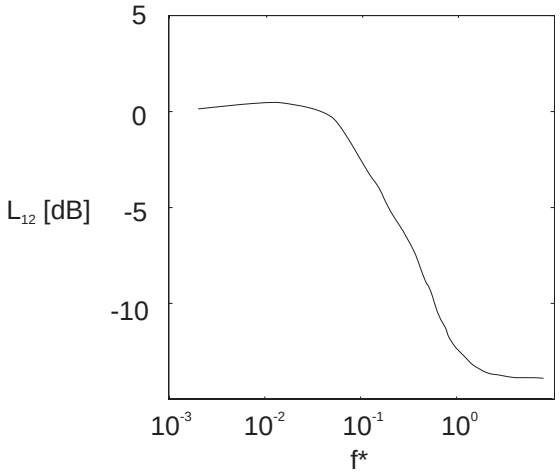

Figure 2.5: The filter L_{12} illustrating the emphasis of the low frequency scales. The filter was used to condition the signals from the detection sensors so as to extract the large scale motion in the flow.

The rest of the signal makes up the uncorrelated portion,

$$U_{12}(\omega) \quad = \quad X_1(\omega) - L_{12}(\omega)\, X_2(\omega). \tag{2.38}$$

In order to identify the most coherent structures in the flow from $x_1(t)$ and $x_2(t)$, one of the signals must be used together with the coherent portion of the other. For example, x_2 can be used with $L_{12}\{x_2\}$ to represent structures that are most coherent between the two sensors. Figure 2.5, which is the actual computed filter, L_{12}, (between two adjacent spanwise wall-shear sensors, separated by $40l^*$ in the spanwise direction) illustrates that the new signal, $L_{12}\{x_2\}$, has been preferentially weighted over the low frequencies signifying the association of the most coherent structures with the low frequency, large scale motion. This weighting representation of the identification procedure highlights a powerful method by which any characteristic of the flow regime may be isolated. For example, if a flow structure, associated with known frequency band is chosen to be extracted from the flow field, L_{12} could take a form of a band-pass filter, with stop-bands corresponding to the given frequency limits. The filtered signal will represent these particular flow structures that are spatially coherent between the two sensors.

In the case considered here, all subsequent filter designs based on these modified signals will represent the evolution of the dominant large scale structures only and will not be degraded by surrounding incoherent turbulent motion. Note that since L_{12} is pre-computed, the implementation of this configuration in real-time requires x_2 only. The signal is split into two branches, namely x_2 and $L_{21}\{x_2\}$, the latter representing the correlated portion of x_1, estimated from x_2.

2.6 Control Strategy

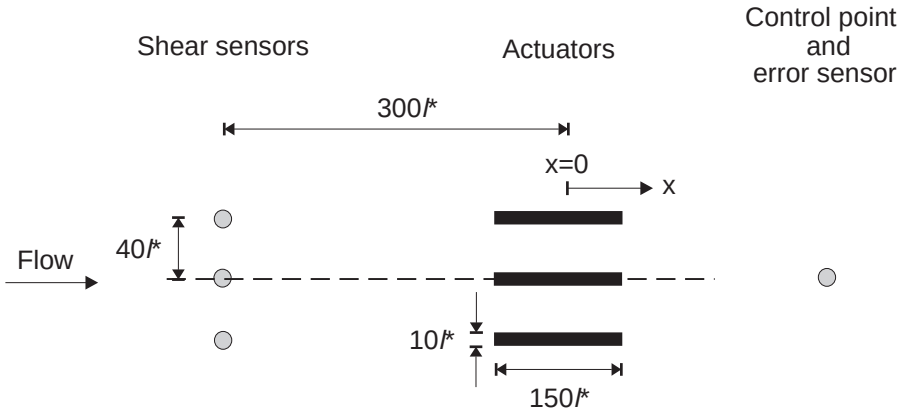

Figure 2.6: Schematic diagram showing the active matrix with the detection sensors, actuators and control point.

The scene has now been set for the control strategy to be designed. The physical arrangement of the active matrix containing the sensors (an array of 3 upstream detection sensors and a downstream error sensor) and actuators is given in Figure 2.6.

The control scheme was formulated with several important assumptions: (i) The wall sensors were operated using the anemometers which had high signal to noise ratios (> 500) so that sensor noise was ignored in the optimization process. (ii) In isolating the coherent structures by using the conditioned analysis between adjacent sensor signals, the contribution of the smaller scales to the control variable was neglected. This method of selection was employed primarily to emphasize the larger scales since they are known to contribute to the majority of the turbulent production in the boundary layer. (iii) The control objectives are based on the assumption that large scale turbulent structures are governed by linear dynamics. This concept was discussed in the introduction and has been supported by various workers. Consequently, the control of the flow was based on linear cancellation, so that the actuator was driven in such a way that it would create a control input that was the opposite of that estimated by the linear predictor to occur naturally in the flow.

The overall control scheme is shown schematically in Figure 2.7. H_1 and H_2 represent the measured transfer functions between the detection sensor and the flow characteristics at the control point and between the actuator and the flow at the control point, respectively. The equivalent low-order filter estimates for these transfer functions are written with a 'hat'.

A spanwise array of 'shear' sensors (s_1, s_2 and s_3) was used to identify on-coming coherent structures. $\hat{H}_1$ contains the filters that describe the coherent parts of the sensor signals (for example, L_{12}) and combine the conditioned signals with the linear predictor, to estimate the control variable at one or more downstream control points, s_d. In these experiments, the control variables were chosen to be the streamwise velocity fluctuation at various downstream locations and the wall pressure fluctuation, $200l^*$ downstream of the middle sensor, s_2. The predicted variable was then combined with the actuator input transfer function. This contained three blocks, $\hat{H_{21}}, \hat{H_{22}}$ and $\hat{H_{23}}$ which described the respective actuator transfer function, relating the input voltage to the output velocity and the transfer function between the output velocity and the downstream control variable. The desired control effect is to

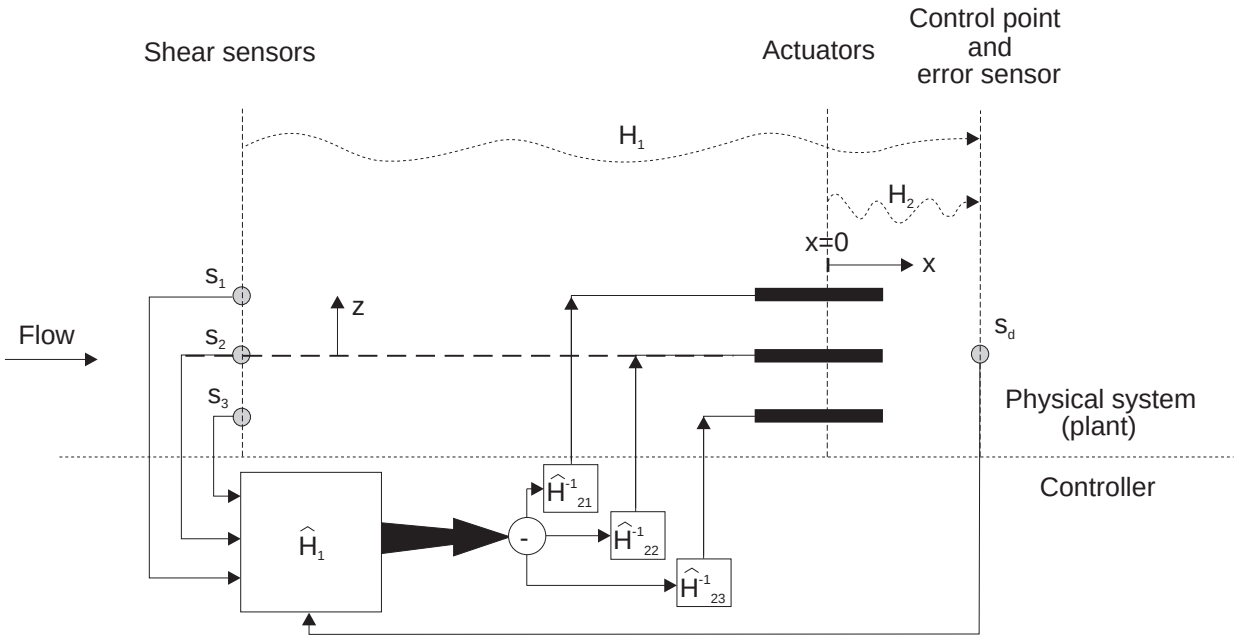

Figure 2.7: Schematic diagram showing the plant - the turbulent boundary layer - together with detection sensors (s_1, s_2 and s_3), actuators and a downstream sensor (s_d). The block diagram below the dotted line represents the controller, including the adaptive feedback path.

directly cancel the control variable at the designed downstream location. Thus the controller provided the actuators with a driving voltage that enabled them to produce an equal but negative response in control variable to that which was estimated by the linear predictor.

The cancellation scheme is an idealized solution and the error between the desired control effect (where the control variable is driven to zero) and the actual measured effect was used to assess the performance of the controller. A feedback path between the control variable, s_d and the controller enabled this error to be measured in real-time, allowing periodic modification to the controller parameters, if desired. In the next section, other methods for controller performance assessment are discussed.

2.6.1 Assessment of the Control Performance and Feedback

The control strategy described above may be applied to a wide range of problems. Its flexibility is apparent in the approach taken, whereby the problem is separated into two segments, namely system identification and control.

The identification procedure is divided into the characterization of the plant dynamics as well as the effect of the control input on the plant. Sensor signals are used to filter through upstream flow information, differentiating the important structures from the rest of the flow. The scales associated with the primary flow structures are emphasized and used to predict the downstream characteristics of the flow.

The effect of the actuators on the downstream flow conditions is characterized in terms of a transfer function between the input voltage and the measured quantity at the control points. The aim of reducing a particular flow variable at a control point is then achieved by linear cancellation through the combination of the predicted quantity and the influence of actuators on it. Note that any variable may be selected to be attenuated so long as it can be predicted and is influenced by the actuator.

In these experiments the control variables were chosen to be the streamwise velocity fluctuation and the wall pressure fluctuation. However, other variables of interest are wall shear stress, Reynolds stress and turbulent production, all of which are measurable quantities. Furthermore, since the actuator was designed to modify the large scale structures, it is clear that it will also have an effect on these other quantities that are primarily governed by the large scale dynamics. Thus if measurements of these parameters are taken, optimal filters can be designed to predict their downstream behavior. This prediction, together with the effect of the actuator on the chosen flow parameter, are combined to provide the appropriate control input for the linear cancellation at the control point.

As mentioned in the last section, the linear cancellation assumption is idealized and it is important to have an idea of how well the control objective is being met. The objective in these experiments was to reduce the fluctuations of the controlled variable at the design point. A direct measure of this was provided by its root-mean-squared value. In addition, its spectra indicated the frequency band over which the flow is effected by the applied control. Hence a performance index may be based on the root-mean-squared value while the modification of the filter parameters can be based on the measured spectra of the controlled variable.

Furthermore, since the large scale structures are assumed to contribute to a majority

of the turbulent dynamics in the near-wall region, a measure of their activity would give additional indication of the control effectiveness. One such measure, discussed in the introduction, is the bursting frequency and is computed by conditionally sampling a time series using the VITA technique [8, 4]. Another measure of the effect on coherent structures is their average size and orientation in the flow. Lorkowski *et al.* [46] showed that steady open-loop forcing in the turbulent inertial range increased the wall-normal and spanwise inclination of the coherent structures. Furthermore, a reduction in the spanwise correlation suggested a breaking-up of the large scale structures.

The results of the experiments will thus be illustrated in terms of root-mean-squared profiles. Spectra and correlation functions are used to illustrate the modification of the flow field and ,in particular, of the large scale dynamics. VITA events are examined to further quantify the effect of control on the evolution and development of these large scale structures.

Chapter 3

Experimental Setup

3.1 The Wind Tunnel Facility

3.1.1 The Tunnel and Flat Plate

All experiments are conducted in air, using a through-flow wind tunnel with a entry convergence ratio of 16:1 and a rectangular test-section measuring 0.61×0.91 m in cross-section and 3.66 m in length. The tunnel exhausts through a diffuser and a 9-blade fan into a large room that houses the entire tunnel. The tunnel maintains a steady freestream velocity range between 1 and 20 m/s with corresponding turbulence intensities between 0.1 and 0.05%, respectively.

The experiments are carried out on a flat plate that consists of a 0.1 m long semi-wedge leading edge inclined at 10^o on the non-working side. The trailing edge is fitted with a flat flap for the control of the leading edge stagnation line. The length of the plate, including flap, extends from approximately 0.5 m from the entrance of the test-section to its end. The plate was inclined to the flow to account for boundary layer growth down the tunnel and to maintain a zero pressure gradient. The plate and flap were inclined at 0.3^o and 15^o to the flow respectively. Further details of the tunnel and plate specifications are documented by Grimaldi [47].

All experiments were carried out in a fully developed, zero-pressure-gradient boundary layer with flow parameters given in Table 3.1. The friction velocity, $u_\tau = \sqrt{\tau_w/\rho}$, is a function of the wall shear stress, τ_w, and the fluid density, ρ. τ_w was measured with a Preston tube placed on the wall (wholly immersed in the inner region of the boundary layer), at the same streamwise position as the detection sensors. The calibration table used was that of Patel [48], which covers a wide range of flow conditions and tube sizes.

3.1.2 Data Acquisition and Processing

The primary data acquisition platform is a 16-channel, 12-bit, 1 MHz A/D board that includes a data-buffering feature for large, continuous data records. The signals are pre-

Re_x	8.1×10^5
Re_θ	1960
U_0	6 m/s
l^*	55μm
t^*	270μs
u_τ	0.31 m/s

Table 3.1: Table of flow parameters corresponding to the location of the experiment.

processed by 16-channel analog filter and amplifier boards for anti-aliasing and resolution enhancement. The input range of the A/D board is ± 5 V, corresponding to a resolution of 2.4 mV. To ensure the statistical convergence of the measured data, record lengths are based on a 95% confidence level with a 0.2% uncertainty in the root-mean-squared value. Assuming a normal distribution, this requires 1.3×10^6 independent sample points per record. This treatment requires that the sample points be independent and uncorrelated with each other. Note that this analysis was based on variables that have a normal distribution. Turbulence quantities are not normally distributed, but for large record lengths, the central limit theorem [39] states that as the number of records increases, the sum of any identically distributed variable has a normal distribution, regardless of their individual characteristics. Thus, this theorem may be applied when calculating the number of record lengths for statistical convergence - typically a very large number. In the current turbulent boundary layer flow, assuming typical correlation times of the order of $100t^*$, this implies sampling frequencies of less than 50 Hz. The constraint on the sampling frequency, however, prevents time-series data that contain information on correlated structures in the flow, which defeats the primary goal of these experiments. Thus, it was necessary to determine appropriate record lengths based on higher sampling frequencies. Lorkowski *et al.* [46] conducted convergence experiments and concluded that at higher sampling frequencies (that is, relative to the 'uncorrelated frequency' of 50Hz) the absolute error in the mean and root-mean-squared values of the measured quantity was only weakly dependent on the sampling frequency. The error was instead dependent only on the total time of each data set. On the basis of these results, all data records in the following experiments contain at least 2×10^6 sample points taken at 5kHz.

Digital Signal Processing

The control system is exclusively managed by an independent DSP processor (Innovative Integration, Model PC32). It features a 60 MHz processor with 4-channels of 16 bit A/D converters, each capable of sampling at 100kHz and 4-channels of 16 bit D/A converters at 100kHz per channel. A 4K on board dual port memory with a bus interface capable of 5 Mbytes/s is mapped onto the host PC and the DSP with arbitration to implement and run the controller transfer functions with programmable filter coefficients, bandwidth and amplitude.

Figure 3.1 is a block diagram of the hardware setup and illustrates this arbitration process.

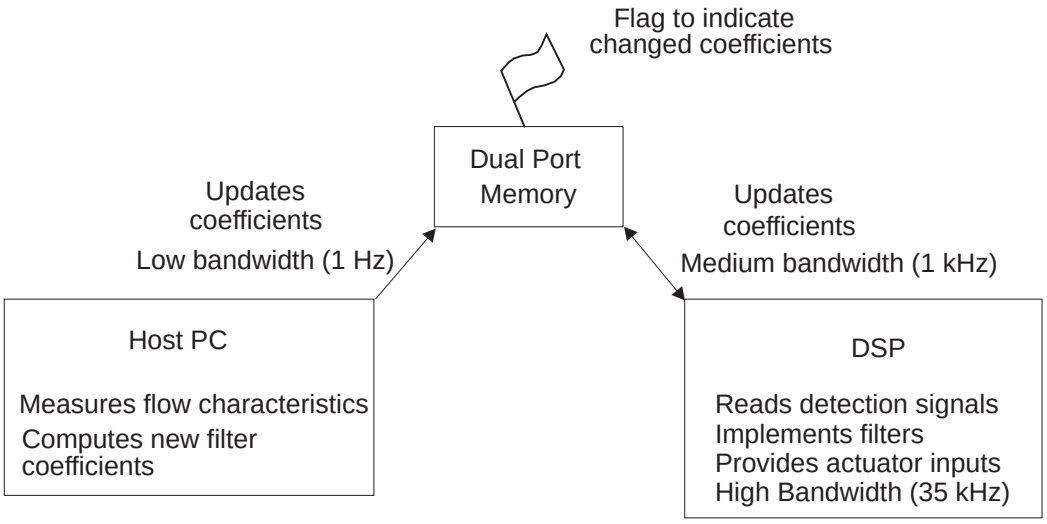

Figure 3.1: Flow diagram of the control architecture showing the host PC - DSP interface via the dual port memory. The host PC updated filter coefficients and placed them in memory and switching on a flag. The flag is periodically checked by the DSP and the coefficients are read when they have been modified.

The DSP reads in the sensor signals at 5kHz ($1.35f^*$) and processes them with the prediction filter coefficients to determine the downstream flow signal. This is then fed through the actuator transfer function, resulting in the actuator input signals required to cancel the fluctuations at the control points. The output from the DSP (which was connected to the actuator array) is composed of these signals multiplied by carrier signals at 2.3 kHz (corresponding to the average resonant frequency of the three actuators). The output is amplified by a factor of 18 with a custom-made power amplifier before it is used to drive the actuators.

The host computer reads in flow measurements from the downstream sensor and recomputes the new filter coefficients to reduce the error between the measured and desired output (zero root-mean-squared value). It then periodically writes the new coefficients into the dual port memory where a flag was set to indicate that the coefficients have been updated. The updating from host PC to the dual port memory was carried out with a low bandwidth of the order of 1 or 0.1 Hz since the computation of new filter coefficients requires large data sets to be read and processed.

The DSP checks the dual port memory for a triggered flag at a rate of 1 kHz and reads in the coefficients if they were updated. The new filter coefficients are then used for the real-time filtering of the upstream sensor signals.

All data acquisition and processing functions are carried out using Matlab software and signal processing tools. A spectral analyzer (Stanford Research Systems, Model SR780, 2-channel network signal analyzer) is also used to acquire real-time spectral and temporal characteristics.

3.1.3 Instrumentation

A custom-made 10-channel, constant temperature anemometer is used for all hot-wire measurements. The anemometer was designed with low-noise circuitry (less than 1 mV peak-to-peak noise level for ± 10 V signal range) and a built-in oscillator for frequency response adjustments. It also includes a variable gain amplifier (ranging between 1 and 96) and a variable cut-off lowpass anti-aliasing filter (ranging between 0.1 and 20 kHz).

A custom-made 10-channel, low-noise pre-amplifier circuit is used for conditioning the microphone signals for pressure measurements. Each channel includes a 5 kHz lowpass anti-aliasing filter and a variable gain amplifier (ranging between 10 and 1000).

A programmable signal generator is used to obtain frequency characteristics for the calibration of the microphone and actuators.

3.2 Sensors and Actuators

In order to implement an effective control strategy, the control hardware, namely sensors and actuators, must be accurately characterized. Sensor response and resolution determine the ability for candidate flow structures to be detected while actuator performance govern the control input required to achieve the desired objectives.

3.2.1 Velocity Sensor

Streamwise velocity is measured using a traversible hot-wire mounted on a sting. The home-made probe holds a platinum-tungsten wire 2.5μm in diameter and 0.5 mm in length ($0.05 \times 10l^*$). The wire is connected to the anemometer and run in constant temperature mode at a resistive overheat ratio of 1.6 and has typical cold resistances between 15 and 30 Ohms [47]. The dynamic response characteristics of the wire is set by measuring its response (in particular, its decay rate and hence damping ratio) to a square-wave input. All hot-wires were adjusted to have a bandwidth of 20 kHz and were operated with a typical signal to noise ratio greater than 500.

The probe was calibrated by placing it outside the boundary layer flow and measuring its output at different freestream velocities. The resulting relationship is then approximated by a least-squares polynomial fit. The calibration process was repeated periodically to account for any signal drift which was generally found to be negligible.

3.2.2 Wall Shear Sensor

The shear stress sensors used were flush-mounted hot-wires run in a constant temperature mode [49]. In these experiments, the sensors were used for the identification of the flow in the near-wall region. The sensors are most sensitive to the shear component normal to the axis of the wire. This result stems directly from hot-wire anemometry theory and requires that for a single wire (single component) measurement, the greatest heat loss is generated by this normal component. Hence for a two-dimensional flow, (with a mean streamwise shear

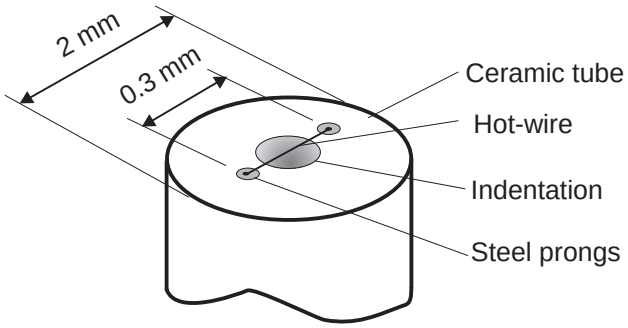

Figure 3.2: Schematic diagram of the shear stress sensor showing the hot-wire flush mounted between two steel prongs which are supported in a ceramic substrate.

component only) a wire aligned in the spanwise direction will provide the best measure of the streamwise shear.

A wire aligned in the *streamwise* direction will be sensitive to both the streamwise and spanwise shear components. However, the wire cannot differentiate between positive and negative spanwise shear fluctuations, since its mean component only comes from the streamwise shear. This results in a rectification of the spanwise shear fluctuations. The mean value of the signal will be dominated by the streamwise shear with a secondary component from the spanwise fluctuations due to this rectification. The fluctuating component will be dominated by this rectified spanwise component together with a secondary contribution from the fluctuating streamwise shear (since the loss of heat associated with this fluctuating component is comparable to that from the streamwise component if the wire was aligned in the spanwise direction). Thus a negative signal can arise only from a reduction in the streamwise shear component .

The signals from a spanwise array of sensors were connected to the inputs of an optimal linear predictor that estimated flow characteristics at downstream locations in real-time. The sensor signals were required as control inputs rather than for the accurate measurement of shear stress. It was thus not necessary for the value of shear stress to be known. The requirement was for a portion of the sensor signal to be linearly related to the downstream variable that is to be controlled. Hence, these detection sensors need not be calibrated (which saves on computational time) and their raw voltage outputs were used in the prediction of the downstream flow characteristics.

The sensors were made using a pair of stainless-steel prongs threaded through a ceramic tube with two isolated through-holes as illustrated in Figure 3.2. The prongs were set in place with epoxy and their tips were sanded flush with the ceramic tube. An indentation was then made between the prong tips to create an insulating air gap. A 0.3 mm long, 2.5μm diameter wire ($6 \times 0.05l^*$), corresponding to a length to diameter ratio, $L/D = 130$, was then spot welded between the prongs (Figure 3.2). The back-ends of the prongs were soldered to wires that then connect to the anemometer. The sensors were epoxied into circular ports made on the flat plate. They may be removed or rotated by applying heat to the bond. Due to their shorter lengths, the sensors had a typical resistance of between 10 and 20 Ohms. They were run at a resistive overheat of 1.6 and were tuned to have a bandwidth of 15 kHz.

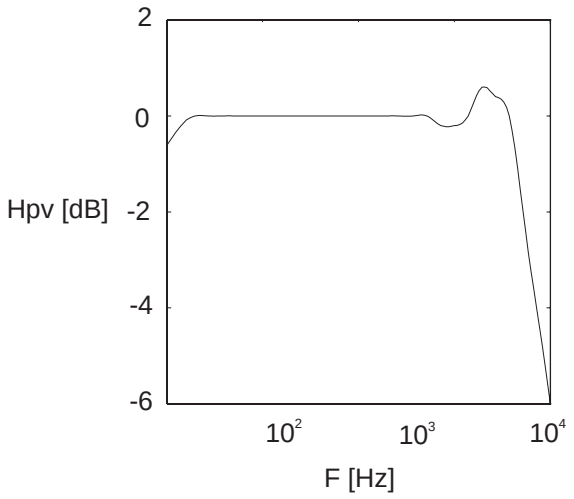

Figure 3.3: Calibrated frequency response of the Knowles microphone showing a uniform response between 30 Hz and 6.5 kHz.

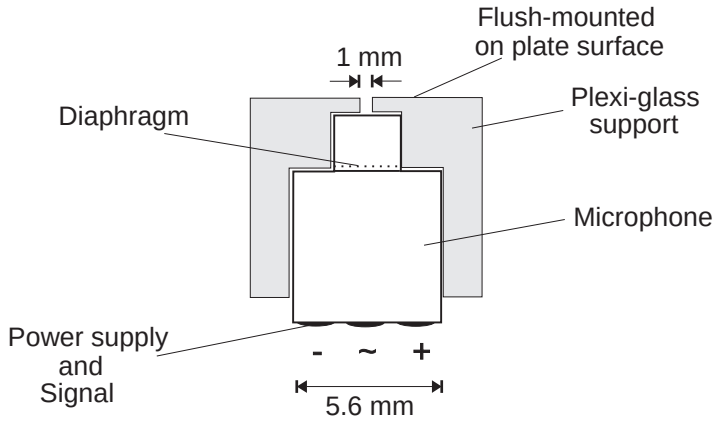

Figure 3.4: Schematic diagram of the microphone assembly. The microphone is press-fitted into a plexiglass socket that has an opening to the boundary layer flow.

3.2.3 Pressure Sensor

Pressure sensors were used in the control of the wall pressure fluctuations. The measurements were taken using a Knowles BL-1785 microphone. Its factory specifications for pressure sensitivity were first confirmed using an accurate 1/4 inch Bruel & Kjaer microphone whose frequency response was uniform from 30 Hz to 12 kHz. Both microphones were placed at one end of a chamber lined with acoustic foam (to minimize reflections), with a loudspeaker at the other end. The speaker was driven with a frequency-modulated sinusoidal signal that swept from 10 Hz through to 5 kHz. The cross spectrum between the two microphone signals then represents the 'true' Knowles' frequency response. This calibrated frequency response of the Knowles microphone is given in Figure 3.3 and is seen to be uniform from 30 Hz up to 6.5 kHz. In this frequency band, the output voltage from the pressure sensor is linearly related to the measured pressure.

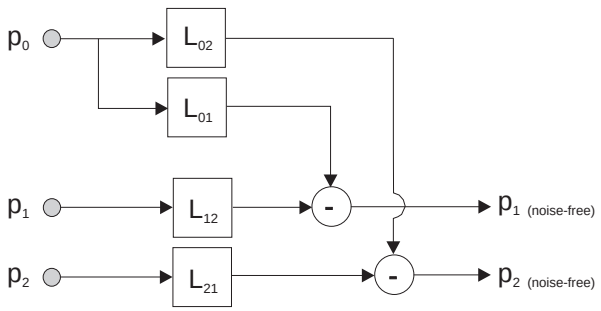

Figure 3.5: Diagram showing the arrangement of the pressure sensors. p_1 is the far-field sensor that was used to extract the background acoustic noise. p_2 and p_3 were the primary sensors whose noise-free signals were used used in the control scheme.

The microphone is fitted into a plexiglass socket that was fabricated with an access hole for the measurement of the wall pressure (Figure 3.4). The hole diameter measures 1 mm or $20l^*$, which was found by Schewe [50] to be the maximum allowable transducer size for the accurate measurements of the most significant contributions to the wall pressure signal. The depth of the hole was governed by the cavity impedance that acts as a lowpass filter for the pressure fluctuation at the wall. This Helmholtz resonator effect was set at 50 kHz with a 1 mm deep hole (taking into account the cavity between the mouth of the microphone and the diaphragm).

Signal Conditioning

The pressure signal in the boundary layer is particularly susceptible to background acoustic noise. These tend to occur at the low-frequency, high-energy end of the spectrum and hence may overwhelm the contributions from the boundary layer flow. However, the large-wavelength nature of the acoustic noise may be used to eliminate it from the measured signal by introducing a second, far-field microphone. This technique was successfully employed by Naguib *et al.* [51] for noise-canceled pressure measurements in a turbulent boundary layer.

In these experiments, three primary microphones were placed in an array, $200l^*$ downstream of the actuators and $40l^*$ apart in the spanwise direction. The far field microphone was located at the same streamwise location as the primary array, but approximately $1200l^*$ away from the center sensor in the spanwise direction. This separation is an order of magnitude larger than a typical distance between coherent structures and should guarantee that the turbulent signal measured by the primary and far field sensors are uncorrelated. The separation corresponds to a wavelength of 6 cm which implies that planar acoustic modes with longer wavelengths were filtered out using the conditioned spectral analysis. A schematic diagram illustrating the location of the sensors is given in Figure 3.5.

Using the conditional spectral analysis technique described in Section 2.5, the portion of the primary signal that is uncorrelated with the far field signal will thus represent the undisturbed turbulent pressure. Furthermore, in an effort to increase the effectiveness of controlling the pressure signal associated with the coherent structures, conditioned spectral analysis was also applied between adjacent microphone signals. The correlated parts of the

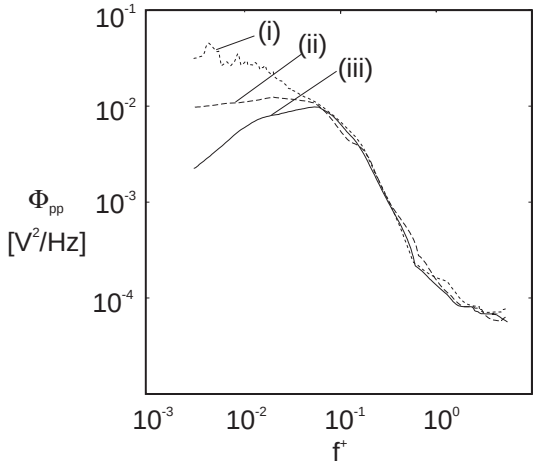

Figure 3.6: Spectra of the wall pressure, (i) with the raw sensor signal, (ii) with the acoustic noise removed and (iii) with only the correlated part of adjacent sensors used to emphasize the coherent structures in the boundary layer.

signals were then used as the control variable, isolating the coherent motion. For example, the noise-free portion of p_2 is written as:

$$p_{2(noise-free)} = L_{21}\{p_2\} - L_{20}\{p_0\}, \tag{3.1}$$

where L_{ij} is the filter that represents the correlated portion between p_i and p_j. All pressure measurements presented here were pre-conditioned in this manner to remove the large scale background noise. The conditioning of the pressure signals is illustrated in Figure 3.5.

Figure 3.6 is a plot of three pressure spectra corresponding to the raw sensor signal, the acoustic noise-free signal and the noise-free signal that has been enhanced to emphasize frequencies corresponding to coherent structures in the boundary layer. The extraction of the acoustic modes has a marked effect on the low frequency peaks in the raw spectra. The peaks have been suppressed to give a much smoother, broad-band spectrum. In emphasizing the frequency bands associated with the coherent structures in the wall flow, the modified spectrum exhibits a peak over the corresponding frequency band. The signal associated with this final spectrum will thus be that which most accurately describes the dynamics of the large scale coherent structures in the wall region. This form of the signal was used in the control of the wall pressure fluctuations in the following experiments.

3.2.4 Actuators

Physical Requirements

For practical flow control purposes, the length, time and velocity scales of an actuator must be comparable to those associated with the flow so as to achieve full controllability. The average scales associated with coherent structures in the wall region of a turbulent boundary layer were discussed in the introduction and provide a convenient guide for the

design of actuators in the control of turbulent flows. Rathnasingham and Breuer [52] have also developed scaling arguments relating actuator performance in various turbulent flow regimes in terms of the operating Reynolds number.

In this section, the design and fabrication of the resonant actuators used in these experiments are discussed. The design approach was mainly governed by the fluid and structural characteristics of the devices and the requirements imposed by the turbulent flow.

Resonant Actuator Concept

The actuators used in these experiments were zero mass-flow, resonant devices based on the concept first proposed by Coe *et al.* [53]. Their device consisted of a thin membrane, rigidly fixed at its edges and driven into transverse oscillations at its resonant frequency. The membrane made up an end wall of a closed, cylindrical cavity. The opposite wall was rigid and contained a small orifice. As the membrane deflects to compress the fluid in the cavity, the rise in pressure drove fluid out through the orifice. The outflow separated at the edge of the orifice and emerged as a normal jet. When the membrane deflected in the opposite direction, the orifice acted as a sink and fluid was drawn into the cavity from all directions. The differences between the inflow and outflow resulted in a time-averaged flow field resembling a vortex ring over the orifice with a steady jet emanating outwards from its core. Coe *et al.* [53] fabricated a micro-machined actuator with orifice diameters of 150-300 μm that achieved jet velocities of 17 m/s and penetration depths of 500 orifice diameters. Similar devices were also used to achieve jet thrust vectoring. An experimental investigation of the jet produced by a similar macro-sized device has also been carried out by James *et al.* [54].

Another actuator design was first proposed by Jacobson and Reynolds [55] [27] and comprised of a piezo-ceramic/metal shim heterogeneous bimorph cantilever, mounted eccentrically over an open cavity. The cantilever was driven at resonance and the oscillatory cavity pressure created, in turn, drove an unsteady flow through the cavity gaps. The time-averaged flow field over the narrower gap resembles a pair of line vortices accompanied by a normal jet. Mass conservation requires that a much less intense flow develop over the larger gap. An array of devices were used in series with shear stress sensors for transition and turbulence control [56] and had produced encouraging results. Saddoughi [57] also developed a larger devices to be used as a vortex generator for the control of boundary layer separation.

The actuators used in these experiments combine the designs of the two devices described above. A schematic diagram is shown in Figure 3.7. They comprised of a close cavity with an oscillating wall, as in the device used by Coe *et al.*, but have an exit *slit* to produce an output flow that resembles that described by Jacobson and Reynolds. A pair of longitudinal vortices aligned in the streamwise direction resemble low-speed streaks and may be best suited to control them. Figure 3.7 illustrates the time-averaged outflow from the slit. Note that the actuator is limited to producing an outflow only, so that a negative or positive driving input will result in the same blowing jet. An array of such devices were designed and optimized based on their structural and fluid characteristics.

Note that these devices, although characterized by a single frequency, may be driven with amplitude modulated signals at frequencies to which the global flow is receptive. This idea

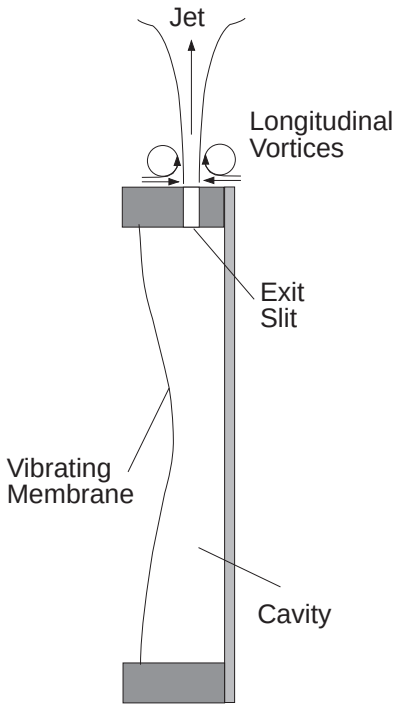

Figure 3.7: Schematic diagram of the actuator with the resultant jet flow out of the exit slit.

was first demonstrated by Wiltse and Glezer [58] in the control of free shear flows.

Actuator Design

The oscillating flow in the slit introduces viscous effects that are analogous to those found in the Stokes' oscillating plate problem [59]. These viscous effects lead to a boundary layer in the slit whose thickness is governed by the viscosity and the frequency of oscillation and the resulting velocity profile may be expressed in terms of the Stokes' parameter, $St = \sqrt{\omega d^2/\nu}$, where ω is the driving frequency, d is the slit width and ν is the fluid kinematic viscosity.

It may be shown that the Stokes' parameter governs the outflow characteristics and leads to a critical value for the slit area, below which viscous effects dominate [52]. The critical value arises from the matching of the viscous and inviscid flow regimes in the flow through the slit. The viscous dominated flow occurs when St is small and the boundary layer within the slit spans its entire width. As St increases the mass flow through the slit increases with the slit area. For large St, the boundary layer in the slit is isolated close to its edges and incompressible theory requires that the mass flow decreases with the slit area. This conflicting variation of the mass flow through the slit, implies that the optimum performance is achieved when the mass flow in the two regimes are matched. This results in an optimum value for the slit area for which the actuator attains its peak performance.

The physical parameters of the actuator were chosen so as to optimize its performance according to its corresponding optimal slit area. The width and length of the slit measured $10 \times 150l^*$ and were chosen to be fractions of the typical dimensions of coherent structures ($\approx 40 \times 500l^*$). A spanwise array of three such actuators were used in these experiments.

Their spanwise separation was designed to be $40l^*$, approximately one half of the typical spanwise separation of the large scale, low-speed streaks. This represented the maximum separation allowable for adequate controllability of these structures.

The efficiency of the device was also examined by Rathnasingham and Breuer [60] in terms of the losses associated with driving the flow out of the slit. These losses were expressed in terms of the kinetic energy, which was obtained by integrating the velocity profile at the exit of the slit over a period of oscillation. They represent the viscous losses in the flow. The losses associated with the forcing method was neglected. Values above fabricated device operating at a suitably high value of St (> 10).

Fabrication

The single actuator unit shown in Figure 3.8a was made using a 170μm thick brass shim sandwiched between two steel washers to make a 25.4 mm diameter membrane. A small rectangular Nickel plated PZT-5H piezo-ceramic (250μm thick) was bonded (using epoxy and silver paint) with one short edge rigidly fixed to the edge support. Since the purpose of the piezo-ceramic was only to excite the membrane at its resonant frequency, it may be small compared to the membrane size so as to minimize the interference on the motion of the membrane. In this case, it measured 3 mm in length and 1 mm wide. Contact wires (24 awg) were soldered onto the membrane and the ceramic. A second 'spacer' shim (0.5 mm or $10l^*$ thick) and a rigid plate were then bonded onto the washer to complete a single device (Figure 3.8a). The 'spacer' shim was a slotted annulus that was used to define the width and length of the jet exit hole which was a 8 mm ($150l^*$) long 0.5 mm ($10l^*$) wide rectangular slit. The rigid plate made the other wall of the cavity that measures 1.2 mm deep. The jet exit slit was made on the edge of the unit by milling through the washers and shims to the edge of the cavity (shown by the dotted line in Figure 3.8a). Three such devices are sandwiched together to produce three slits, 2 mm ($40l^*$) apart as shown in Figure 3.8b. Figure 3.8c is a plan view of the actuator assembly showing the exposed area with the slits aligned in the streamwise direction relative to the flow.

3.2.5 Actuator Structural Characteristics

In order to use a device to its full potential in flow control, it is vital that its dynamic behavior be fully understood. The device must be accurately characterized to obtain a transfer function between the input (voltage) and output (mass ejection). The input-output transfer function of the actuator provided its frequency characteristics and completes the forward path of the control loop. This was computed by driving the actuator through a continuous frequency band and recording the velocity output through the slit. The transfer function is derived from the cross-spectra between the input voltage and the output velocity. The results for the three actuators are shown in Figure 3.9a and clearly indicates the resonant frequencies of approximately 1.8 kHz. This characterization of the first mode was adequate for low amplitudes ($< 130V$), but super-harmonics, shifts in the resonant frequency and other non-linear effects were introduced with higher forcing amplitudes [52, 60]. The resonant frequency of the three actuators are slightly different (mainly due to manufacturing

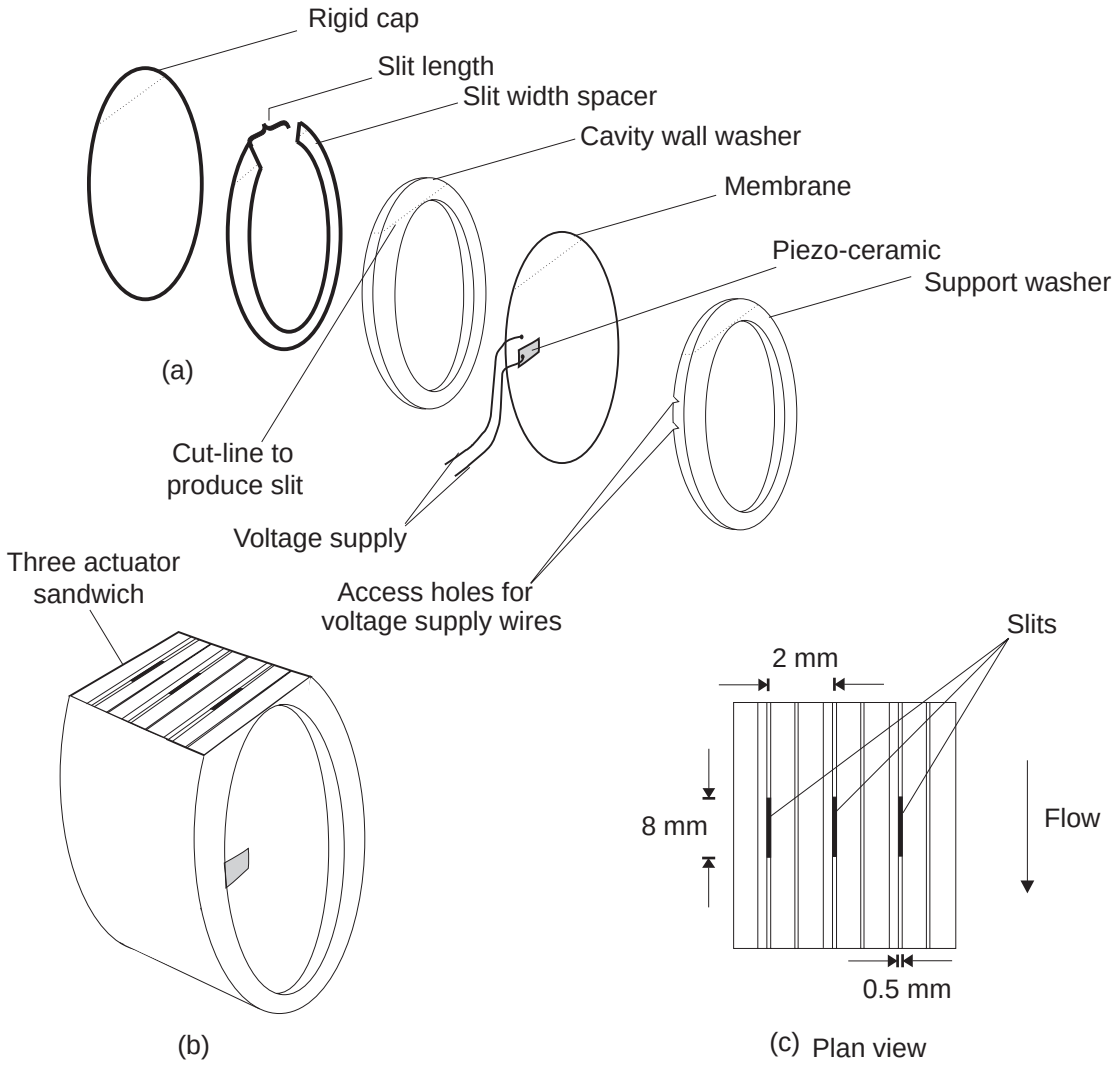

Figure 3.8: The resonant actuator assembly. (a) shows the multiple layers that are bonded together to produce a single actuator. (b) shows a perspective view of the assembly and (c) illustrates the plan view with the slit array that will be flush-mounted to the flat plate surface.

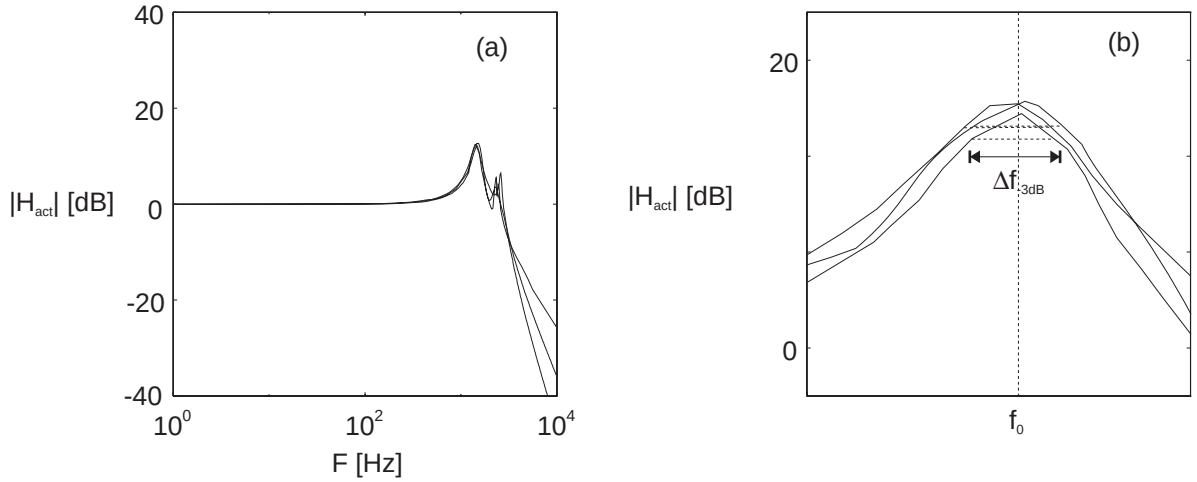

Figure 3.9: The actuator transfer functions plotted about their resonant frequencies. (a) The resonant peak of all three actuators occur approximately at 1.8 kHz. (b) Details of the resonant peak of the actuators used to compute their damping ratios and rise times.

inaccuracies) but for the ease of multiple actuator control, all three will be driven at a single frequency, without much loss in effectiveness. The character of the resonance peak can provide a measure of the actuator response. Assuming a second order system, the damping ratio was computed as follows [61];

$$\zeta \;=\; \Delta f_{-3dB}/2f_0, \tag{3.2}$$

where Δf_{-3dB} is the width of the peak at half the maximum power (i.e. -3dB below the maximum value) and f_0 is the resonance frequency. The rise-time, defined as the time taken for the output to attain 90% of a step input steady state, can be expressed as;

$$t_r \;=\; \frac{1}{2f_0\zeta} \tag{3.3}$$

and is a measure of the response time of the jet to an input voltage. Figure 3.9b shows the resonant peaks and illustrates the appropriate quantities that may be extracted from them. The computed rise time for the actuators was approximately 3ms which corresponds to 5 cycles at the resonant frequency of 2.3 kHz and $\Delta f_{-3dB} = 310$Hz. This agreed well with the measured rise time of 3.3 ms.

In practice, the actuator inputs were functions of the magnitude of the controlled flow parameter in the boundary layer, so that the actuators were never forced from rest. This meant that the rise-time was not crucial in implementation of the controller. Note that a compensator could always be designed to achieve the required dynamics, so long as it was structurally viable.

3.2.6 Actuator Jet Characteristics

The jet characteristics were investigated by using a traversible hot-wire to measure its axial velocity component. The hot-wire probe was traversed across the jet at different axial

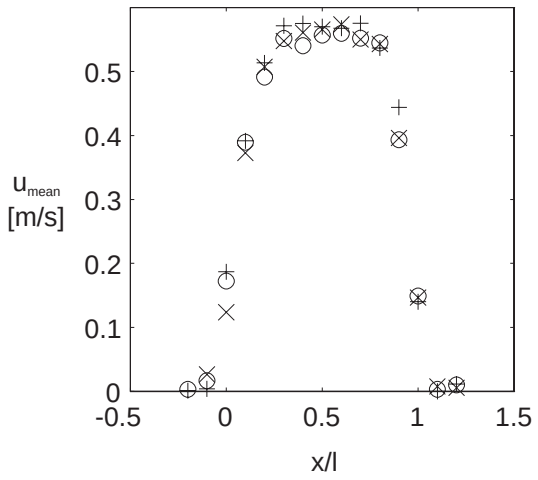

Figure 3.10: Mean jet velocity profile along the three actuator slits showing that a uniform jet velocity is obtained over most of its length. The measurement is taken at a distance from the slits corresponding to the maximum velocity in the axial direction. An input voltage of 100 V is used to attain a maximum velocity of 0.58 m/s or $1.8u_\tau$. $x/l = 0$ and $x/l = 1$ corresponds to the upstream and downstream ends of the slits, respectively. The symbols correspond to the three different actuators.

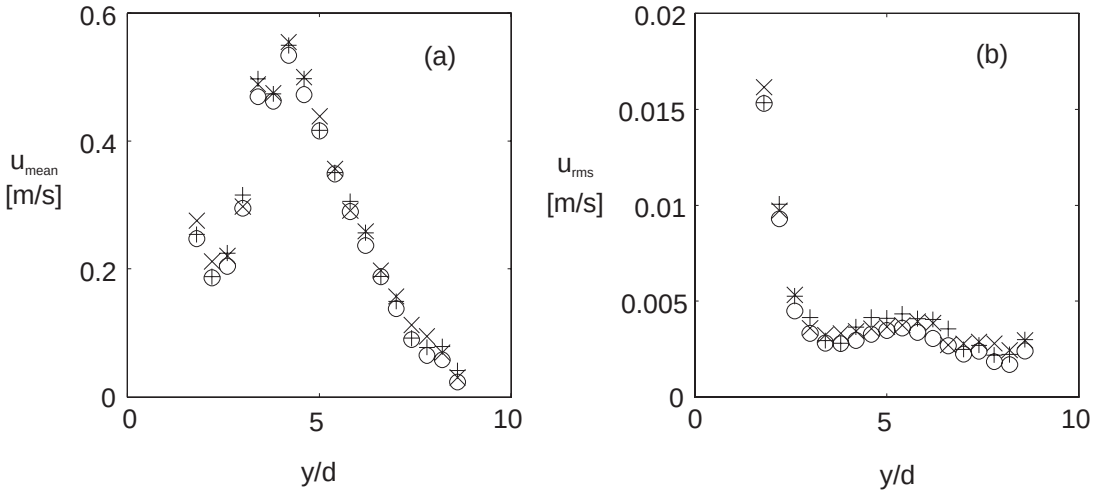

Figure 3.11: Jet velocity profiles in the normalized, wall-normal (axial) direction taken for the three actuators. (a) The mean velocity profile shows an initial rise to the maximum value (when the jet is fully developed) before decaying as a 2-D jet. (b) The root-mean-squared profile shows the high-energy fluctuations corresponding to the vortices, concentrated close to the slits, before the jet is fully developed. Measurements were taken at $x = 0.5$ (the middle of the slit). The symbols correspond to the three different actuators.

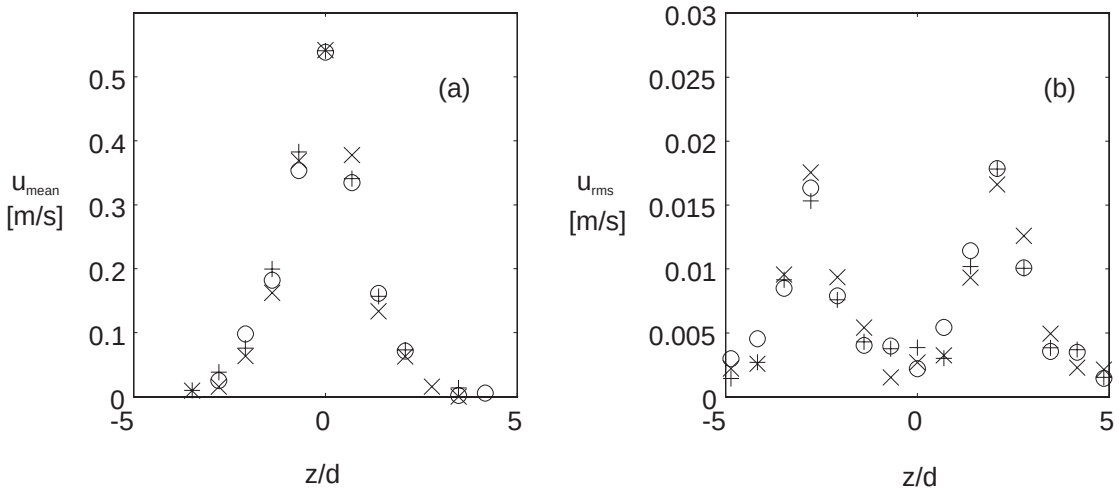

Figure 3.12: Jet velocity profiles in the normalized, spanwise (cross-stream) direction taken for the three actuators.(a) The mean velocity profile shows the jet flow centered about the slits. (b) The root-mean-squared profile shows the vortices as two concentrated peaks approximately 2 slit widths ($20l^*$) on either sides of the slits. Measurements were taken at $y/d = 5$. The symbols correspond to the three different actuators and the slit is centered on the origin.

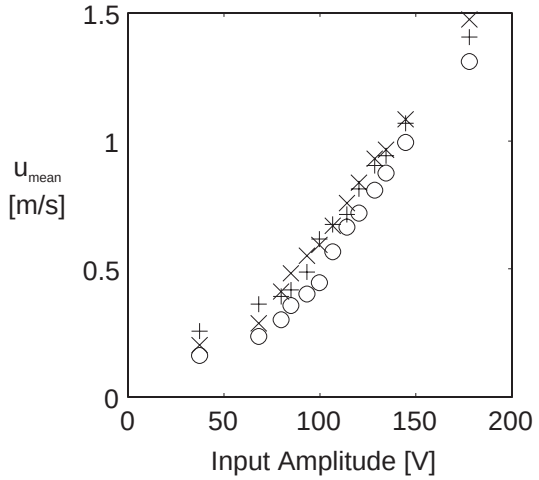

Figure 3.13: Maximum jet velocity over the range of forcing amplitudes, indicating a lower threshold of approximately 60 V below which viscous effects dominate and the jet fails to fully develop. The symbols correspond to the three different actuators.

distances from the exit to measure velocity profiles and range of influence. Using the convergence results of Lorkowski *et al.* [46], the mean and fluctuating velocity was measured with an average error of ± 0.02 m/s and ± 0.01 m/s, respectively.

Figure 3.10 is the plot of the axial velocity along the length of the slit and shows that the jet is maintained for approximately 60% of the slit length and vanishes rapidly at the edges. The profiles were measured at the height corresponding to the maximum jet velocity ($y/d = 5$).

Figure 3.11a is a plot of the mean axial velocity in the direction normal to the wall, y, normalized by the slit width, d, with an input voltage of 100 V. It shows an increase to a maximum value of 0.58 m/s ($1.8u_\tau$) at a distance of $y/d = 2$ ($20l^*$), followed by a steady reduction typical of a fully developed two dimensional jet [38]. At this forcing voltage, the jet extends as far as $8d$ ($80l^*$) away from the exit. Figure 3.11b is a plot of the root-mean-squared axial velocity profile and clearly indicates the high-energy fluctuations associated with the longitudinal vortices on either sides of the slit. This is seen to fall rapidly with axial distance and reaches a steady value beyond $y/d = 3$ which suggests that the vortices are isolated close to the slit.

The spanwise profiles are shown in Figures 3.12a and b. The mean profile (Figure 3.12a) clearly indicates that the jet is concentrated at the slit, while the twin peaks in the root-mean-squared profile (Figure 3.12b) confirms that the jet is sandwiched between the two vortices, located approximately 2 slit widths ($20l^*$) on either sides of the slit.

Figure 3.13 is a plot of the maximum jet velocity with input voltage. There is a lower voltage threshold of approximately 60 V below which the jet diminishes. This is a consequence of the low velocities and hence Reynolds numbers that cause viscous forces to dominate in the slit [52].

Steady Forcing

Lorkowski *et al.* [46] measured the streamwise velocity in the turbulent boundary layer just downstream of an actuator slit while forcing at a constant amplitude (steady forcing). Figure 3.14 illustrates the flow pattern as a contour map (in the $y - z$ plane) of the increase in the mean streamwise velocity. The vortical structures are centered about the slit and are seen to be approximately $10l^*$ in diameter and are separated by $40l^*$. These correspond well with the profile in Figure 3.12. Further details regarding the characteristics and evolution of these vortices are discussed by them. They also measured mean and root-mean-squared streamwise velocity profiles downstream of the actuator. Figure 3.15a is a plot of the mean profile taken directly downstream of the actuator. It illustrates the region of lower-speed fluid that results from the effect of the actuator output jet. The root-mean-squared profile (Figure 3.15b) indicates that the location of its maximum is located further from the wall, suggesting that the point of maximum turbulent production may also be shifted further out into the boundary layer.

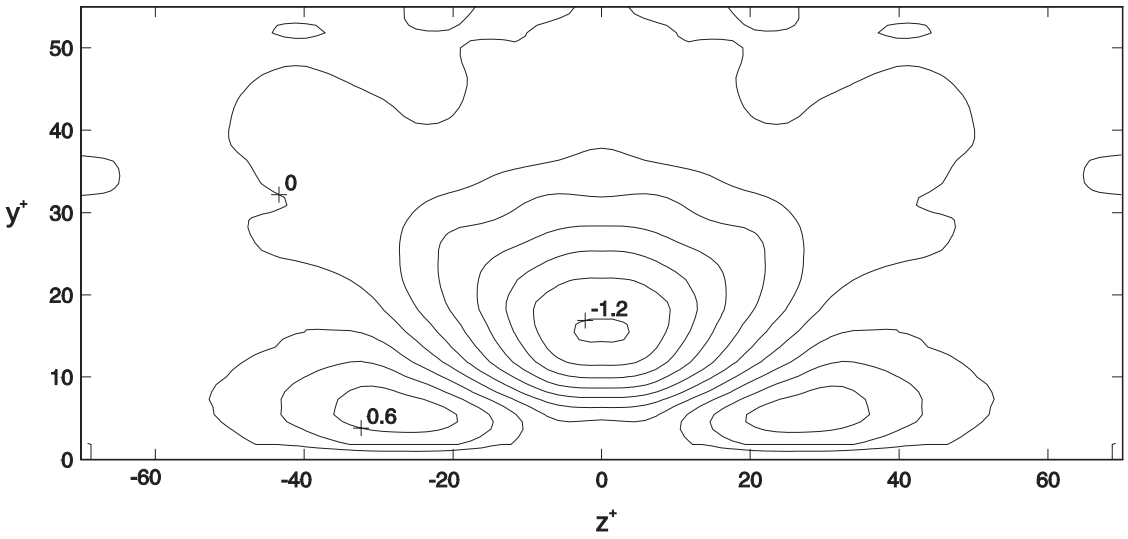

Figure 3.14: Contour plots of the change in the mean streamwise velocity at $60l^*$ downstream of the end of the slit. The vortices have maintained their relative positions (separated by $40l^*$ or 4 slit widths and centered about the slit) as they convected downstream [38].

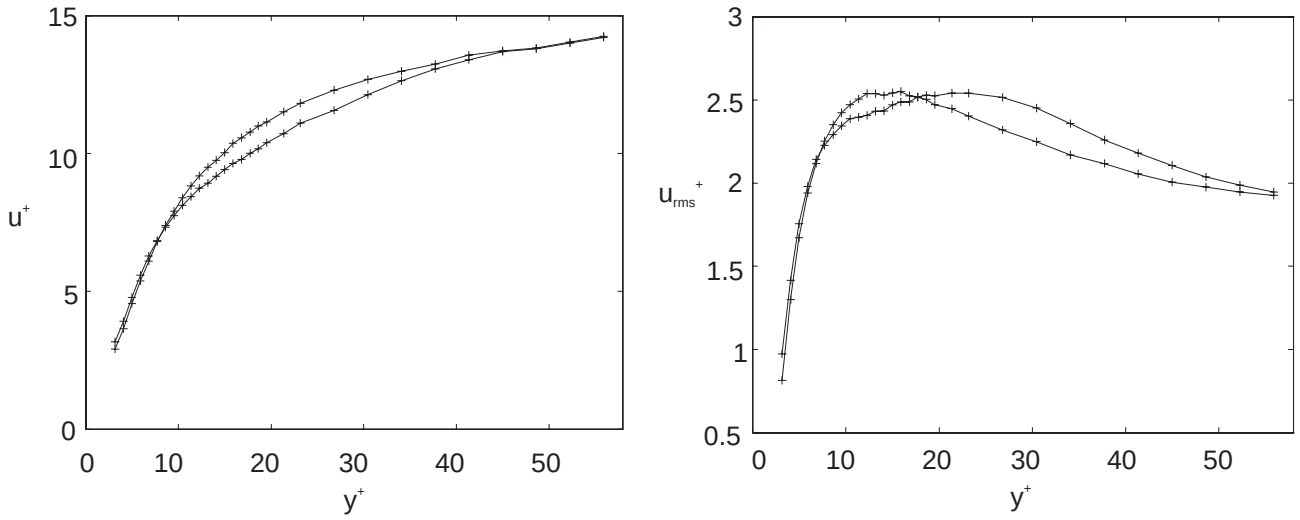

Figure 3.15: Mean and root-mean-squared profiles, $60l^*$ downstream of the actuator. The injection of low-speed fluid is seen in the mean profile, while the root-mean-squared profile shows a maximum value further away from the wall in the forced case. (Soild line: unforced, dashed line:forced).

Chapter 4

Results and Discussion

4.1 The Turbulent Boundary Layer

The local boundary layer velocity profiles are shown in Figure 4.1. The profiles compare well with past data of Purtell *et al.* [62] and numerical simulation of Kim *et al.* [63].

The mean velocity profile is seen to exhibit a linear near-wall region for $y^+ < 7$, a log-law region for $30 < y^+ < 100$ and a outer wake region for $y > 200$. The logarithmic region is well matched to the Clauser profile with a gradient of 2.5 and an intercept of 5.0 [59]. The mean wall shear stress, obtained using the Clauser profiles, was equal to 0.116, corresponding to a friction velocity, $u_\tau = 0.31$ m/s. The peak value in the root-mean-squared profile ($u_{rms} = 2.6u_\tau$) occurs at $y^+ = 12$ and coincides with the zero-crossing of the skewness and the point of minimum flatness [64].

4.2 System Identification

The proposed technique of identifying coherent structures from near wall turbulent signals and predicting their downstream effects was discussed in Section 2.5. It relies on combining the coherent parts of the signals from a spanwise array of sensors to design a system of multiple-input optimal filters. In this section, the results of various experiments, conducted to determine this optimal identification procedure is discussed. The primary issues stem from consideration of sensor orientation and configuration, optimal filter design and prediction and performance assessments. The aim is to optimally identify the characteristics of a chosen variable at a given downstream location using the detection sensors.

4.2.1 Sensor Performance

As mentioned in Section 3.2.2, the signal measured by the wall-wires depends on their orientation to the flow. When the wires are oriented normal to the flow direction, they are most sensitive to streamwise shear, while wires aligned to the flow are more sensitive to spanwise shear. To illustrate the differences between the two measurements in terms of their ability

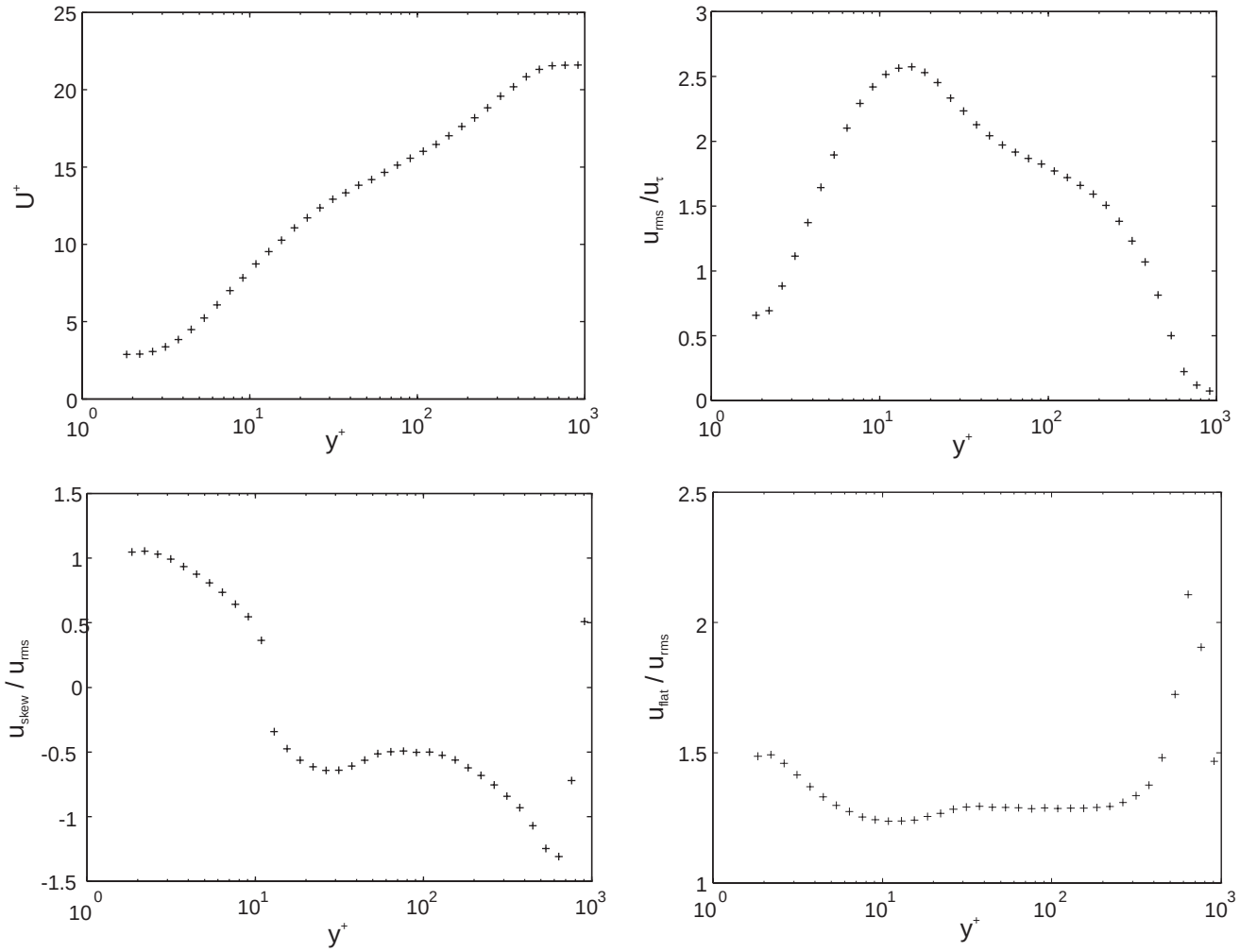

Figure 4.1: Wall-normal profiles of the first four statistical moments of the streamwise velocity in the turbulent boundary layer ($Re_\theta = 1960$).

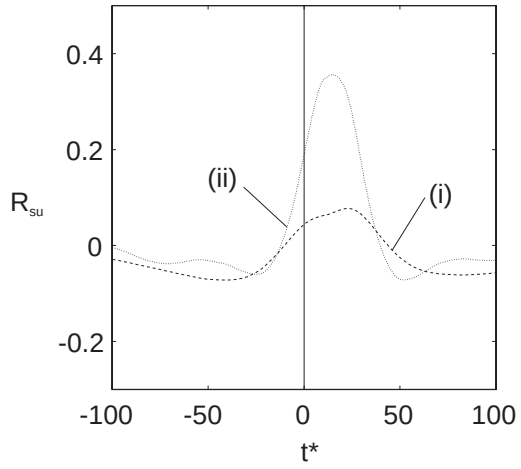

Figure 4.2: Cross-correlation between the upstream sensor and the downstream velocity (located at $300x^+$ downstream, $40z^+$ and $10y^+$ relative to the upstream sensor). The two curves represent (i) the sensor aligned in the spanwise direction (most sensitive to streamwise shear) and (ii) the sensor aligned in the streamwise direction (most sensitive to spanwise shear).

to predict the downstream flow, Figure 4.2 shows a plot of the cross-correlation function between a sensor and a downstream velocity hot-wire (placed $300l^*$ downstream and offset by $40l^*$ in the spanwise direction). Figure 4.2(i) shows that the streamwise shear correlates rather poorly with the downstream signal with a maximum correlation of 0.1. However, recent numerical experiments by Lee *et al.* [34] indicate that the spanwise shear appears to be a more effective control input. Orienting the sensor wires so that they were aligned in the streamwise direction (hence making them more sensitive to spanwise shear) produces a marked improvement in the cross-correlation which increases from 0.1 to 0.4. Due to this increase in the correlation coefficient and the consequent improvement to the prediction of the downstream control variable, this configuration (where the wires are oriented in the streamwise direction) was adopted for all subsequent identification and detection schemes.

4.2.2 Optimal Linear Prediction: Frequency Description

In order to assess the relative contribution of each sensor to the identification of the large scale flow structures, it was instructive to explore, in greater detail, the quantitative improvements of using multiple sensors. This is most clearly represented by the effectiveness of predicting the downstream variable as a function of sensor numbers and relative position. This effectiveness may be expressed as the difference between the measured and predicted root-mean-squared value of the predicted variable. Further insight may be obtained from the differences in the measured and predicted cross-spectra between the detection sensors and the downstream variable. The latter provides a convenient way to judge the accuracy of predicting particular frequencies. In the following discussion, the measured variable was chosen to be the streamwise velocity, $300l^*$ downstream of the sensor array, at $y^+ = 10$.

Figures 4.3, 4.4, 4.5 and 4.6 illustrate the effectiveness of various detection sensor con-

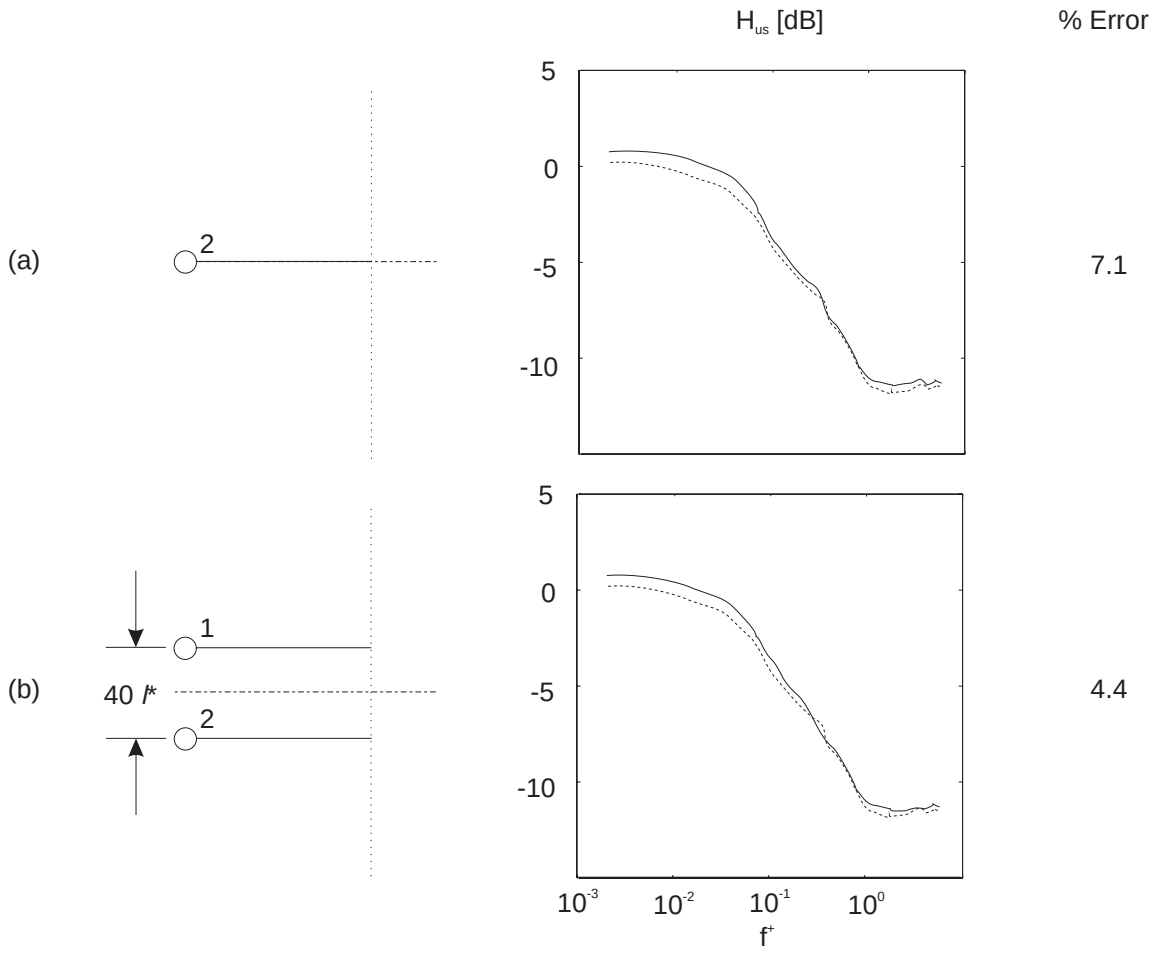

Figure 4.3: Cross-spectra between the detection sensors and the streamwise velocity $300l^*$ downstream; (a) with a single sensor directly upstream of the measurement point, (b) with a pair of sensors separated by $40l^*$ in the spanwise direction. The dashed-dotted line represents the line that passes through the downstream measurement point

figurations in predicting the downstream variable. Note that all sensors were run with the wires aligned to the flow, making them most sensitive to the fluctuating spanwise shear. The figures are separated into three columns. The first shows the sensor configuration in terms of number of sensors and relative positions. The dashed-dotted line represents the line that passes through the point, $300l^*$ downstream, where the predicted variable is measured. The second column in the figures compares the measured (dashed line) and predicted (solid line) cross-spectra. This provides a useful insight into the frequency bands that are most accurately predicted. The third column represents the root-mean-squared error between the predicted and measured u. This value acts as a performance index, allowing the selection of the most accurate configuration.

Figure 4.3 shows the prediction results for a single in-line sensor and a pair of sensors separated by $40l^*$ centered about the downstream measurement point. The single sensor predicts u with an error of 7.1% but the use of a pair of sensors makes a marked improvement,

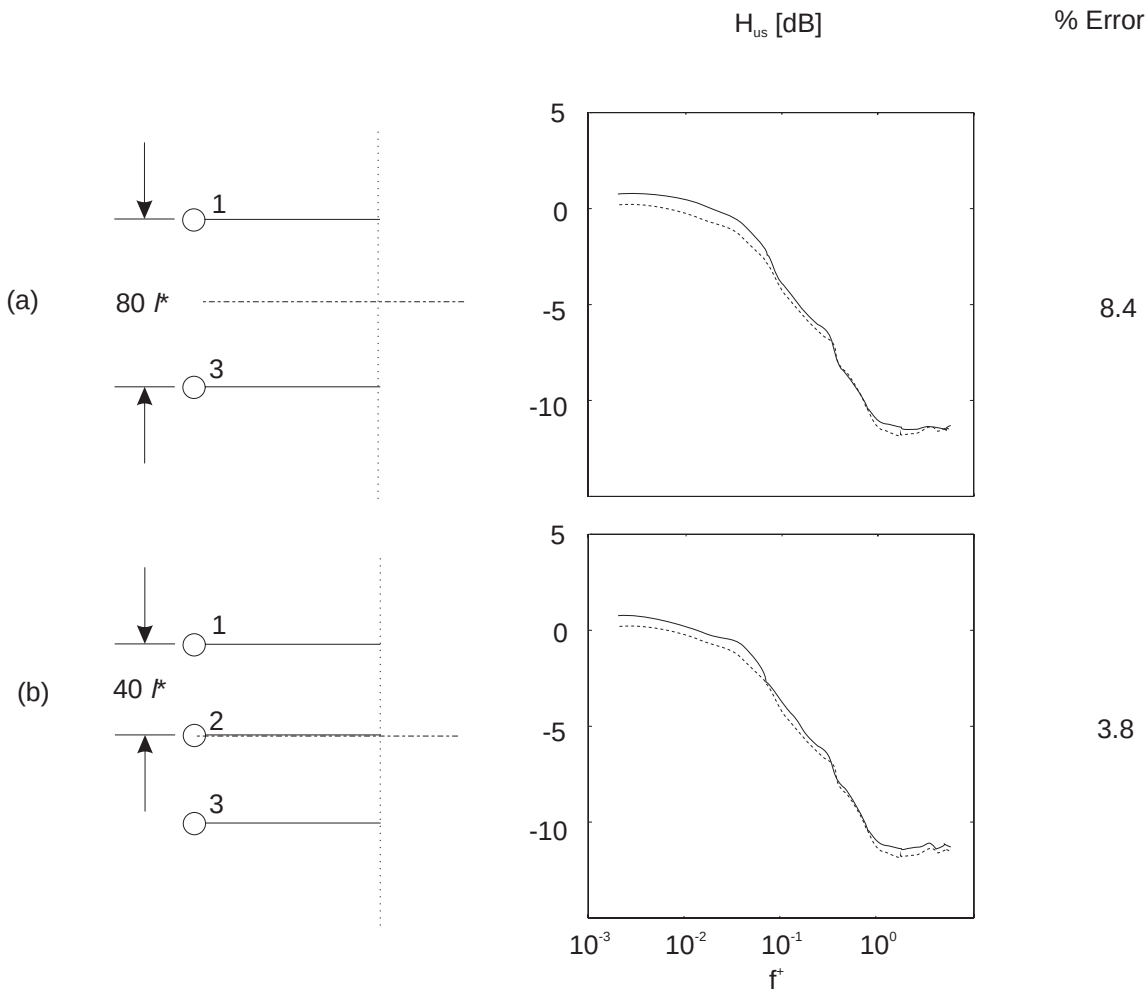

Figure 4.4: Cross-spectra between upstream detection sensors and the streamwise velocity $300l^*$ downstream; (a) with a pair of sensors separated by $80l^*$ in the spanwise direction, (b) with three sensors separated by $40l^*$ and centered about the downstream measurement point.

reducing this error to 4.4%. The increased performance of the second configuration suggests that the flow structures that contribute to the linear relationship between the upstream and downstream signals possess some degree of spanwise spatial coherence - either in terms of physical size or a meandering convection path. The obvious question that arises from this result is that to what extent is spanwise resolution beneficial. The extent of the spatial coherence may be investigated by considering a pair of sensors with a wider separation as shown in Figure 4.4a. With a separation of $80l^*$, the prediction error almost doubles to 8.4% suggesting an outer limit to the spatial coherence. This corresponds well to the spatial extent of coherent structures which is typically $100l^*$.

In an effort to improve the prediction error while maintaining the largest possible spanwise extent, an additional sensor was added to the configuration as shown in Figure 4.4b. Now the separation between sensors is reduced to $40l^*$ and the corresponding prediction

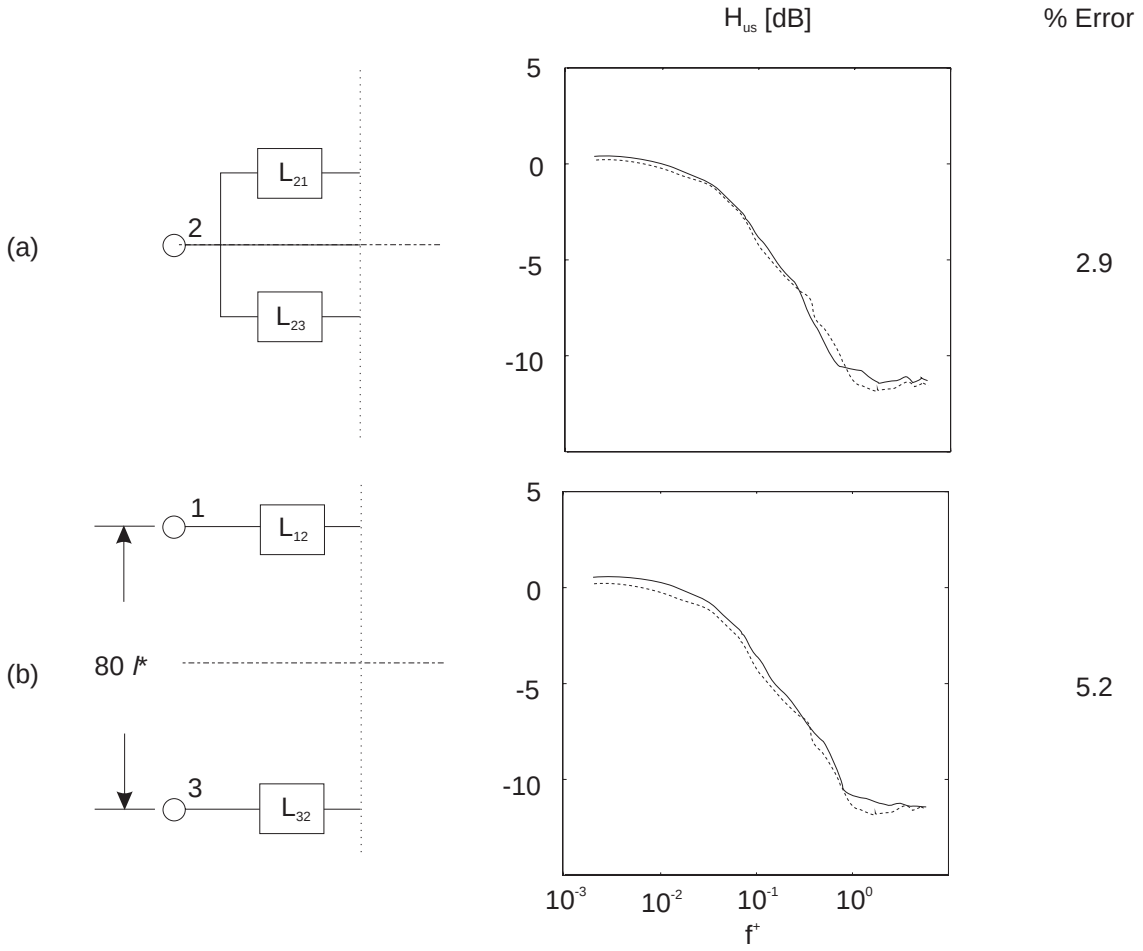

Figure 4.5: Cross-spectra between upstream detection sensors and the streamwise velocity $300l^*$ downstream; (a) with a single sensor whose signal is filtered to emphasize the most coherent structures in the flow, (b) a pair of sensors separated by $80l^*$ and filtered to emphasize the large scale motion.

error falls to 3.8%. This represents the optimal configuration for predicting the downstream variable with the raw signals from detection sensors. No condition was placed on the prediction scheme in terms of selecting particular flow structures. In other words, there was no weighting imposed to emphasize particular frequency bands, so that large scale motion was given as much importance as the smallest scales. Considering the greater contribution to turbulence production and high-energy events attributed to large scale (low frequency), coherent structures, it would seem that preferential weighting imposed on these scales would be beneficial, not only in terms of the predictability of the flow but more importantly, in terms of its controllability. The conditioned spectral analysis may be thought of as providing the appropriate weighting for this purpose. Using this technique, the frequency band associated with coherent structures is isolated and when represented as a filter can be used to emphasize the appropriate scales in the raw signals from the detection sensors.

Figures 4.5 and 4.6 represent configurations with filters incorporated to emphasize the

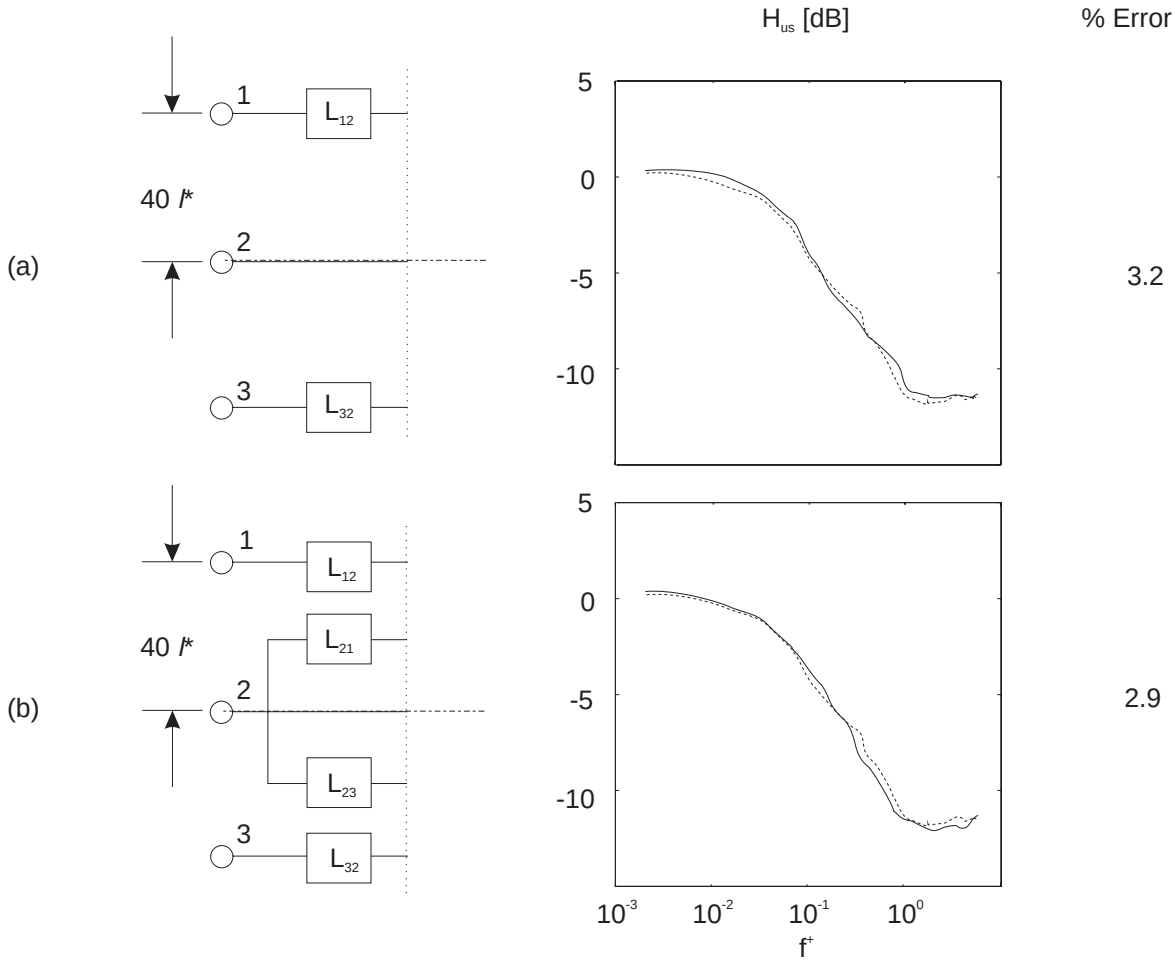

Figure 4.6: Cross-spectra between upstream detection sensors and the streamwise velocity $300l^*$ downstream; (a) three sensors centered about the downstream measurement point with the outer most signals filtered to emphasize the coherent motion, (b) three sensors centered about the downstream measurement point and all filtered to emphasize the large scale motion.

coherent scales. Each FIR filter, L_{ij}, has 32 poles and is constructed from the cross-spectra between adjacent sensors. An example of the filter, L_{21}, was defined in Equation 2.38 and a plot of its magnitude is provided in Figure 2.5). The resulting filtered signals are used as inputs into the predictor, so that the part of the raw signals associated with the coherent structures is used for the prediction of u downstream. The configuration in Figure 4.5a uses a filtered signal from the middle sensor alone to estimate the signals from all three sensors. This is done by combining the signal from the middle sensor with the filters L_{21} and L_{23} which correspond to the part of the adjacent sensor signals that are correlated with the middle sensor signal. The prediction error for this configuration is 2.9% and corresponds to the lowest value obtained. The effect of the filters can be readily observed from the plots of the cross-spectra. The low frequencies are more accurately reproduced than in the unfiltered cases shown in Figures 4.3 and 4.4. This improvement is attributed to the preferential weighting of these lower frequencies imposed by the conditioned analysis. The configuration in Figure 4.5b is a filtered version of that in Figure 4.4a and produces a much lower prediction error of 5.2% compared to the unfiltered case. This is as expected since the spanwise coherence is associated with the coherent structures which are emphasized by the filtering. The configuration in Figure 4.6a includes the unfiltered middle signal and produces a lower error of 3.8%, but one that is higher than the single filtered configuration shown in Figure 4.5a. This indicates that the middle sensor (or that which is in-line with the downstream variable) is the primary contributor to the prediction of the u. Thus an attempt to combine all sensors to produce an optimal configuration is shown in Figure 4.6b. It combines the highly effective prediction of the middle sensor with the filtered signals of the adjacent sensors to extract the most coherent parts from all signals. The prediction error of 2.9% is identical to that with just the middle sensor. This seems to suggest the addition of adjacent sensors will have no effect on the prediction of u. However, on closer examination of the cross-spectra, the lower frequencies is seen to be more accurately predicted, so that although the overall error is unchanged (over the entire frequency range), the improved prediction of the larger scales may improve controllability of the flow.

These results support the idea that the function of the filters that result from the conditioned spectral analysis is to weight different frequency bands. In this case, the large scale structures are associated with the low frequencies which are clearly emphasized by these filters (for example by L_{12} in Figure 2.5). When multiple sensors are used in real-time, these filters also weight the signals from each sensor, relative to each other.

The phase diagrams, which were not shown in the figures, exhibited a constant slope (always true for a FIR filter), which corresponded to a lag that matched the average convection speed of the large scale structures ($u_c^+ = 10.7$, where the convection speed u_c has been normalized by the friction velocity, u_τ). This lag was seen to be constant for all cross-spectra between the upstream and downstream sensors.

4.2.3 Optimal Linear Prediction: Time Description

A qualitative assessment of the effectiveness of the predictor may be provided by the real-time record of the measured and predicted variable. Figure 4.7 shows a short time series of the in-line detection sensor signal, the measured and predicted downstream velocity and

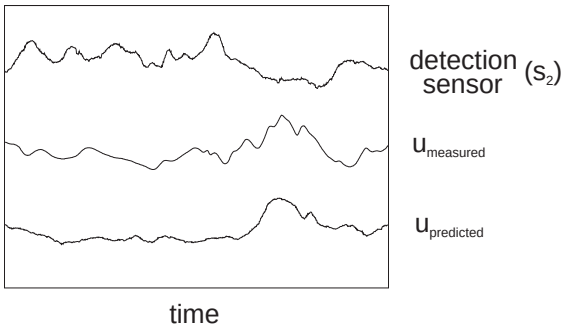

Figure 4.7: Time series showing the middle detection sensor signal, the measured and predicted streamwise velocity ($300l^*$ downstream of the actuator) and the input signal to the actuator. The signals were recorded with the actuator disconnected.

the input signal to the actuator (the actuator was disconnected). Comparing the measured and predicted velocity signals, it is clear that the large scale motion and high amplitude peaks are successfully captured. Furthermore, regions of low and high activity are also well predicted.

It should be noted that although the output of the predictor takes both positive and negative values, the actuator does not differentiate between positive and negative inputs since it only blows out into the boundary layer. Thus, there is a rectification of the input to the actuator in terms of its output flow.

4.2.4 Optimal Linear Prediction: Wall Pressure Versus Streamwise Velocity Fluctuations

The optimal configuration for the prediction of the streamwise velocity fluctuation was used for the prediction of the wall pressure fluctuation $500l^*$ downstream of the detection sensors. Using the configuration based on three sensors (illustrated in Figure 4.6b), the transfer functions between the conditioned sensor signals and the downstream wall pressure were computed and approximated by 32-pole FIR filters.

The characteristics of the filters are illustrated in Figure 4.8. The optimal transfer functions for the streamwise velocity is shown in Figure 4.8a. The emphasis is on the low frequencies ranging up to the inertial scales. The filters for the wall pressure are shown in Figure 4.8b and tend to emphasize higher frequencies indicating the pressure (the output) is a function of the derivative of the upstream sensor signals (the inputs). The low-frequency slope is approximately equal to 1 which corresponds to a first derivative in the time domain ($\partial/\partial t = i\omega$, where $i = \sqrt{-1}$).

This observation in the difference in velocity and pressure characteristics is encouraging when compared to the conditionally sampled results of Johansson *et al.* [9], who show that the high amplitude pressure peaks coincide with large positive gradients in the streamwise velocity fluctuations (discussed further in the introduction).

The accuracy of predicting the downstream pressure compared to the the streamwise

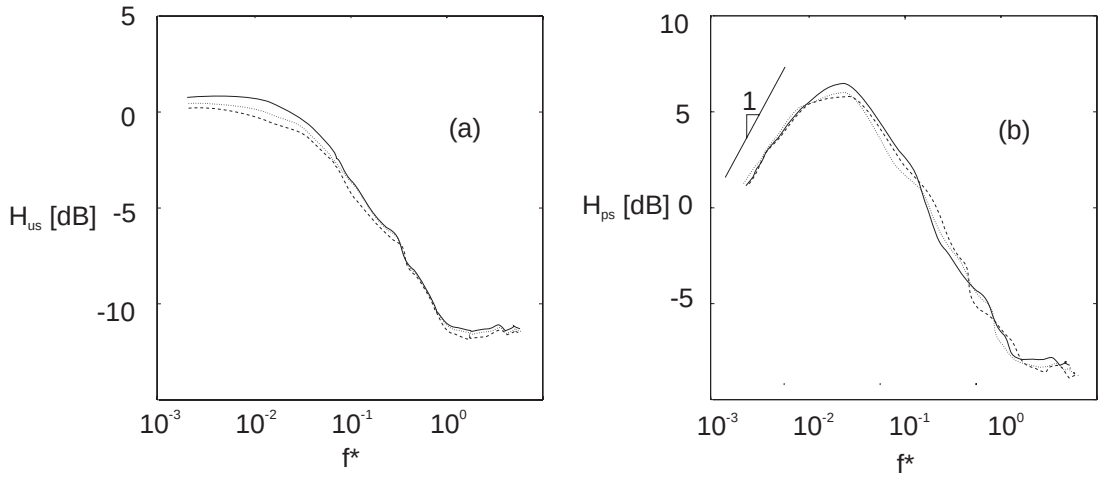

Figure 4.8: Optimal multiple-input/single-output transfer functions for the three detection sensors for the prediction of (a) streamwise velocity $300l^*$ downstream at $y^+ = 10$ and (b) wall pressure $500l^*$ downstream.

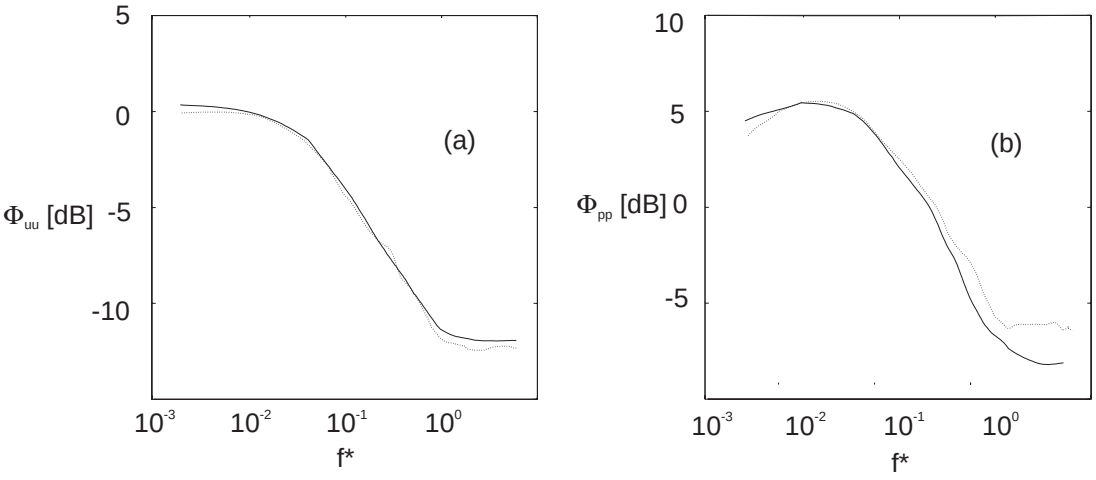

Figure 4.9: Spectra of the measured and predicted streamwise velocity, $500l^*$ downstream of the detection sensors and at $y^+ = 10$, (a), and wall pressure, $500l^*$ downstream, (b). The solid and dotted lines represents the prediction and measurement, respectively.

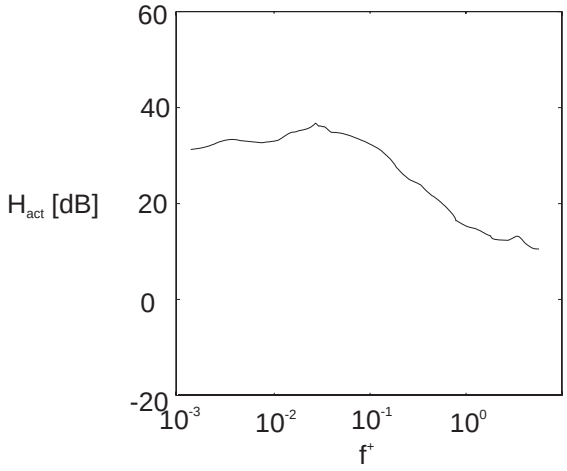

Figure 4.10: Actuator transfer function between the input voltage and the streamwise velocity fluctuation, $300l^*$ downstream.

velocity is illustrated in Figure 4.9. The prediction of the streamwise velocity and the wall pressure fluctuations at $500l^*$ downstream of the actuators were made with a maximum root-mean-squared error of 4.5% and 7.1%, respectively. The cause of the higher errors in pressure is primarily due to the fact that pressure is not as localized in terms of its association with the coherent structures [32]. The intergral expression for the pressure at the wall is given by:

$$\nabla^2 p = 2\frac{\partial U_i}{\partial x_j}\frac{\partial u_j}{\partial x_i} + \frac{\partial^2(u_i u_j - \overline{u_i u_j})}{\partial x_i \partial x_j}. \tag{4.1}$$

Equation 4.1 indicates that the pressure is coupled to the velocity throughout the boundary layer. Nevertheless, the errors are relatively small and are concentrated mainly in the high frequencies, beyond that which is associated with the turbulent coherent motion.

4.2.5 Actuator Transfer Function and Inversion

Figure 4.10 is a plot of the actuator transfer functions. It describes the linear relationship between the input voltage to the actuator and the measured streamwise velocity $300l^*$ downstream. It clearly indicates that there is a particular frequency band within which the flow is most receptive.

These transfer functions were used to determine the appropriate actuator inputs from the predicted velocity at the downstream control points. This called for an inversion of the transfer functions (so that it estimated a voltage output given a velocity input) which then led to phase leads that were absorbed by the longer phase lag associated with the predictor. The causality of the transfer functions were maintained by the inversion, since the spectral estimates were limited to a maximum non-dimensional frequency of $f^+ = 2$ so that the high frequency gain was neglected.

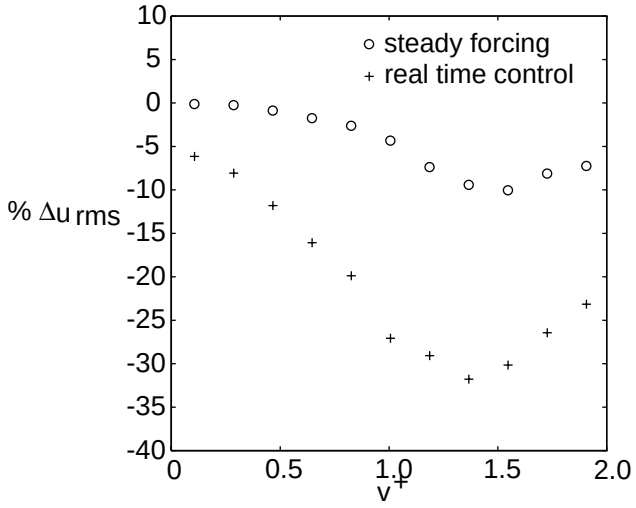

Figure 4.11: Flow response to varying forcing amplitude. Maximum reduction in streamwise velocity fluctuation is obtained with an approximate exit velocity fluctuation of $1.3u_\tau$. Steady and real-time forcing applied with the same power.

4.3 Control Performance

4.3.1 Adaptation

The effect of the control performance with respect to changing control inputs provides insight into the capability of the control system to adapt to changing flow conditions.

In an effort to optimize the performance of the controller, its effect on the flow as a function of forcing amplitude is considered. The controller is first optimized at the actuator position and its output is then multiplied by a factor to vary the total amplitude. Figure 4.11 shows the variation with the control amplitude and indicates an optimal fluctuating exit velocity of approximately $0.6u_\tau$ (where u_τ is the friction velocity at the actuator location), above which the control input overwhelms the flow. This value was observed to be slightly higher than that given by the optimal predictor ($0.45u_\tau$). Note that steady forcing exhibits a similar behavior to the real time control scheme, but is much less pronounced. A maximum reduction of 31% in the streamwise velocity fluctuations is achieved at the optimal forcing amplitude.

The delay associated with the controller represents the average convection time of the large scale motion between the detection sensors and the actuator. This appears as a delay in the prediction filters and is determined by the cross-spectra between the upstream and downstream sensors. Figure 4.12 illustrates the effect of manually changing this delay on the control. The sharp dip centered around the optimal value indicates that this is a sensitive parameter.

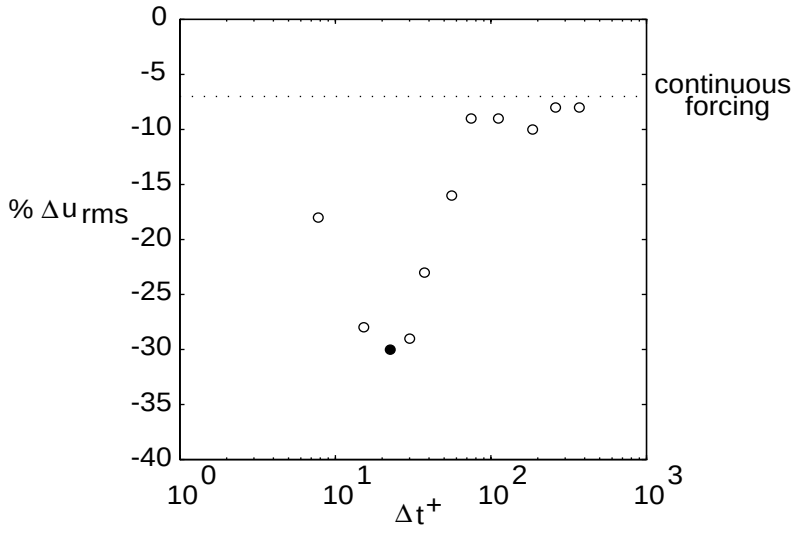

Figure 4.12: Flow response to varying control delay. Optimal delay is represented by the filled circle and is computed in the optimization process. Steady and real-time forcing applied with the same power.

4.4 Single-Input/Single-Output Control

Single-output control was implemented with the schemes shown in Figure 4.5a and Figure 4.6b. In the former scheme, only one sensor is used to detect on-coming structures. The filtering of this single signal emphasizes the important large scale structures in the flow and enables the accurate prediction of the control variable downstream.

Figure 4.13 shows the reduction in u_{rms} (normalized by the unforced u_{rms}) as a function of x^+, measured from the center of the actuator ($x^+ = 0$). It illustrates the extent of the control in the streamwise direction directly downstream of the actuator slit. The solid circles and bold pluses indicate the position at which the controller was optimized ($x^+ = 12$ and 20). The maximum reduction in streamwise velocity fluctuations is seen to extend over most of the slit. The effect persists for several hundred viscous length scales downstream before gradually returning to the unforced value. There is no noticeable effect with optimizing at the different locations.

Figure 4.14 shows similar profiles in the wall-normal direction at $x^+ = 20$ and $z^+ = 0$. The maximum reduction in u_{rms} is greater closer to the wall, rising from 18% when optimized at $y^+ = 15$ to 26% when optimized at $y^+ = 10$. The recovery to the unforced level was however more rapid when optimized closer to the wall. The control effect persists for approximately $50l^*$ from the wall.

This result may indicate that better control can be achieved with wall quantities such as pressure and shear stress. Note, however, that wall pressure is not an appropriate choice in localized control schemes in general, since it is governed by the velocity fluctuations throughout the flow field. This is illustrated by the relationship between the pressure and

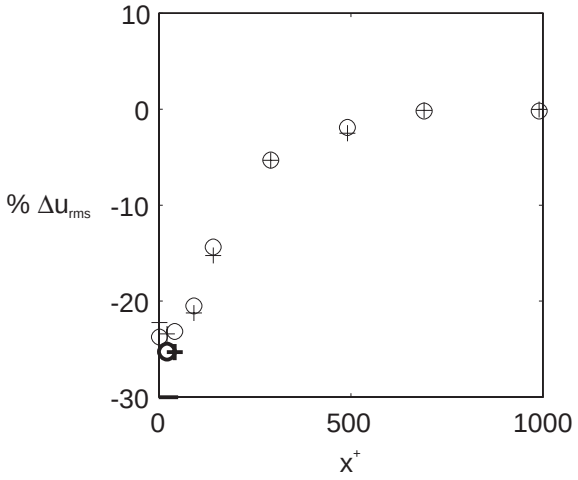

Figure 4.13: Percentage change of the streamwise velocity fluctuation with streamwise distance from the middle of the actuator for two locations of control optimization ($x^+ = 12$ and $x^+ = 20$). Filled circle and bold pluses indicate point of optimization. Bold line on the abscissa represents the downstream half of the actuator slit.

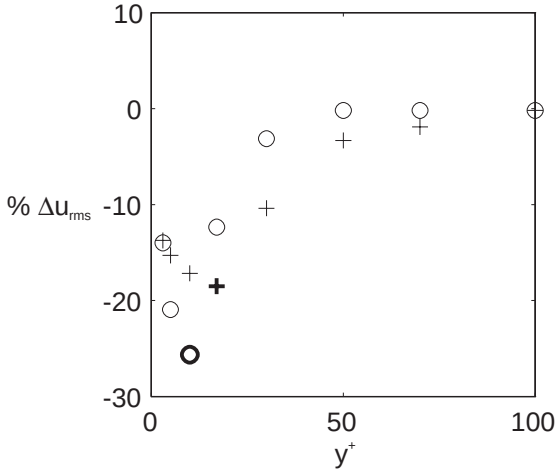

Figure 4.14: Percentage change of the streamwise velocity fluctuation with normal distance from the wall for two locations of control optimization ($y^+ = 10$ and $y^+ = 15$). Filled circle and bold pluses indicate point of optimization.

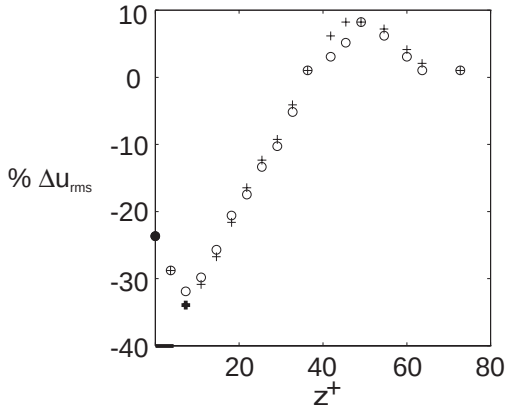

Figure 4.15: Percentage change of the streamwise velocity fluctuation with spanwise distance from the actuator for two locations of control optimization (circles for $z^+ = 0$ and pluses for $z^+ = 5$). Filled circle and bold pluses indicate points of optimization. The measurements were take at $x^+ = 0$ and $y^+ = 15$. Bold line on the abscissa represents the extent of the actuator slit.

the velocity field, given by Equation 4.1.

Figure 4.15 is the plot of the reduction in u_{rms} with z^+. It indicates that a maximum reduction of 34% occurs on either sides of the slit, approximately at the location of the streamwise vortices created by the forcing. Optimizing at this location ($z^+ = 7$) shows very little change in the overall effect. The profile indicates a small region of increased intensity before recovery to the unforced level further out in the spanwise direction. This increase is, however, small compared to the reduction found in the rest of the profile.

Figure 4.16 is a plot of the spectra of the streamwise velocity measured at $x^+ = 20$, $y^+ = 12$ and $z^+ = 0$ for three different flow conditions, namely (i) the uncontrolled flow , (ii) with continuous forcing at the actuator resonant frequency (2.3kHz) and (iii) with real-time active control. It illustrates the effectiveness of the active control scheme at suppressing the large scale, low-frequency motion. Note that the resonant frequency of the actuator, represented by the sharp peaks, was far higher than the frequencies associated with the flow dynamics. This was essential to enable the bandwidth of the controller to span the frequency range over which the flow was receptive.

4.5 Multiple-Input/Single-Output

Although there is no apparent improvement in the prediction of the downstream control variable (comparing Figures 4.3a and 4.4b), including all three detection sensors in the control scheme (Figure 4.4b) may have implications in regards to the control performance. This multiple-input/single-output result is discussed below.

Figure 4.17 shows the reduction in u_{rms} with streamwise distance compared to the single-sensor case. The measurements were taken at a height of $y^+ = 12$ and at $z^+ = 0$. It shows that there is a negligible difference between the two. Similarly in Figure 4.18 which illustrates the variation with the wall-normal distance. The spanwise variation, however, indicates an

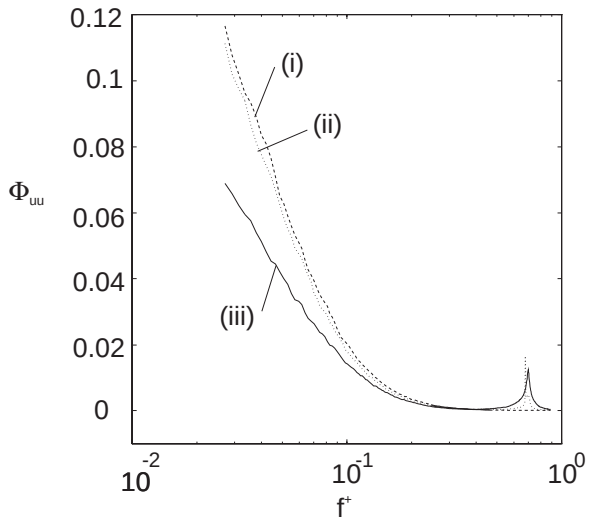

Figure 4.16: Spectra of the streamwise velocity measured at $x^+ = 20$, $y^+ = 12$ and $z^+ = 0$ for, (i) uncontrolled flow , (ii) continuous forcing at the actuator resonant frequency (2.3kHz) and (iii) real-time active control. Note that the forcing frequency is represented by the sharp peak embedded in the high-frequency regime.

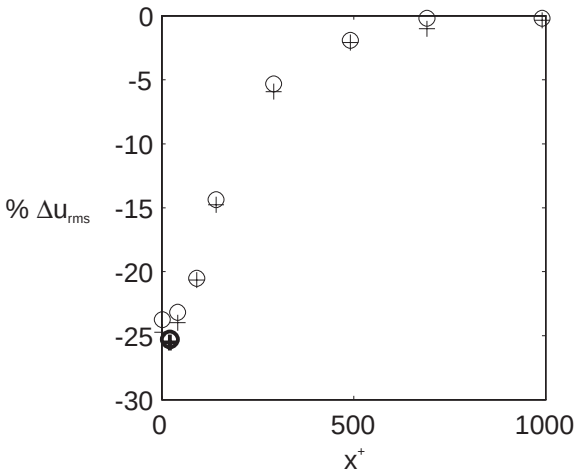

Figure 4.17: Percentage change of the streamwise velocity fluctuation with streamwise distance from the center of the actuator array. The circle represents the single-sensor result and the pluses represents the multiple sensor result. The bold circle and plus indicate the point of optimization ($x^+ = 20$).

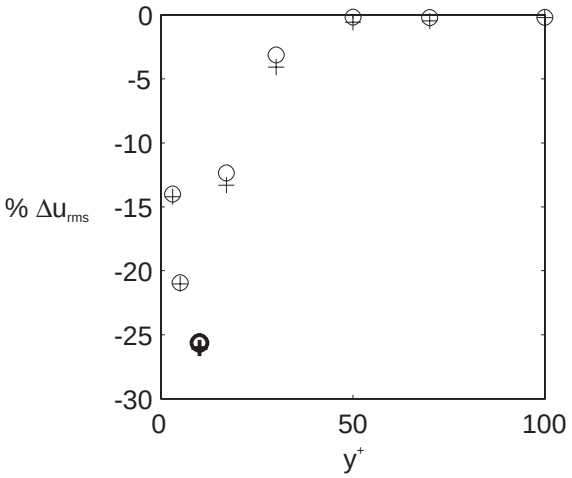

Figure 4.18: Percentage change of the streamwise velocity fluctuation with normal distance from the wall. The circle represents the single-sensor result and the pluses represents the multiple sensor result. The bold circle and plus indicate the point of optimization ($y^+ = 15$).

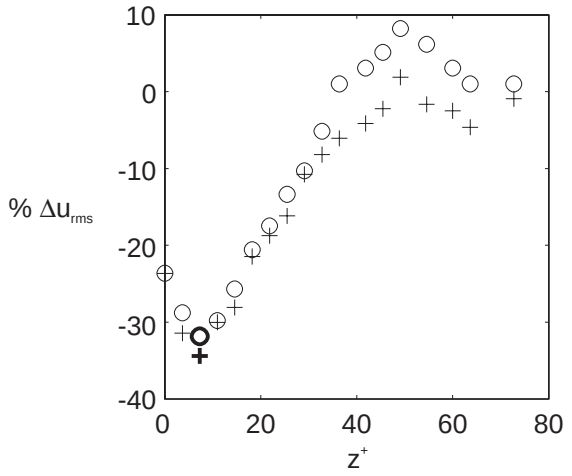

Figure 4.19: Percentage change of the streamwise velocity fluctuation with spanwise distance from the center actuator. The circle represents the single-sensor result and the pluses represents the multiple sensor result. The bold circle and plus indicates the point of optimization ($z^+ = 5$).

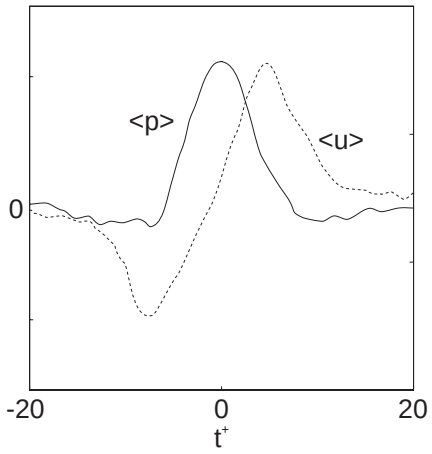

Figure 4.20: Conditional averages of the wall pressure and streamwise velocity fluctuation at $y^+ = 12$ with a threshold level of 1 and an averaging time of $20t^*$. Note that the curve shown for pressure is based on the raw voltage output of the microphone and is linearly related to the true value of the wall pressure.

improvement both in terms of greater reduction at the optimized spanwise location (an increase of 6% from 33% to 35%) and a recovery to the unforced case without significant overshoot (i.e. an increase in u_{rms}). The recovery occurs within the same spanwise extent but the lack of a u_{rms} region suggests a superior control performance compared to the single-sensor case.

4.6 VITA Results

The VITA technique (expressed in Equation 1.1) was used to compute bursting frequencies at different threshold values. The averaging time was chosen to be $20t^*$. This was based on results by Alfredsson and Johansson [4] who demonstrated that errors in bursting frequency were minimized for averaging times of the order of the outer scales. In these experiments, the outer time scales computed using the freestream velocity and the local displacement thickness of the boundary layer was equal to $18.5t^*$.

The conditional averages of the wall pressure and velocity events, with a threshold level of 1, are shown in Figure 4.20. It compares well with the results of Johansson *et al.* [19] and clearly shows that a high positive shear region (accelerating streamwise velocity) is associated with a pressure peak at the wall. This has interesting consequences regarding the control of the boundary layer flow, since it suggests that a similar control algorithm may be used for both wall pressure and shear.

Figure 4.21 is a plot of the bursting frequency normalized by t^* for different threshold levels. With a threshold level of 3, the frequency is approximately 0.01, corresponding to a time between bursts of $100t^*$. This agrees well with the results of Blackwelder and Haritonidis [2].

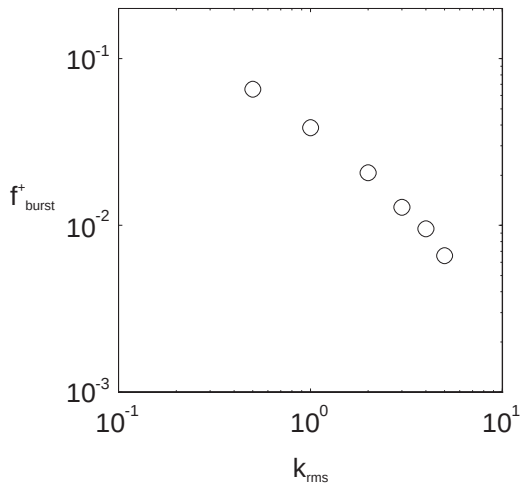

Figure 4.21: Plot of the bursting frequency normalized by t^* versus threshold level at $y^+ = 12$. Averaging time was $20t^*$.

4.6.1 Effects of Active Control

A comparison was made between the bursting frequency in the controlled and uncontrolled boundary layer to evaluate the effect of control on the large scale structures. Figures 4.22a and 4.22b illustrate the reduction in burst frequency with threshold level at two streamwise locations. The burst frequency is seen to decrease by up to 23% at the higher threshold levels at the optimized location (Figure 4.22a). However, this reduction is localized and the flow is seen to return to close to the unforced case $20l^*$ downstream (Figure 4.22b). This recovery to the unforced case is more clearly seen in Figure 4.23a which shows the reduction in burst frequency calculated with a threshold level of 3, versus downstream distance. The discrepancy in the reduction of the bursting frequency and u_{rms} suggests that the modification of the coherent structures takes place on a much smaller time scale compared to that associated with its effect on u_{rms}.

To illustrate this further, the bursting frequency is computed with a threshold level that is based on the unforced u_{rms}. This provides an indication of how the bursting frequency of events of a fixed amplitude (i.e. 3 times the unforced u_{rms}) are affected by the control. Figure 4.23b shows the reduction of the bursting frequency with x^+, computed with the unforced threshold level, plotted together with the reduction in u_{rms}. The plots show that apart from the first point, there is a similar variation with x^+ for both variables. This indicates that at the optimal control point (marked in bold), the flow undergoes an aggressive modification accompanied by a sharp fall in bursting frequency (suggesting a reduction in turbulence producing events). As this modified flow convects downstream, it resembles a weakened flow field in which both u_{rms} and f^+_{burst} have been reduced and recover at similar rates up to their unforced levels several $100l^*$ downstream. Thus the effect of a short impulse that modifies the flow locally is seen to persist far downstream suggesting two time scales; (i) one that is associated with the modification and (ii) one that is associated with the life of the modified flow structures. The former is observed to be an order of magnitude shorter than the latter. This results supports the suggestion of the existence of two time scales by

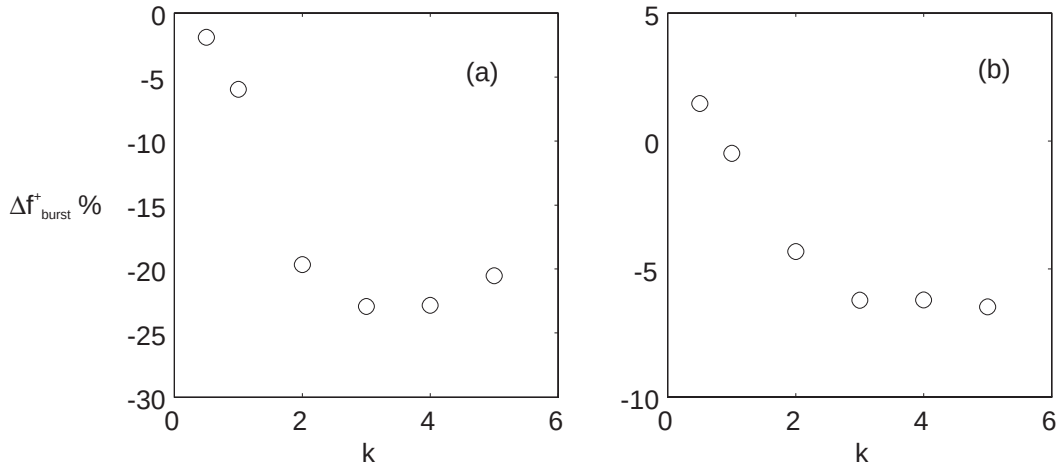

Figure 4.22: Percentage change in bursting frequency for varying threshold levels measured at (a) the optimal streamwise location ($x^+ = 20$) and (b) at $x^+ = 40$. The corresponding reduction in u_{rms} at these stations are 24% and 23.2%. Threshold levels are based on the local u_{rms}.

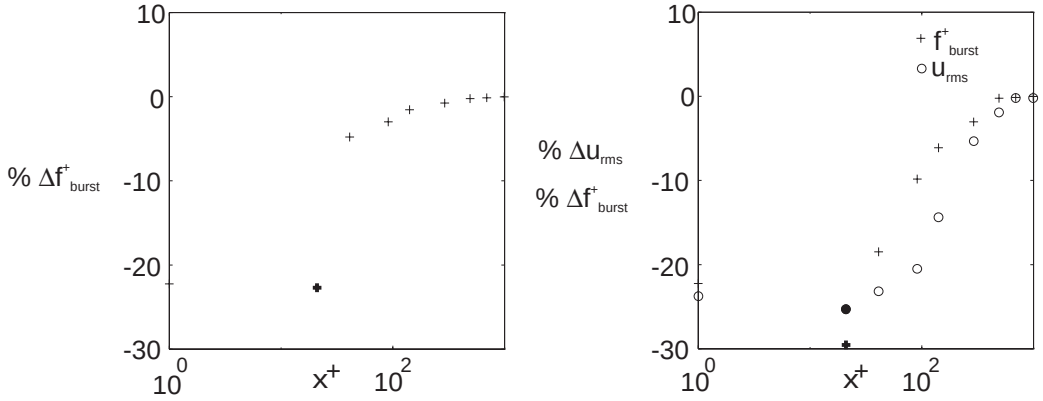

Figure 4.23: Percentage reduction in bursting frequency with streamwise distance from the center of the actuator (a) using a threshold level of 3 times the local u_{rms} and (b) a threshold level of 3 times the unforced u_{rms}.

.

Landahl [10].

4.6.2 Wall Pressure Control

The control of the wall pressure fluctuation is carried out in a similar fashion to that of the streamwise velocity fluctuation.

Single-Input/Single-Output

The single-input/single-output configuration is illustrated in Figure 4.5a. In this case, the conditioned pressure signal (described in Section 3.2.3), $500l^*$ downstream of the detection sensors, is used as the control variable and a reduction of 17% in p_{rms} is obtained.

Multiple-Input/Single-Output

The multiple-input/single-output configuration is illustrated in Figure 4.6b. The additional information obtained from the adjacent sensors improved the controllability of the flow (as in the case with the streamwise velocity fluctuations), and p_{rms} was reduced by 20%.

4.7 Multiple-Input/Multiple-Output control

The introduction of multiple actuators may be seen to serve two purposes; (i) to improve the control at a single location and (ii) to expand the spatial extent of control. To explore these effects further, a spanwise array of three actuators is incorporated into the control scheme to minimize the streamwise velocity fluctuations at three downstream locations, $300l^*$ downstream of the actuators and $40z^+$ apart (i.e. in-line with each actuator). The multiple-input multiple-output prediction procedure was used together with the pre-conditioning of all three detection sensors to emphasize the large scale motion (as in Figure 4.4b). To verify the effectiveness of predicting the downstream variable, the predicted value of u_{rms} is compared to the measured value and is shown to fall within an error margin of 4.5%.

In order to assess the effect of introducing multiple actuators on the control performance at a single downstream location, the multiple-input/ multiple-output prediction is carried out with preferential weighting for that particular location (in this case, the center location was chosen, which was also used in the single output case). That is, the signal from that location is emphasized by weighting the signals from the other control points by a small value (chosen to be 1% of the primary signal). This is done when computing the optimal prediction filters. The aim is then to use all three actuators to minimize u_{rms} at the primary location.

Figures 4.24, 4.25 and 4.26 show the streamwise, wall-normal and spanwise extent of the multiple actuator controller downstream of the primary control location compared to the single-actuator case. The streamwise control is improved in that local reduction in u_{rms} is greater (Figure 4.24) at a given downstream location. Thus the use of multiple actuators in

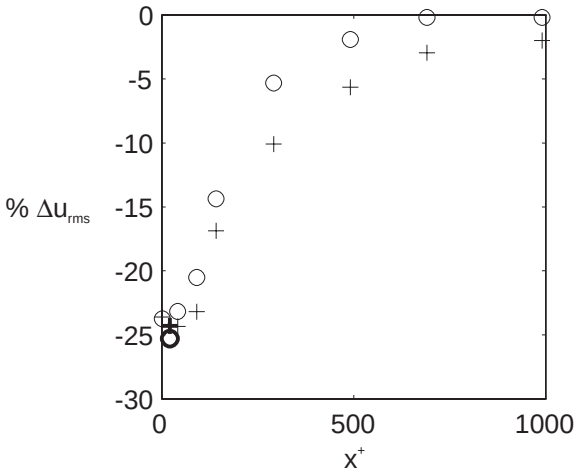

Figure 4.24: Percentage change of the streamwise velocity fluctuation with spanwise distance from the center actuator. The circle represents the single-sensor result and the pluses represents the multiple actuator result. The control is weighted to favor a single control point, $300l^*$ downstream of the center of the actuator array. The bold circle and plus indicates the point of optimization ($x^+ = 20$).

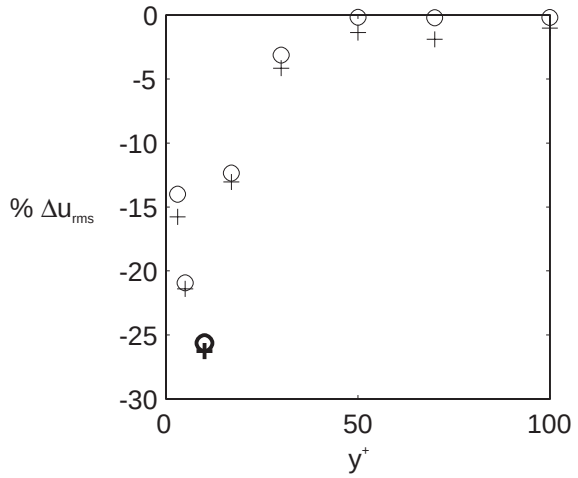

Figure 4.25: Percentage change of the streamwise velocity fluctuation with streamwise distance from the center of the actuator array. The circle represents the single-sensor result and the pluses represents the multiple actuator result. The control is weighted to favor a single control point, $300l^*$ downstream of the center of the actuator array. The bold circle and plus indicate the point of optimization ($y^+ = 15$).

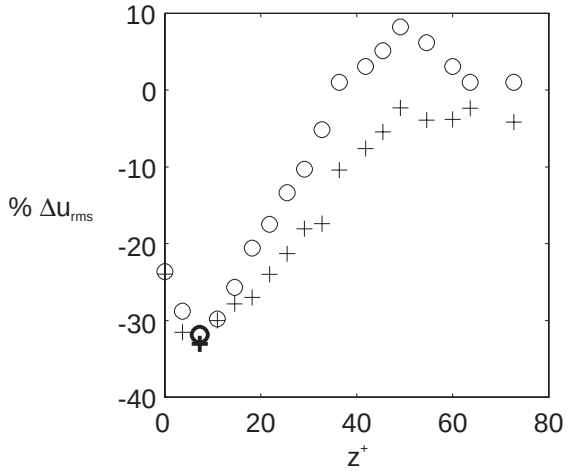

Figure 4.26: Percentage change of the streamwise velocity fluctuation with normal distance from the wall. The circle represents the single-sensor result and the pluses represents the multiple actuator result. The control is weighted to favor a single control point, $300l^*$ downstream of the center of the actuator array. The bold circle and plus indicate the point of optimization ($z^+ = 5$).

the spanwise direction has a definite effect on the streamwise extent of the control, suggesting that the introduction of streamwise vortices adjacent to the in-line actuator contributes to the persistence of the modification to the flow structure characteristics. Note that the maximum reduction of u_{rms} at the optimized location is slightly lower (by approximately 4%) so that the effect of the adjacent actuators is not an immediate reduction in u_{rms} and is realized only as the flow structures convect downstream. This suggests that an initial modification of the large scale motion by a single actuator may be sustained with actuators placed downstream preserving the modified flow structure as it convects downstream. The downstream separation of adjacent actuators would be determined from the streamwise extent of the maximum control region, centered about the optimal design point. From Figure 4.24, this is estimated to be in the order of $100x^+$.

The addition of multiple actuators is not 'felt' in the wall normal direction (Figure 4.25) suggesting that the control is effective only in the near wall region ($y^+ < 50$) which is as expected since the streamwise vortices created by the actuators do not penetrate beyond this wall region and moreover, the majority of the coherent structures are known to be located within this wall region.

The effect of multiple actuators on the spanwise distribution is more pronounced (Figure 4.26). The recovery of u_{rms} to the unforced level is more gradual and does not exhibit the overshoot and the increase in u_{rms} observed with the single-actuator control. The extent of control in the spanwise direction is similar to that of the single-actuator case but the total reduction integrated over the spanwise extent is approximately doubled. As in the streamwise profile, the maximum reduction remains unchanged from the single-actuator case, but the added control provided by the adjacent actuators extends the spanwise control area. This indicates that additional actuators placed in the array may be used to expand the control region further in the spanwise direction. The appropriate spanwise separation

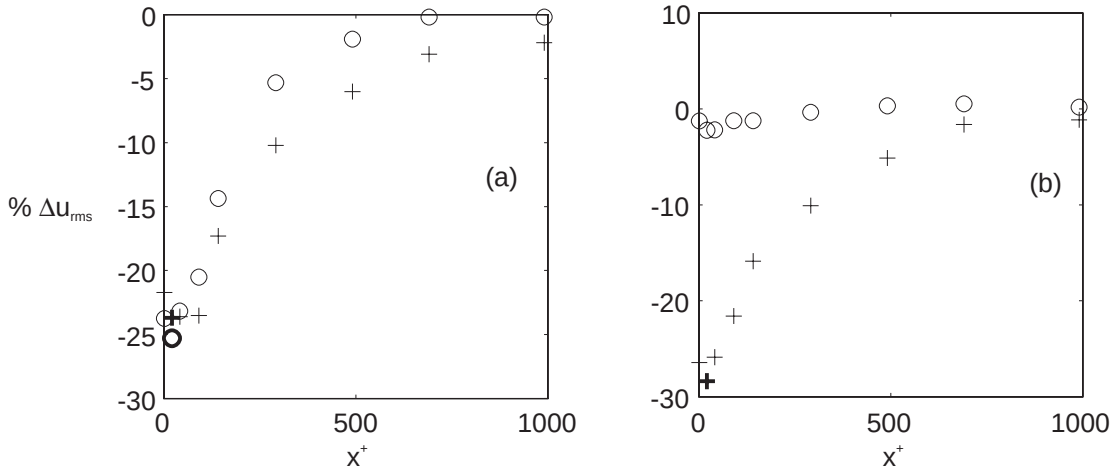

Figure 4.27: Percentage change of the streamwise velocity fluctuation with streamwise distance from (a) the center of the actuator array and (b) downstream of an adjacent actuator compared to the single actuator case. The circles represent the single-sensor result and the pluses represents the multiple actuator result. The bold circle and plus indicate the point of optimization ($x^+ = 20$).

may be estimated from the extent of the single point control and is approximately $40z^+$.

The full potential of the array of three actuators was examined by weighting all three control points equally. The aim here was to obtain the widest possible control region while maintaining the optimal control configuration. The control scheme was implemented similarly to those described in the previous configuration.

Figures 4.27, 4.28 and 4.29 show the streamwise, wall-normal and spanwise extent of the multiple actuator controller compared to the single-actuator case.

Figure 4.27a shows the streamwise control is increased as in the case above. However the maximum reduction is now 22% as opposed to 25% in the single sensor case. This fall in control performance downstream of the middle actuator is attributed to the fact that the actuators are being used to control the flow at three separate locations and their ability to effectively control the flow at each will be degraded to compensate for the broader control field. This extended region of control is clearly observed in Figure 4.27b, which shows the streamwise reduction in u_{rms}, downstream of an adjacent actuator compared to the single control point case. As expected, the control region extends much further downstream confirming the influence of the addition control points.

The wall-normal variation shows a slight improvement - no more than a further reduction of 4% compared to the single actuator case (Figure 4.28a). Thus with multiple actuators, the control remains isolated in the near-wall region. As mentioned above, this is as expected due to the proximity of the coherent structures to the wall region. Figure 4.28b shows the reduction of u_{rms} in the wall-normal direction downstream of an adjacent actuator. It illustrates the extension of the controlled flow far beyond that for the single control point case. This provides further encouragement for controlling a larger region with additional actuators and control points.

The spanwise variation again shows the most pronounced changes. Figure 4.29 shows the

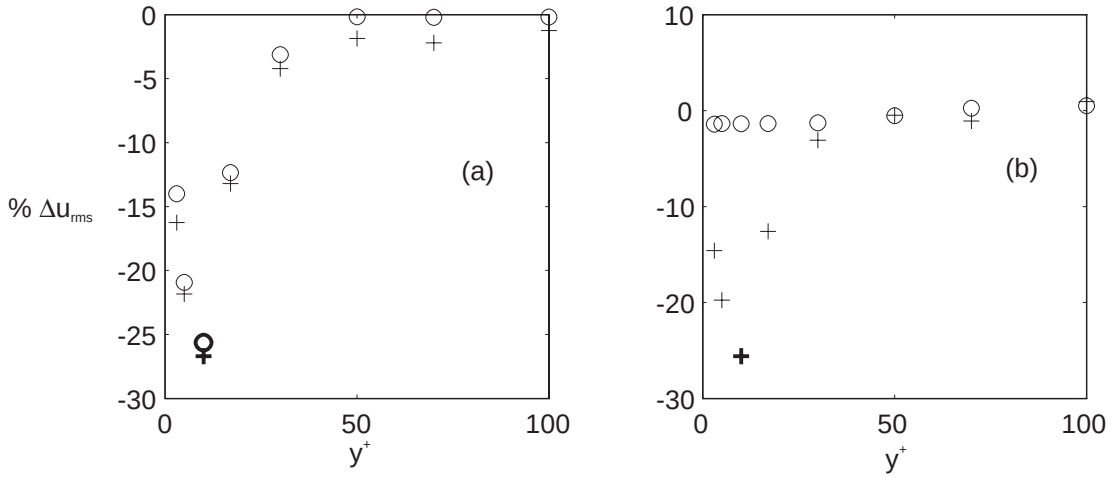

Figure 4.28: Percentage change of the streamwise velocity fluctuation with normal distance from the wall at (a) the center of the actuator array and (b) at an adjacent actuator compared to the single actuator case. The circles represent the single-sensor result and the pluses represents the multiple actuator result. The bold circle and pluses indicate the point of optimization ($y^+ = 15$).

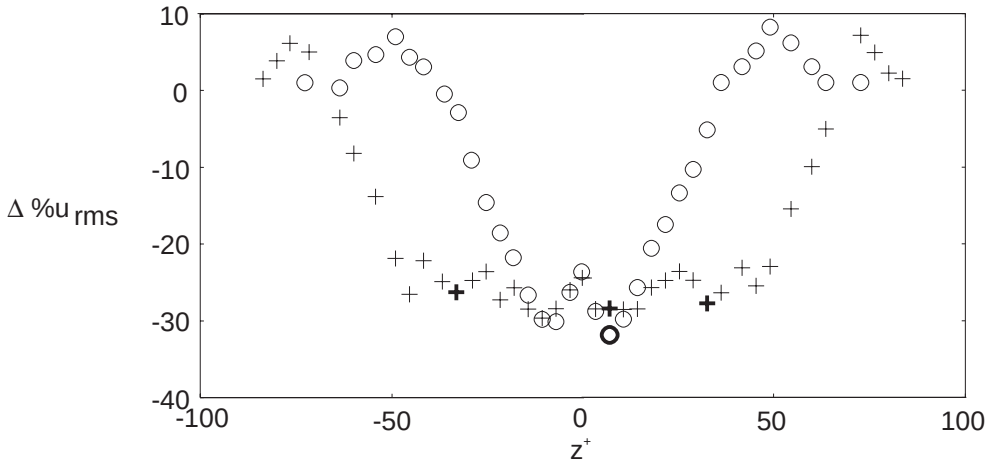

Figure 4.29: Percentage change of the streamwise velocity fluctuation with spanwise distance the optimal location ($x^+ = 20$) compared to the single actuator case (the circle represents the single actuator result and the pluses represents the multiple actuator result). The bold pluses and circle indicate the points of optimization ($z^+ = 5$ and $z^+ = 45$).

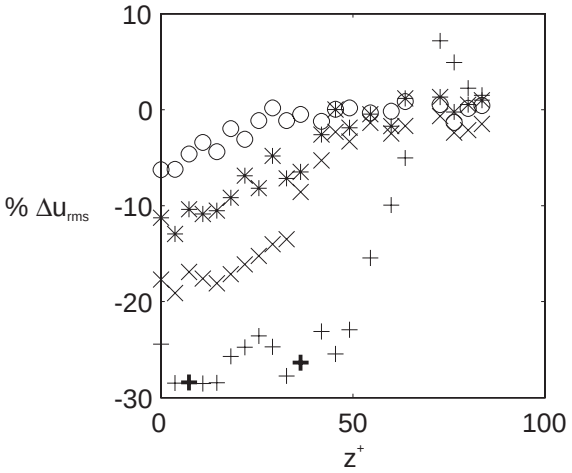

Figure 4.30: Percentage change of the streamwise velocity fluctuation with spanwise distance from the center actuator at four streamwise stations downstream of the actuator array; $x^+ = 20, 100, 300$ and 500. The bold pluses indicate the points of optimization ($z^+ = 5$, $z^+ = 45$).

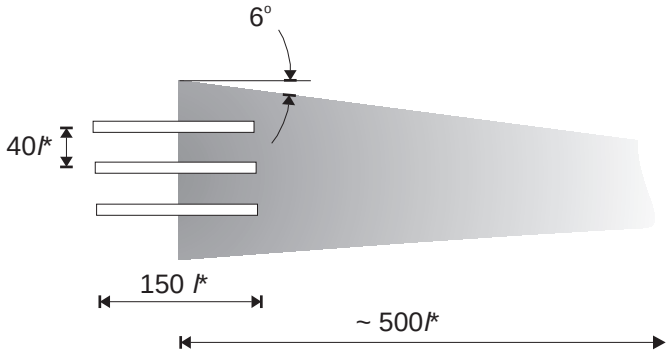

Figure 4.31: Diagram illustrating the zone of influence downstream of the three actuators.

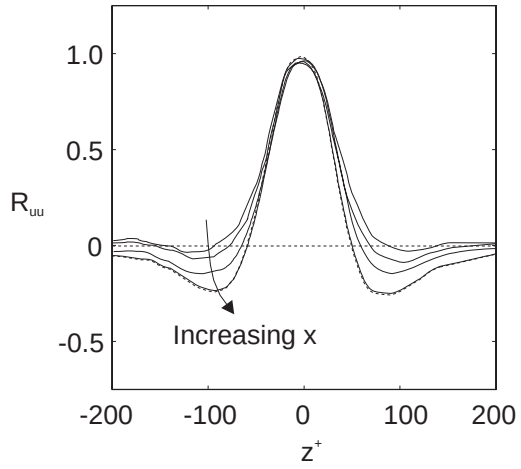

Figure 4.32: Spanwise spatial correlations downstream of the actuator array at $x^+ = 20 : +, 100 : x, 300 : *$ and $500 : o$.

increased control obtained by including multiple actuators as compared to the single actuator case. At the optimal streamwise location ($x^+ = 20$ downstream of the middle actuator), the region of maximum reduction in u_{rms} spans a range of $100z^+$ (corresponding to the array of 3 actuators spanning $80z^+$) with an average value of 26%. As the $y - z$ plane moves further downstream this region shrinks with a converging angle of approximately 6^o (Figure 4.30). Figure 4.31 illustrates the converging pattern in relation to the actuators and control points (drawn to scale). This zone of influence of this particular configuration may be used to determine the appropriate spacing between actuators and control points for broadening the region of control. The extent of control influence in the spanwise direction is approximately $40z^+$ centered about the actuator slit, which implies that the current actuator separation of $40z^+$ is ideally suited to provide maximum control for the minimum number of devices.

The spanwise profile is accompanied by an overshoot region of increased u_{rms} (as in the single-actuator case) which is shifted out-board by $25z^+$ compared to that in the single-actuator case.

The spanwise spatial correlation at four streamwise stations downstream of the actuator array is shown in Figure 4.32. The correlation corresponding to the unforced flow is shown by the dashed line. At the point of optimization ($x^+ = 20$), the location of the minimum point and the point of zero crossing have been forced out further in the spanwise direction. This indicates that the coherent structures that now exist, as a result of the control, are more widely spaced in the spanwise direction. They are also much weaker as indicated by reduced negative correlation at the minimum point. The correlation curve recovers to the unforced curve as the streamwise station moves further downstream. The implication in this modification of the spatial correlation is that the introduction of the streamwise vortices into the flow to 'cancel' coherent structures achieves its desired control result (in this case, a reduction in the streamwise velocity fluctuations) by interacting with the flow in such a way so as to increase the spanwise separation of the large-scale, energy producing structures,while weakening their relative correlation with each other. In other words, the break-up of the coherent structures is achieved by weakening the their ability to interact with each other.

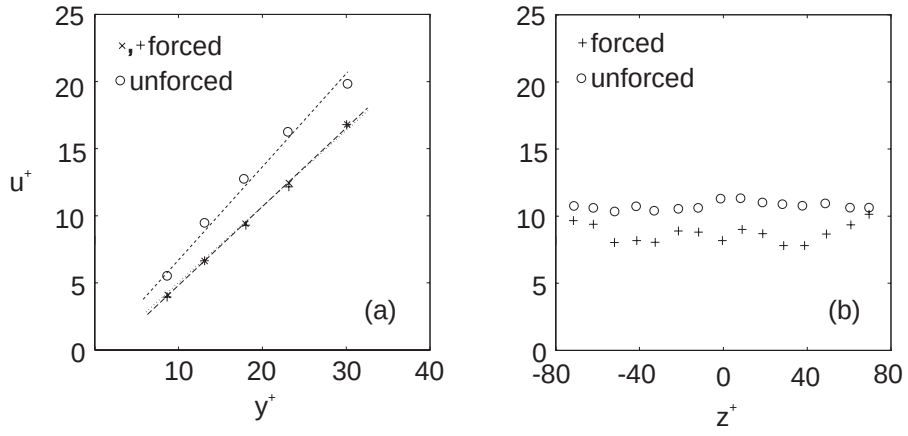

Figure 4.33: Mean velocity profile near the wall for the forced and unforced cases,(a) in the wall-normal direction at $z^+ = 10$, the shear is reduced by approximately 7% in the forced case; (b) in the spanwise direction, at $y^+ \approx 15$, the velocity is reduced throughout the control region.

4.8 Wall Pressure Control

The multiple-input/multiple-output control scheme was applied to the array of three pressure sensors, $500l^*$ downstream of the detection sensors. The performance of the controller in reducing the pressure fluctuations was similar to that for the streamwise velocity, in that the maximum reduction was less than in the single-output case but the control effected a larger area. The reduction in p_{rms} was 15% at the middle sensor and 12% at the adjacent ones, $40l^*$ in the spanwise direction.

4.9 Wall Shear Stress Control

Both Figure 4.20 and Equation 4.1 indicated that there exists a strong relationship between the wall pressure and the wall shear stress. It was thus instructive to investigate the effect of the control on the wall shear stress. This effect was measured by considering the slope of the mean velocity profile near the wall. Figure 4.33a is a plot of the mean velocity profile for the unforced and forced cases taken at $z^+ = 10$. It shows a reduction in the shear by approximately 7%. Although this is only a qualitative measurement of the wall shear, the measurement was taken with the hot-wire fixed at each location while the control was switched on and off. Thus it illustrates a definite and marked reduction and shows promise for future work in drag reduction. Figure 4.33b is a plot of the mean velocity profile in the spanwise direction taken at $y^+ = 15$. It shows that the reduction in the mean velocity extends over the entire spanwise extent of the controlled region, suggesting that the reduction is shear is not localized close to the actuators.

Chapter 5

Conclusions and Further Work

The formulation and implementation of an active control algorithm for a turbulent boundary layer was presented. The control scheme was based around an active matrix of sensors and actuators that were networked through linear filters that optimally predicted the evolution of coherent structures in the near-wall region as well as describing the characteristics of the actuators and their effect on the flow. The control objective was the linear cancellation of a flow parameter at chosen control points, downstream of the actuators.

A formal procedure was developed that provides an efficient, realizable and extendible control algorithm. The limitations of the scheme stems from the ideal assumption of linearity made both in the system identification and the control. Other non-ideal behavior in the system come from the lack of information of the flow field, due to the practical limitations placed on the number of sensors and their capabilities. The sensors used here are sensitive to spanwise shear fluctuations but do not differentiate between positive and negative fluctuations. The acuators were also limited to only *blowing* into the boundary layer. This rectification of the sensors and actuators inhibited the full potential of the control scheme to be realized. Nevertheless, the control results were better than expected in terms of the suppression of the turbulence fluctuations and the spatial extent of the controlled flow.

A summary of the main results and observations is given below.

5.1 System Identification

The system identification of the plant - in this case the turbulent boundary layer - was crucial to the success of the control scheme. The coherent structures in the near-wall region are known to be associated with a major part of the turbulent energy production so that the identification efforts were focused on these large scale structures. Furthermore, the linear dynamics of these flow structures (discussed in the introduction) strengthened the linear control approach taken here.

The identification of these large scale structures was achieved by the use of an array of spanwise shear sensors. These sensors were sensitive to spanwise shear, which was shown to well correlate with the coherent structures [34]. It was shown that the cross-correlation between two sensors separated by $300l^*$ in the streamwise direction increased from 0.1 to 0.4 for streamwise and spanwise shear components, respectively. In order to improve the identi-

fication scheme, the signals from these sensors were processed to emphasize the frequencies associated with the large scale motion (low frequency). This was done with a conditioned spectral analysis approach where the correlated parts of adjacent sensor signals were computed from their cross-spectra. These modified signals were then used to predict downstream flow parameters.

A linear predictor was formulated with an optimal design that solved for input/output transfer functions based on minimizing the root-mean-squared value of a chosen parameter in a least squares sense. Predictors with single and multiple inputs and outputs were designed and implemented to determine their relative accuracy. It was shown that for a single-input/single-output system, the error in predicting the streamwise velocity fluctuation, u_{rms}, $300l^*$ downstream was 2.9% when the pre-conditioning was applied to emphasize the low frequency. When more inputs were added (adjacent sensors in the spanwise direction) the error in the prediction of u_{rms} was unchanged at best. However, on examining the spectra of the measured and predicted streamwise velocity, it was found that the low frequencies were better predicted with multiple inputs, suggesting improved identification of the large scale motion.

A time series of the predicted and measured downstream parameter shows that the large scale motion is very well estimated together with regions of high and low activity.

5.2 Sensors and Actuators

Flush-mounted hot-wire sensors, sensitive to spanwise shear fluctuations were used for the identification of flow structures. As mentioned earlier, their signals were rectified due to their inability to differentiate between positive and negative spanwise shear stress fluctuations. Streamwise velocity and wall pressure were measured with a hot-wire and a surface-mounted microphone.

An array of three resonant actuators was made from a series of closed cavities with an exit slit into the boundary layer flow. The dimensions of the actuator cavity and the slit area were optimized for maximum mass flow. The slit was aligned in the flow direction and the outflow from the actuator comprised of a pair of streamwise vortices accompanied by a steady jet. The actuator output is rectified, in that it only blows into the boundary layer. The maximum jet exit velocity was 1.5 m/s ($5u_\tau$) and was obtained with an input voltage of 180 V. The average resonant frequency of the actuators was 2.3 kHz which corresponded to $0.62f^*$.

5.3 Control Strategy

The control strategy combines the signal from the upstream shear sensors with the conditioning filters (obtained from the conditioned spectral analysis between adjacent sensors) and the predictor. The output of the predictor is an estimate of the downstream parameter that is to be suppressed. Using the transfer function between the actuator output and its effect on the downstream parameter, the input to the actuator is set so that it creates an equal

and opposite perturbation at the downstream location with the aim of linear cancellation of the parameter.

The downstream parameter is measured in the controlled flow and an error signal is sent back to the controller so that periodic adaptation can be made, if required.

5.4 Control Performance

Adaptation of the input amplitude indicates that there is an optimal exit velocity of $1.3u_\tau$ at which the greatest suppression of the downstream parameter is obtained.

The reduction in u_{rms} is seen to extend to approximately $500l^*$ in the streamwise direction, $50l^*$ in the wall-normal direction and $50l^*$ on either sides of the actuator, in the spanwise direction. The maximum reduction of 34% occurs in the streamwise plane corresponding to the control point and at the spanwise and wall-normal location corresponding to the center of the streamwise vortices created by the actuator ($z^+ = 5, y^+ = 12$). When multiple actuators are used, the maximum reduction of u_{rms} is less ($\approx 30\%$) but it extends over a wider region in the spanwise direction, up to the location of the adjacent actuators.

VITA events were detected using the streamwise velocity fluctuations and were shown to be markedly reduced (a maximum reduction of 23% at the control point ($x^* = 12$) with a threshold level of 3), when the control was applied. When the threshold is normalized with the unforced u_{rms}, the recovery of the bursting frequency to the unforced level with streamwise distance is similar to that for u_{rms}, suggesting that the control creates a region downstream of the actuators that resembles a weaker turbulent flow, with reduced u_{rms} and bursting frequency.

The results also indicate that the control effort provides an initial 'kick' to the flow that causes it to respond instantly, before a much slower recovery to the uncontrolled case, as the flow structures convect downstream.

Spatial correlations at several streamwise stations downstream of the actuator showed the effect of control on the physical properties of the large scale coherent motion. Just downstream of the actuators the zero-crossing and minimum points of the correlation function occurs further out in the spanwise direction, suggesting that the most coherent motion in the flow is now further apart and weaker. As the streamwise station moves further downstream, the correlation recovers to its uncontrolled values. Thus, the reduction in turbulent fluctuations obtained using the current control scheme seems to be achieved by reducing the strength of the most coherent flow structures and to inhibit their ability to interact with each other by increasing their average spanwise separation by more than 25% (from $\approx 90l^*$ to $120l^*$).

5.5 Reynolds Number Dependence

For practical flow control purposes, the length, time and velocity scales must be comparable with the scales of the coherent structures in the flow so as to maintain controllability. These physical dimensions in these experiments were chosen for a particular flow condition and it is instructive to consider scaling arguments based on varying flow conditions. As

discussed in the introduction, there are strong indications that the coherent structures scale with the viscous scales which in turn scale with the Reynolds number. Rathnasingham and Breuer [52] suggested that the length and time scales associated with the actuator should scale with the Reynolds number based on the local momentum thickness.

The relative location of the sensors and actuators depend on the average size and separation of the coherent structures in the flow and can be estimated using the viscous scales. For example, the spanwise separation of both sensors and actuators must be small enough so that at least two devices are placed within the average distance between coherent structures (measured to be between $90l^*$ and $150l^*$). In these experiments, this separation was $40l^*$ which would be close to the maximum allowed. Since the viscous length scale falls with Reynolds number (approximately as $\theta\, Re_\theta^{-9/8}$, where θ is the momentum thickness [23]) the separation between the devices must also be reduced accordingly so as to maintain the controllability of the flow.

Similarly, the time scales associated with the sensors and actuators as well as the controller must scale with varying flow conditions. As for the length scale, the viscous time scale approximately varies as $\theta^2\, Re_\theta^{-7/4}$. In these experiments the time scales of the sensors and actuators were much higher than that associated with the large scale motion. For example, the period between bursts was measured to be approximately 5.4 ms, while the sensor and actuator time scales were less than devices). The controller was also run at a far higher rate than necessary ($\approx 30\mu$s). Thus, the time scales in the current control scheme will still be adequate for a moderate increase in Reynolds number (an increase by a factor of 3 in Reynolds number would place the time scales of the actuator at the upper limit).

5.6 Recommendations for Further Work

The research described in this thesis, on the system identification and control in the near-wall region of a turbulent boundary layer shows promise for future work using similar control architectures. In the course of the study, several observations were made, highlighting possible modifications to the current system that would have been desirable in improving its overall performance. Some of these ideas are presented below.

5.6.1 Fabrication

The fabrication of sensors and actuators for these experiments were carried out manually so that repeatability could not be guaranteed. The actuators had slightly different resonant frequencies and had moderate structural damping due to the poor manufacturing tolerances. Improvements in fabrication should focus on using fewer components in each actuator to improve rigidity and a removable design that would allow the replacement of a a single actuator within an array.

5.6.2 Filter Design

The choice of an FIR filter in these experiments was mainly based on convenience. They have constant phase and are always stable. The flexibility of IIR filters, however, may

prove to be advantageous when considering improvements in the system identification and prediction of the flow. IIR filters generally require fewer poles than FIR filters making them more attractive when considering problems with long lag times between sensors and actuators. The filter is not guaranteed to be stable, but can usually be stabilized in practice.

5.6.3 Flow Measurements

The streamwise velocity fluctuation was primarily used as a controlled parameter since it allowed for the greatest flexibility - it was mounted on a traverse; its operation was robust and convenient and it was easily replaced. The pressure measurements required embedding microphones into the flat plate at discrete points so that continuous spatial measurements were not available. The advantage of the control scheme presented here is that it can be applied in any flow regime for the control of any flow parameter, so long as it can be accurately characterized. This allows the possibility to expand the current work to attempt the control of other crucial flow quantities like wall shear stress, Reynolds stress and turbulent kinetic energy. These quantities may be similarly controlled so long as they can be measured together with the upstream detection sensors.

5.6.4 Non-Linear Control

The use of linear filters and control in this study was based on the assumption that the coherent structures were primarily governed by linear dynamics. If a linear identification scheme could be designed to describe the evolution of these flow structures, then linear control could be used to modify their characteristics.

A non-linear approach may be helpful in the identification process to further emphasize the large scale motion. For example, rather than adding the contributions from each detection sensor to predict the downstream parameter, the signals could be multiplied together, exaggerating the high energy motion. The control design discussed here is ideally suited to study the non-linear effects, in that non-linear functions of the detection signal can be chosen and implemented as independent inputs to the controller. For example, amplitude dependence may be studied by using $s_1(t)$ as well as $s_1^3(t)$ in the input to the controller.

Another aspect of the control scheme that may benefit from non-linear analysis is in the characterization of the effect of the actuator on the turbulent flow. The initial interaction of the streamwise vortices produced by the actuator with the turbulent flow is most probably non-linear.Thus a non-linear description of this interaction may lead to more accurate control.

5.6.5 Adaptation

The adaptation that was carried out in this study was limited to changing the gain and lag to minimize u_{rms} and p_{rms}. The adaptation was based on the measured value of the downstream controlled parameter.

This same measurement may be used as an error signal to implement a more robust adaptation scheme. For example, an error could be expressed in the form of the difference between the measured and desired spectra of the controlled parameter. This difference in

fed back into the controller, preferably in terms of filter coefficients and could be included into the actuator input signal to modify the appropriate frequency bands.

Bibliography

[1] S.J. Kline, W.C. Reynolds, F.A. Schraub, and P.W. Runstadler. The structure of turbulent boundary layers. *J. Fluid Mech.*, 30:741–773, 1967.

[2] R.F. Blackwelder and J.H. Haritonidis. Scaling of the bursting frequency in turbulent layers. *J. Fluid Mech.*, 132:87–103, 1983.

[3] A.V. Johansson, P.H. Alfredsson, and H. Eckelmann. *Advances in Turbulence*. Springer Verlag, 1987.

[4] P.H. Alfredsson and A.V. Johansson. On the detection of turbulence generating events. *Department of Mechanics, The Royal Institute of Technology, Sweden*, Paper 4, 1982.

[5] J. Kim. Turbulence structures associated with the bursting event. *Phys. Fluids*, 28(1):52–58, 1985.

[6] S.K. Robinson. Coherent motions in the turbulent boundary layer. *Ann. Rev. Fluid Mechanics*, 23, 1991.

[7] H.T. Kim, S.J. Kline, and W.C. Reynolds. The production of turbulence near a smooth wall in a turbulent boundary layer. *J. Fluid Mech.*, 50, 1971.

[8] R.F. Blackwelder and R.E. Kaplan. On the wall structure of the turbulent boundary layer. *J. Fluid Mech.*, 76:89–112, 1976.

[9] A.V. Johansson, P.H. Alfredsson, and J. Kim. Evolution and dynamics of shear layer structure in near-wall turbulence. *J. Fluid Mech.*, 224:579–599, 1991.

[10] M.T. Landahl. Wave breakdown and turbulence. *SIAM J. Appl. Math.*, 28:735–756, 1975.

[11] P.H. Alfredsson and A.V. Johansson. Time scales in turbulent channel flow. *Phys. Fluids*, 27:1974–1981, 1984.

[12] M.T. Landahl. On sublayer streaks. *J. Fluid Mech.*, 212:593–614, 1990.

[13] J. L. Lumley. The structure of inhomogeneous turbulent flows. In A. G. Yaglom and V. I. Tatarski, editors, *Atmostpheric Turbulence and Radio Wave Propagation*, pages 166–178. Nauka, Moscow, 1967.

[14] L. Sirovich. Turbulence and the dynamics of coherent structures. Part I: Coherent structures. *Quat. Appl. Math*, XLV(3):561–571, 1987.

[15] M. Rajaee, S.K.F. Karlsson, and L. Sirovich. Low-dimensional description of free-shear-flow coherent structures and their dynamical behaviour. *J. Fluid Mech.*, 258:1–29, 1994.

[16] N. Aubry, P. Holmes, J.L. Lumley, and E. Stone. The dynamics of coherent structures in the wall region of a turbulent boundary layer. *J. Fluid Mech.*, 192:115–173, 1988.

[17] G. Berkooz, P. Holmes, and J.L. Lumley. The proper orthorgonal decomposition in the analysis of turbulent flows. *Ann. Rev. Fluid Mech.*, 25:539–575, 1993.

[18] L.R. Keefe, P. Moin, and J. Kim. The dimension of attractors underlying periodic turbulent poiseuille flow. *J. Fluid Mech.*, 242:1–29, 1992.

[19] A.V. Johansson, J.Y. Her, and J.H. Haritonidis. On the generation of high amplitude wall pressure peaks in turbulent boundary layers and spots. *J. Fluid Mech.*, Vol. 175:119, 1987.

[20] G.K. Batchelor. *The Theory of Homogeneous Turbulence*. Cambridge University Press, Cambridge, UK, 1953.

[21] J.C.R. Hunt and J.D. Carruthers. Rapid distortion theory and the problems of turbulence. *J. Fluid Mech.*, 212:497–532, 1990.

[22] M.T. Landahl. A note on an algebraic instability of inviscid parallel shear flows. *J. Fluid Mech.*, 98:243–251, 1980.

[23] K. S. Breuer. Active control of wall pressure fluctutations in turbulent boundary layers. In *Flow Noise Modeling and Control*, volume FED 168, pages 39 – 48. ASME, 1993.

[24] K.S. Breuer, J.H. Haritonidis, and M.T. Landahl. The control of transient disturbances in a flat plate boundary layer through active wall motion. *Phys. Fluids*, 1:574–582, 1989.

[25] D.M. Nosenchuck and M.K. Lynch. Active control of low-speed streak bursting in turbulent spots. *AIAA-85-0535*, 1985.

[26] M. Gad-el Hak and Blackwelder R.F. Selective suction for controlling bursting events in a boundary layer. *AIAA Journal 27*, pages 308–314, 1989.

[27] S.A. Jacobson and W.C. Reynolds. An experimental investigation towards the active control of turbulent boundary layers. *Thermosciences Division Report No. TF-64, Department of Mechanical Engineering, Stanford University*, 1995.

[28] S.A. Jacobson and W.C. Reynolds. Active control of boundary layer wall shear stress using self-learning neural networks. *AIAA-93-3272*, 1993.

[29] S.P. Wilkinson and R. Balasubramanian. Turbulent burst control through phase-locked traveling surface depression. *AIAA-85-0536*, 1985.

[30] C.C. Chu and R.E. Falco. Vortex ring/viscous wall layer interaction model of the turbulent production process near walls. *Experiments in Fluids*, 6, 1988.

[31] H.A. Carlson and J.L. Lumley. Active control in the turbulent wall layer of a minimal flow unit. *J. Fluid Mech.*, 329:341–371, 1996.

[32] H. Choi, P. Moin, and J. Kim. Active turbulence control for drag reduction in wall-bounded flows. *Journal of Fluid Mechanics*, Vol. 262:75–110, 1994.

[33] M.J. Walsh. Viscous drag reduction in boundary layers. In D.M. Bushnell and J.N. Hefner, editors, *Progress in Astronautics and Aeronautics, Vol. 123*, 1990.

[34] C. Lee, J. Kim, D. Babcock, and R. Goodman. Application of neural networks to turbulent control for drag reduction. *Phys. Fluids*, page In press, 1997.

[35] B.D. Coller, P. Holmes, and J.L. Lumley. Control of bursting in a boundary layer model. *Appl. Mech. Rev.*, 47:S139–S143, 1994.

[36] T.R. Bewley and P. Moin. Optimal control of turbulent channel flows. *Active Control of Vibration and Noise, ASME*, 75, 1994.

[37] G.F. Franklin, J.D. Powell, and M.L. Workman. *Digital Control of Dynamic Systems, 2^{nd} Edition.* Addison-Wesley Publishing Company, Reading, Massachusetts, 1992.

[38] A.A. Townsend. *The Structure of Turbulent Shear Flow, 2nd ed.* Cambridge University Press, Cambride, UK, 1976.

[39] R.G. Brown and P.Y.C. Hwang. *Introduction to Random Signals and Applied Kalman Filtering, 2^{nd} Edition.* John Wiley & Sons, New York, New York, 1992.

[40] J.S. Meditch. *Stochastic Optimal Linear Estimation and Control.* McGraw-Hill, Inc., New York, New York, 1969.

[41] Truxal, J.G. *Automatic Feedback Control System Synthesis.* McGraw-Hill, Inc., New York, New York, 1955.

[42] R.G. Brown and J.W. Nilsson. *Introduction to Linear Systems Analysis.* John Wiley & Sons, New York, New York, 1962.

[43] W.B. Davenport Jr. and W.L. Root. *Introduction to Random Signals and Noise.* McGraw-Hill, Inc., New York, New York, 1958.

[44] G.R. Cooper and C.D. McGillem. *Probabilistic Methods of Signal and System Analysis, 2^{nd} Edition.* Holt, Reinhart & Wilson, New York, New York, 1986.

[45] J.S. Bendat and A.G. Piersol. *Random Data: Analysis and Measurement Procedures.* Wiley-Intersciences, New York, New York, 1971.

[46] T. Lorkowski, R. Rathnasingham, and K.S. Breuer. Small scale forcing in a turbulent boundary layer. *AIAA-97-1792*, 1997.

[47] M.E. Grimaldi. Roughness-induced boundary layer transition. *Masters Thesis, Department of Aeronautics and Astronautics, MIT*, 1994.

[48] V.C. Patel. Calibration of the preston tube and limitations on its use in pressure gradients. *J. Fluid Mech.*, 23:185–208, 1965.

[49] J.H. Haritonidis. The measurement of wall shear stress. In M. Gad-el Hak, editor, *Advances in Fluid Mechanics Measurements*. Springer Verlag, 1988.

[50] G. Schewe. On the structure and resolution of wall pressure fluctuations associated with turbulent boundary layer flow. *J. Fluid Mech.*, 134:311, 1983.

[51] H. Naguib, S. Gravante, and C. Wark. Extraction of turbulent wall-pressure time-series using an optimal filtering scheme. *Experiments in Fluids*, 22, 1996.

[52] R. Rathnasingham and K.S. Breuer. Coupled fluid-structural characteristics of actuators for flow control. *AIAA Journal*, 35(5), May 1997.

[53] D.J. Coe, M.G. Allen, M.A. Trautman, and A. Glezer. Micromachined jets for manipulation of macro flows. *Solid-State Sensor and Actuator Workshop*, pages 243–247, 1994.

[54] R.D. James, J.W. Jacobs, and A. Glezer. Experimental investigation of a turbulent jet produced by an oscillating surface actuator. *Proceedings of the Twelfth US National Congress of Applied Mechanics*, pages S127–S131, 1994.

[55] S.A. Jacobson and W.C. Reynolds. A piezoelectric actuator for controlling turbulent flows. *Status Report, Department of Mechanical Engineering, Stanford University*, 1993.

[56] S.A. Jacobson and W.C. Reynolds. Active control of transition and drag in boundary layers. *Bulletin of the American Physical Society*, 39(9), 1994.

[57] S.G. Saddoughi. Experimental investigations of 'on-demand' vortex generators. *Annual Research Briefs, Center for Turbulence Research*, pages 197–203, 1994.

[58] R.D. Wiltse and A. Glezer. Manipulation of free shear flows using piezo actuators. *Journal of Fluid Mechanics*, Vol. 249:261–285, 1993.

[59] H. Schlichting. *Boundary Layer Theory*. McGraw-Hill, Inc, New York, New York, 1968.

[60] R. Rathnasingham. Coupled fluid-structural characteristics of actuators for flow control. *Masters Thesis, Department of Aeronautics and Astronautics, MIT*, 1995.

[61] R.D. Blevins. *Formulas for Natural Frequency and Mode Shape*. Krieger Publishing Company, Malabar, Florida, 1984.

[62] L.P. Purtell, P.S. Klebanoff, and F.T. Buckley. Turbulent boundary layers at low reynolds numbers. *Phys. Fluids*, 24:802–811, 1981.

[63] J. Kim, P. Moin, and R. Moser. Turbulence statistics in fully developed channel flow. *J. Fluid Mech.*, 177:133–166, 1987.

[64] L.S. Gresko. Characteristics of wall pressure and near-wall velocity in a flat plate turbulent boundary layer. *FDRL Report 88-2. Department of Aeronautics and Astronautics, Massachusetts Institute of Technology*, 1988.